Master's thesis

Emil Stave
Stian Stensrud Normann

On the Ultimate Limit State Capacity of Slender Steel Beams with Unstiffened Web Openings

Master's thesis in Civil and Environmental Engineering
Supervisor: Arne Aalberg
June 2023

NTNU
Norwegian University of Science and Technology
Faculty of Engineering
Department of Structural Engineering

NTNU
Norwegian University of
Science and Technology

Emil Stave
Stian Stensrud Normann

On the Ultimate Limit State Capacity of Slender Steel Beams with Unstiffened Web Openings

Master’s thesis in Civil and Environmental Engineering
Supervisor: Arne Aalberg
June 2023

Norwegian University of Science and Technology
Faculty of Engineering
Department of Structural Engineering

NTNU
Norwegian University of
Science and Technology

Abstract

Theoretical knowledge on beams with web openings has existed for a long time. However, due to the lack of standardized design guidelines the development of an addition to Eurocode 3, EN 1993-1-13: *Beams with large web openings*, began in 2015. This extension is scheduled to be published in 2026, and this paper is based on the current draft as of September 26th, 2022.

The purpose of this paper is to build upon the previous research conducted at NTNU regarding the topic, specifically by evaluating the current design rules of EN 1993-1-13. In total, seven laboratory experiments has been conducted on beam specimens with various web openings and finite element models were developed and calibrated accordingly. These models yielded a general error of 3 % compared to the experimental results. Among the seven beam specimens, the last two were specifically tested for this project, and both beams failed due to Vierendeel bending, which is a fundamental failure mode within this study.

The numerical models were utilized to conduct a comprehensive parameter study on the topic of steel beams with web openings. A total of 128 finite element analyses were performed on various types of openings, and the maximum capacities of the models were compared to their corresponding Eurocode design calculations. The parameter study was limited to singular and unstiffened web openings, centered on the beams' neutral axis. Furthermore, the study only considered rectangular, elongated and circular opening shapes. Key parameters taken into account during the study included the moment-shear ratio, Tee outstand classification, opening size and geometry, as well as plastic/elastic design methods.

The moment-shear ratio was found to have little significance in the parameter study, likely due to geometric limitations imposed by the beam specimens. Additional formulae accounting for effects of corner radius in rectangular openings were proposed. Based on 56 analyzed rectangular openings, the formulae were considered to yield conservative design capacities. An addition to EN 1993-1-13 Clause 4.2(5) was formulated to address small openings, based on an analysis of 102 openings. Lastly, based on 44 different web openings, it was observed that the utilization of the plastic design capacity of the Tees did not result in a single overestimation of the ultimate load-carrying capacity of the beams, regardless of the current Tee class definition.

Sammendrag

Teoretisk kunnskap om bjelker med åpninger i steget har eksistert lenge. På grunn av mangelen på standardiserte retningslinjer for dimensjonering, ble det i 2015 påbegynt utvikling av et tillegg til Eurokode 3, EN 1993-1-13: *Beams with large web openings*. Dette tillegget skal etter planen publiseres i 2026, og denne oppgaven er basert på det gjeldende utkastet per 26. september 2022.

Formålet med prosjektet er å bygge videre på den tidligere forskningen som er utført ved NTNU på temaet, spesielt ved å evaluere de gjeldende beregningsreglene i EN 1993-1-13. Totalt er det utført syv laboratorieforsøk på bjelkeprøver med ulike åpninger i steget, og elementmodeller ble utviklet og kalibrert i basert på forsøkene. Disse modellene ga en generell feil på 3 % sammenlignet med resultatene fra eksperimentene. Blant de syv bjelkeprøvene ble de to siste testet spesielt for dette prosjektet, og begge bjelkene gikk til brudd på grunn av Vierendeel-bøyning, som er en grunnleggende bruddform i dette studiet.

De numeriske modellene ble brukt til å gjennomføre en omfattende parameterstudie av stålbjelker med åpninger i steget. Totalt 128 elementanalyser ble utført på ulike typer stegåpninger, og modellenes bruddlast ble sammenlignet med beregninger i henhold til Eurokoden. Parameterstudien var begrenset til enkeltstående og uavstivede åpninger, sentrert på bjelkenes nøytralakse. Videre ble kun rektangulære, med og uten avrunding, og sirkulære åpningsformer vurdert. Parameterne betraktet i studien, var moment-skjær-forhold, tverrsnittsklassifisering av T-utstikk, åpningsstørrelse og -geometri, samt plastiske/elastiske beregningsmetoder.

Moment-skjær-forholdet viste seg å ha liten betydning i parameterstudien, trolig på grunn av geometriske begrensninger i bjelkeprøvene. Formler som tar hensyn til effekten av hjørneradius i rektangulære åpninger ble foreslått. Det har blitt vist at disse formlene gir konservative kapasitetsberegninger basert på 56 analyserte, rektangulære stegåpninger. Basert på en analyse av 102 åpninger ble det utarbeidet et tillegg til EN 1993-1-13 punkt 4.2(5) for definisjon av små stegåpninger. Til slutt, basert på 44 forskjellige åpninger, ble det observert at utnyttelse av T-tverrsnittenes plastiske dimensjoneringskapasitet ikke resulterte i en eneste overestimering av bjelkenes totale bæreevne, uavhengig av gjeldende tverrsnittsklasse for T-utstikkene.

Preface

This master's thesis concludes our fifth and final year of the study program *Bygg- og miljøteknikk* at the Norwegian University of Science and Technology (NTNU) in Trondheim. The project has had a duration of 20 weeks and corresponds to 30 credits. It is a collaboration between Emil Stave and Stian Stendsrud Normann, with Arne Aalberg from the Department of Structural Engineering as our supervisor.

Throughout the project, we have gained better knowledge and familiarity with the structural Eurocode EN 1993: *Design of steel structures*, as well as the finite element program Abaqus. Additionally, insight on experiment techniques and a better understanding of the behavior and limitations associated with web openings in steel beams has been obtained.

We would like to express our gratitude to Arne, who has always been readily available for guidance and to Christian for his help with the laboratory work.

Trondheim, June 11th, 2023

Emil Stave　　　　Stian S. Normann

Emil Stave　　　　Stian Stensrud Normann

Table of Contents

Abstract i

Sammendrag ii

Preface iii

List of Symbols vi

1 Introduction 1

1.1 Background 1
1.2 Scope 1
1.3 Theory 2

2 Experiments 5

2.1 Specimen Details 5
2.2 Method 9
2.3 Geometric Imperfections 12
2.4 Test Results 13
  2.4.1 Specimen F 13
  2.4.2 Specimen G 16

3 Numerical Modeling 21

3.1 Cross Section 21
3.2 Material Data 22
3.3 Boundary Conditions and Loading 23
3.4 Analysis Methods 24
3.5 Imperfections 24
3.6 Element Assignment 25
3.7 Meshing 25

4 Precision of the Numerical Models 27

4.1 Variations in the Second Moment of Area 27
4.2 Impact of the Imperfection Amplitudes 28
4.3 Mesh Size Significance 29
4.4 Comparison of Experiments and Numerical Models 31
  4.4.1 Specimen A 32
  4.4.2 Specimen B 34
  4.4.3 Specimen C 36
  4.4.4 Specimen D 38
  4.4.5 Specimen E 40
  4.4.6 Specimen F 42
  4.4.7 Specimen G 46

4.5 Assessment of the Numerical Model Precision 49

5 Parameter Study 51

5.1 Identification of Failure Modes 51
5.2 Opening Corner Radius in Eurocode Design Capacity 55
5.3 Moment-Shear Ratio at Web Opening 55
5.4 Corner Radius of Rectangular Web Openings 58
5.5 Plastic Design Capacity of Tees in Vierendeel Bending 61
5.6 Small Web Openings 69

6 Conclusions and Suggestions 77

6.1 Conclusions 77
6.2 Suggestions for Further Study 78

Bibliography 79

Appendix 81

A Numerical Model Eigenmodes of Specimen F 81
B Numerical Model Eigenmodes of Specimen G 83
C Response Curves of Various Failure Modes - Examples 85
D Design Capacity of Specimen F According to the Eurocode 87
E Design Capacity of Specimen G According to the Eurocode 95

List of Symbols

The following symbols are used in the report. The symbols are defined according to EN 1993-1-13 Clause 3.2 *List of Symbols* [1].

χ_{wp}	Reduction factor due to web-post buckling
χ_{w}	Reduction factor due to web buckling
$\gamma_{\mathrm{M0}}, \gamma_{\mathrm{M1}}$	Partial material factors for steel
λ_1	Reference slenderness
$\overline{\lambda}$	Relative slenderness
$\overline{\lambda}_{\mathrm{w}}$	Relative slenderness of web next to opening
ε	Material parameter depending on yield strength; $\varepsilon = (235/f_{\mathrm{y}})^{0.5}$
a	Distance between vertical stiffeners along the beam
$A_{\mathrm{b,T}}$	Cross section area of bottom Tee
a_{eff}	Effective opening length. Used to calculate buckling capacity and deflections.
a_{eq}	Equivalent opening length. Used to calculate Vierendeel capacity.
a_{o}	Opening length
$A_{\mathrm{t,T}}$	Cross section area of top Tee
b	Flange width
b_{w}	Effective web thickness
$c_{\mathrm{b,T}}$	Length of bottom Tee outstand, including root radius
$c_{\mathrm{t,T}}$	Length of top Tee outstand, including root radius
c_{T}	Length of Tee outstand, including root radius
d_{T}	Depth of web outstand of Tee section. For rolled sections, the depth is measured from the root radius.
E	Modulus of elasticity
$f_{\mathrm{y,red}}$	Reduced yield strength considering interaction with large shear
f_{y}	Yield strength
h	Depth of steel section
h_{b}	Depth of bottom Tee
h_{eq}	Equivalent rectangular opening height
h_{o}	Opening height
h_{T}	Depth of Tee
h_{t}	Depth of top Tee
h_{w}	Depth of web
$I_{\mathrm{b,T}}$	Second moment of area of bottom Tee
$I_{\mathrm{t,T}}$	Second moment of area of top Tee

L	Length of beam span
$M_{\mathrm{b,T,Rd}}$	Design value of bending resistance of bottom Tee
M_{Ed}	Design value of global bending moment at center line of opening
$M_{\mathrm{el,wp,Rd}}$	Design value of elastic bending resistance of web-post
$M_{\mathrm{N,b,T,Rd}}$	Design value of reduced bending resistance of bottom Tee due to axial force
$M_{\mathrm{NV,b,T,Rd}}$	Design value of reduced bending resistance of bottom Tee due to axial force and shear
$M_{\mathrm{NV,T,Rd}}$	Design value of reduced bending resistance of Tee due to axial force and shear
$M_{\mathrm{NV,t,T,Rd}}$	Design value of reduced bending resistance of top Tee due to axial force and shear
$M_{\mathrm{o,Rd}}$	Design value of bending resistance of beam at opening
$M_{\mathrm{pl,Rd}}$	Design value of plastic bending resistance of Tee
$M_{\mathrm{T,el,Rd}}$	Design value of elastic bending resistance of Tee
$M_{\mathrm{T,pl,Rd}}$	Design value of plastic bending resistance of Tee
$M_{\mathrm{T,Rd}}$	Design value of bending resistance of compressed Tee section in the plane of the web
$M_{\mathrm{t,T,Rd}}$	Design value of bending resistance of top Tee
$M_{\mathrm{wp,Ed}}$	Design value of in-plane moment acting on the web-post
$N_{\mathrm{b,Ed}}$	Design value of axial force in bottom Tee
$N_{\mathrm{b,Rd}}$	Design value of buckling resistance of the compressed Tee for buckling in the plane of the web. Determined for a buckling length $0.5a_{\mathrm{eff}}$
$N_{\mathrm{b,T,Rd}}$	Design value of axial resistance of bottom tee
N_{Ed}	Design value of axial force
$N_{\mathrm{ep,Rd}}$	Design value of buckling resistance of the end-post
$N_{\mathrm{m,Ed}}$	Design value of the axial force acting on a Tee due to global bending at the center line of the opening
$N_{\mathrm{o,pl,Rd}}$	Design value of the plastic axial resistance of the steel section with opening
n_{o}	Number of regularly spaced openings along the beam
$N_{\mathrm{pl,Rd}}$	Design value of axial resistance
$N_{\mathrm{T,Ed}}$	Design value of axial force applied to the compressed Tee due to global bending and additional axial forces
$N_{\mathrm{t,Ed}}$	Design value of the axial force in top Tee
$N_{\mathrm{T,el,Rd}}$	Elastic compression resistance of Tee
$N_{\mathrm{T,pl,Rd}}$	Plastic compression resistance of Tee
$N_{\mathrm{t,T,Rd}}$	Design value of axial resistance of top Tee
$N_{\mathrm{w,Ed}}$	Design value of compression force in the web next to an opening
$N_{\mathrm{w,Rd}}$	Design value of buckling resistance of web next to an opening
$N_{\mathrm{wp,Ed}}$	Design value of compression force in web-post between openings
$N_{\mathrm{wp,Rd}}$	Design value of buckling resistance of web-post between openings

r	Root radius of rolled section
r_{o}	Radius of opening edge
s	Center to center spacing of adjacent openings
$s_{\mathrm{e,eff}}$	Effective width of end-post
s_{e}	Width of end-post between the connection and nearer edge of first opening
$s_{\mathrm{o,eff}}$	Effective width of the web-post for slenderness in web-post buckling
s_{o}	Edge-to-edge spacing of openings
s_{wp}	Width of the critical section of the web-post above the center line of the opening
t_{f}	Thickness of flange
$t_{\mathrm{w,b,T}}$	Web thickness of the bottom Tee
$t_{\mathrm{w,t,T}}$	Web thickness of the top Tee
t_{w}	Thickness of web
$V_{\mathrm{b,Ed}}$	Design value of the shear force in bottom Tee
$V_{\mathrm{b,Rd}}$	Design value of the shear resistance of the bottom Tee, limited by pure shear or *Vierendeel* bending
V_{Ed}	Design value of the shear force acting on the beam at the center line of opening
$V_{\mathrm{m,Ed}}$	Design value of the shear force acting on a Tee due to the global bending at the center line of the opening
$V_{\mathrm{o,pl,Rd}}$	Design value of plastic shear resistance at the opening
$V_{\mathrm{pl,b,Rd}}$	Design value of plastic shear resistance of the bottom Tee
$V_{\mathrm{pl,Rd}}$	Design value of plastic shear resistance of the solid web section
$V_{\mathrm{pl,t,Rd}}$	Design value of plastic shear resistance of the top Tee
$V_{\mathrm{t,Ed}}$	Design value of the shear force in the top Tee
$V_{\mathrm{t,Rd}}$	Design value of the shear resistance of the top Tee, limited by pure shear or *Vierendeel* bending
$V_{\mathrm{Vier,Rd}}$	Design value of shear resistance due to *Vierendeel* bending across the opening
$V_{\mathrm{w,Ed}}$	Design value of the compression force acting on the web
$V_{\mathrm{w,Rd}}$	Deisgn value of the buckling resistance of the web
$V_{\mathrm{wp,Ed}}$	Design value of horizontal shear force acting on the web-post
$V_{\mathrm{wp,Rd}}$	Design value of horizontal shear resistance of the web-post
x_{o}	Distance of center of opening from nearer support

1 Introduction

1.1 Background

Openings in the web of beam sections are commonly used for both practical and aesthetic reasons. Due to space limitations and cost savings, web openings may be necessary for routing e.g. cables, pipes and ventilation ducts through the beams in constructions. Furthermore, openings may be implemented in later stages of design, and quick design checks may be highly beneficial. However, large openings in beams may result in significantly reduced capacity at the opening. Currently, there are no finalized common design rules for beams with large web openings, but the development of an extension of the EN 1993: *Design of Steel Structures* that includes design rules for beams with large web openings is in progress. This extension, titled ”EN 1993-1-13: Rules for beams with large web openings”, is currently in a draft stage, and it applies to H- and I-profiles of uniform members symmetric about the weak axis. This thesis is based on the draft submitted for formal vote within CEN TC 250 (European Committee of Standardization, Technical Committee 250) on September 26th, 2022.

At NTNU, several previous theses have been conducted on this topic. These include four different master’s theses from the years 2019-2021:

- ”Bjelker med rektangulære åpninger i steget”, Marthinussen and Sandnes [2]
- ”Bjelker med sirkulære åpninger i steget”, Hovda and Hurum [3]
- ”Bjelker med åpninger i steget”, Bjerch and Aksnes [4]
- ”Beams with unstiffened web openings”, Grønland [5]

The reader of the thesis is expected to have knowledge on the topic of web openings, and relevant theory or information will be included when necessary, rather than in a comprehensive and independent theory section. This approach is taken because these previous theses have already extensively covered the theoretical background and content of EN 1993-1-13. However, some basis for design will be presented in Section 1.3. Additionally, Hagen [6], Lawson and Hicks [7] and Ferreira *et al.* [8] also cover relevant theory on the subject. This thesis will focus on the final beam specimens with web openings at NTNU and conclude the laboratory experiments.

1.2 Scope

The scope of this master’s thesis is to conclude the work done by students at NTNU on the topic, including performing the last tests on the laboratory’s beam specimens. This work will complement the previous research and provide a basis for a research paper to be published in *Journal of Constructional Steel Research*, drafted by Grønland [5]. A parametric study will aim to verify and/or suggest improvements for the current design rules in EN 1993-1-13. This study is limited to the criteria of EN 1993-1-13, as well as the following:

- Unstiffened web openings
- Web openings placed symmetrically about the beam’s neutral axis
- Singular openings
- No external loads applied over or close to the web openings
- Ultimate limit state (ULS) design

1.3 Theory

In this section, the rudimentary theory behind the design of steel beams with web openings will be presented. Definitions used in this section and the list of symbols are defined in EN 1993-1-13.

When web openings are present in beams, the internal forces along the beam have to be transferred through what are known as Tees, which are illustrated in Figure 1.1. The openings result in a reduction in the cross-sectional area, which introduces several additional potential failure modes. These include net section yielding due to bending moment and/or shear, failure due to Vierendeel bending, local and global buckling of the Tee in compression and web buckling next to the opening of the free edge. The net section failure modes are addressed in EN 1993-1-1 [9].

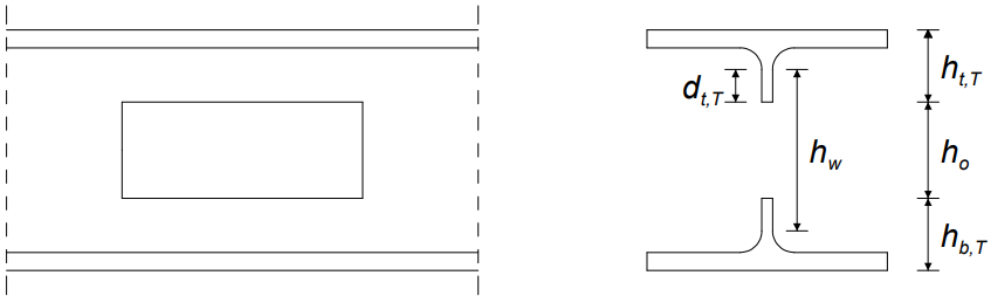

Figure 1.1: Illustration of Tees.

Plastic hinges, illustrated in Figure 1.2, occur around the web opening due to Vierendeel bending. As shown in Figure 1.3, the external shear force is transferred to the top and bottom Tees, resulting in bending of the Tees - similar to beams with fixed ends - that allow vertical translations. Furthermore, the external bending moments induce a compression force in the top Tee and a tension force in the bottom Tee, as illustrated. Due to local buckling of the Tee outstands, EN 1993-1-13 [1] imposes certain limits on the design of the Tees. These limits determine whether the Tees can be designed using plastic or elastic theory, i.e. whether the Tees are capable of developing full plasticity before local buckling occurs.

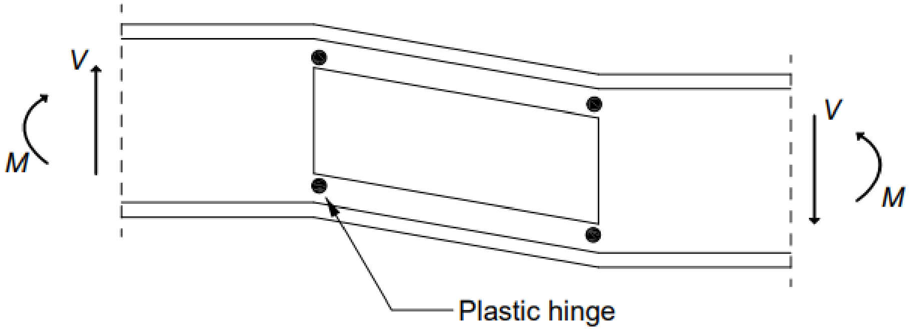

Figure 1.2: Plastic hinges in web opening region indicated by dots.

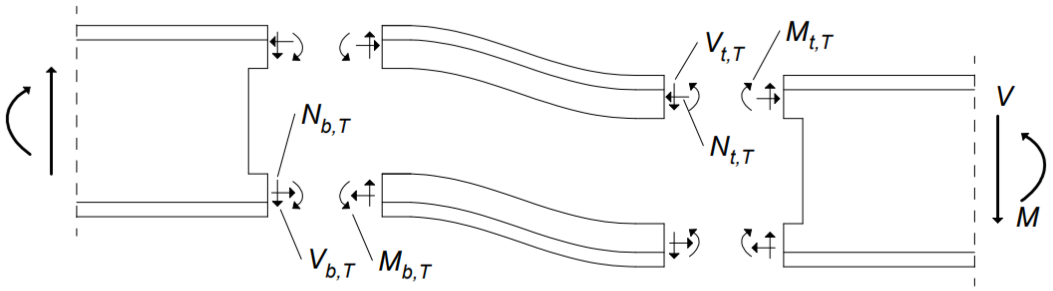

Figure 1.3: Internal forces of Vierendeel bending.

The internal stresses of the Tees corresponding to the load situation in Figure 1.3 are illustrated in Figure 1.4. $\sigma_{\mathrm{T,M}}$ denotes the normal stresses caused by the external bending moment, while $\sigma_{\mathrm{T,MV}}$ denote normal stresses resulting from the secondary bending moment induced by the external shear force. In the presented load case, the top-left corner of the opening experiences compressive stresses from both the global bending moment and the secondary bending moment. Similarly, the bottom-left corner of the opening experiences tensile stresses from both actions. On the right hand side of the opening, the normal stresses resulting from the primary and secondary moments counteract each other near the opening in both Tees due to the opposite direction of the shear force.

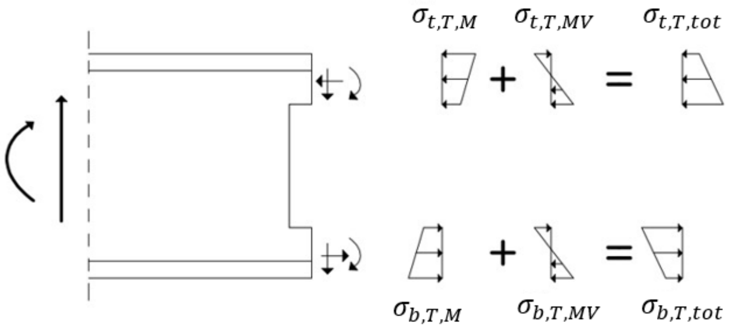

Figure 1.4: Summation of stresses due to Vierendeel bending.

For openings with rounded edges, such as circular and elongated openings, equivalent opening dimensions (shown in Figure 1.5) are utilized to simplify calculations while considering the effect of the true shape. The definition of equivalent openings are based on theoretical and empirical findings that indicate the regions where the plastic hinges develop around openings. These critical locations coincide with the corners of the equivalent rectangular opening.

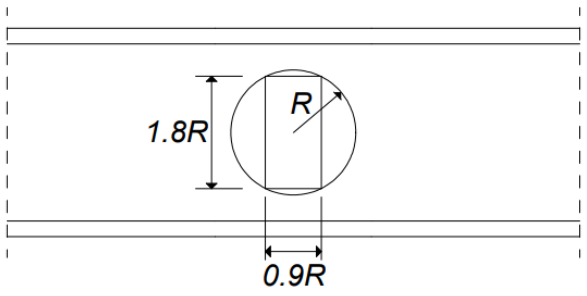

Figure 1.5: Equivalent opening for circular opening shape. Dimensions according to EN 1993-1-13 for circular openings.

Buckling of the Tees is mainly present in beams with either long web openings or large Tee outstands, d_{T}. Long openings cause long buckling lengths of the Tees, and in load scenarios dominated by the global bending moment, significant axial forces in the compressed Tee can cause buckling of the Tee. Figure 1.6 illustrates the potential buckling shapes of the Tees, according to Hagen [6, p. 59].

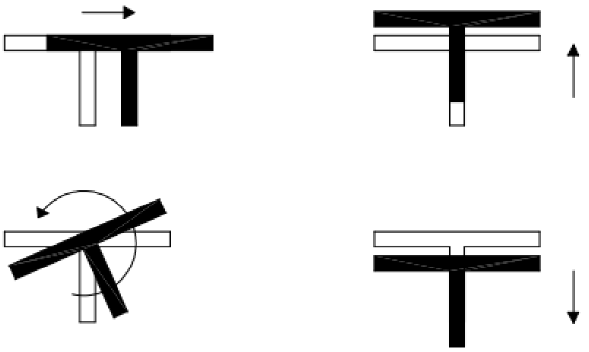

Figure 1.6: Buckling modes of the the Tees, as presented by Hagen [6, p. 59].

Buckling adjacent to the free edge of the opening can also lead to beam failure, particularly in the case of slender webs. According to EN 1993-1-13 [1], the web column affected by instability near the free edge is determined based on the effective width of the web, denoted b_w as shown in Figure 1.7. The corresponding web area is then treated as a column, which is more prone to buckling due to the presence of the adjacent web opening.

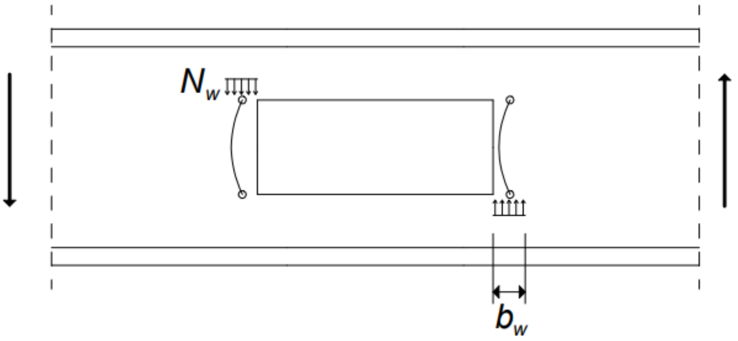

Figure 1.7: Web buckling compression force, N_w, over an effective width of the web, b_w.

2 Experiments

2.1 Specimen Details

The beams produced for the experiments were created either using two IPE 220 or two IPE 200 profiles, as shown in Figure 2.1 for the former case. On each profile, one flange is cut off and the remaining webs are welded together. It is assumed that the longitudinal weld along the neutral axis will have little to no impact on the experiments. Out of the seven experiments performed on this topic at NTNU, four beams were created with IPE 220 profiles, and three beams with IPE 200 profiles.

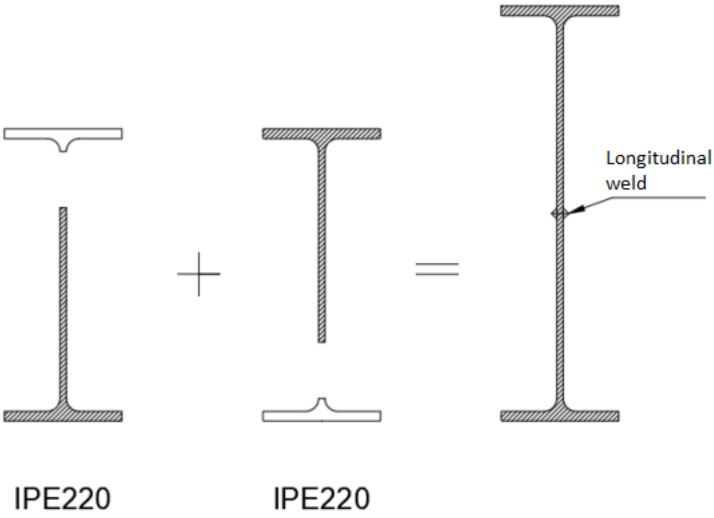

Figure 2.1: Customized cross section example for specimens using IPE 220, corresponding to specimen A, B, C and F. Figure made by Bjerch and Aksnes [4, p. 27].

A three-point bending test was performed on the four larger beams, while a four point bending test was performed on the three smaller beams. The main idea behind the different types of tests was to obtain and study different moment-shear ratios. Figure 2.2 shows the static systems for the two test configurations. The setup for specimen G effectively emulates a load case of three-point bending of a beam with shorter span.

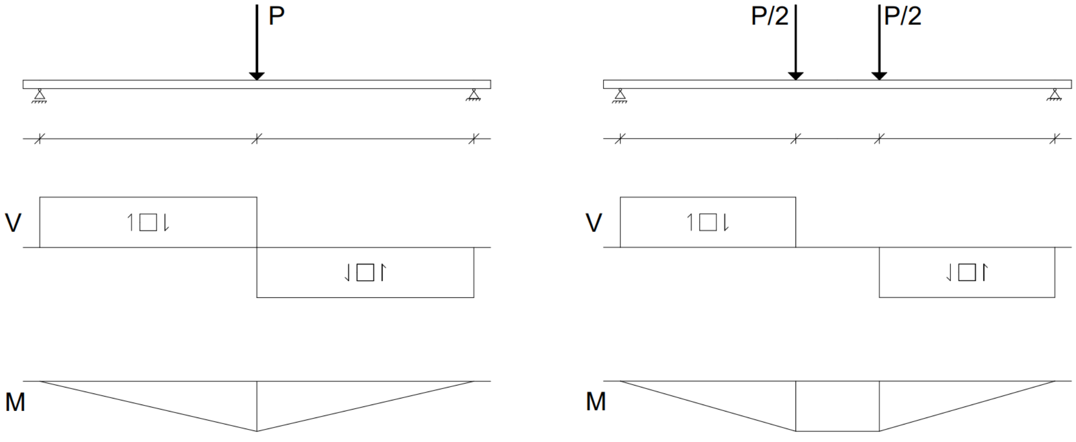

Figure 2.2: Static systems of specimens F (left) and G (right).

Table 2.1 shows the geometries of all specimens, where the external loads are applied at the midspans and transferred to web stiffeners. Specimens A to E were tested between 2019 and 2021, while specimens F and G were tested specifically for this study.

Table 2.1: The geometries of the different laboratory-tested beam specimens are shown. The web opening geometries of beams A to E are sketched by Grønland [5, p. 8].

Specimen	Web Opening Geometry [mm]	Cross Section [mm]
A	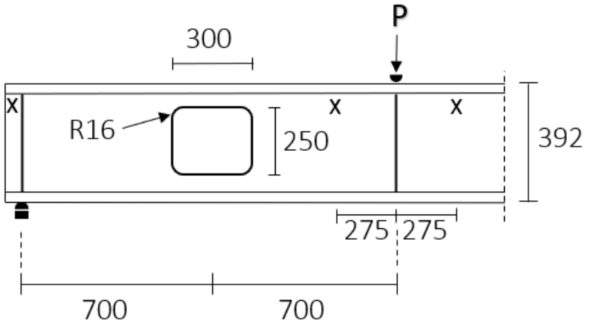 P 300 X R16 250 X X 392 275 275 700 700	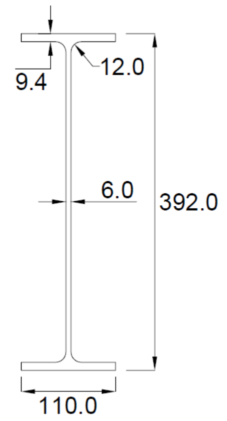 9.4 12.0 6.0 392.0 110.0
B	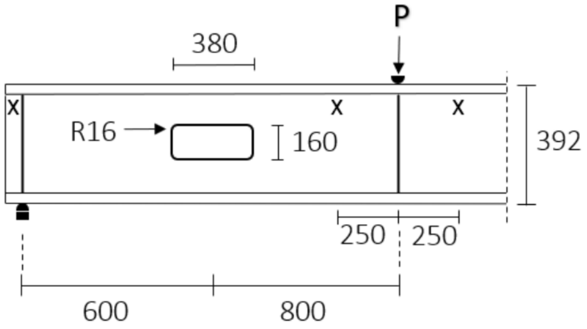 P 380 X R16 160 X X 392 250 250 600 800	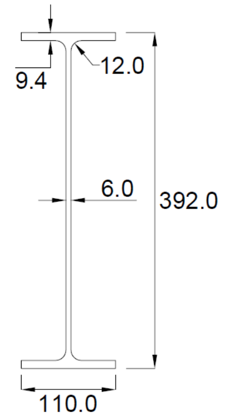 9.4 12.0 6.0 392.0 110.0
C	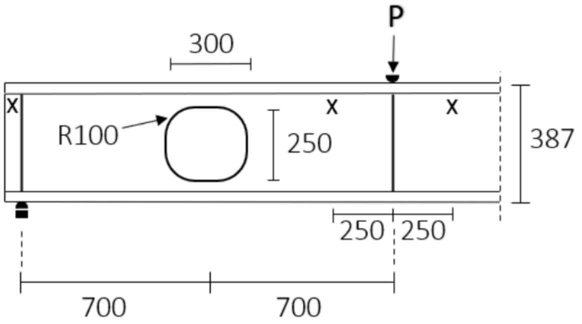 P 300 X R100 250 X X 387 250 250 700 700	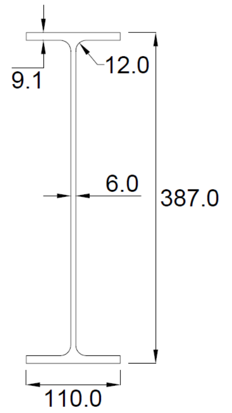 9.1 12.0 6.0 387.0 110.0

Specimen	Web Opening Geometry [mm]	Cross Section [mm]
D	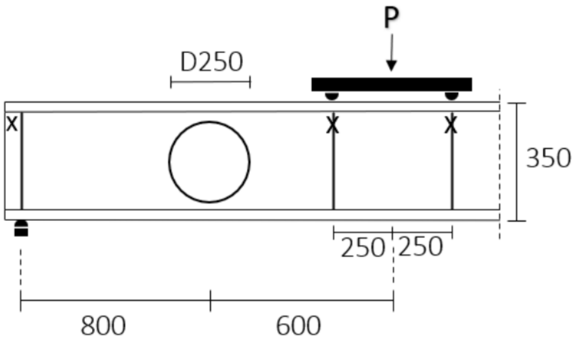 P D250 350 250 250 800 600	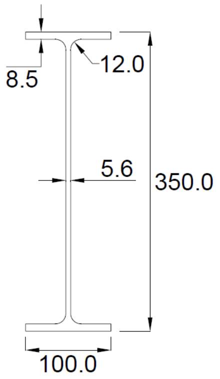 8.5 12.0 5.6 350.0 100.0
E	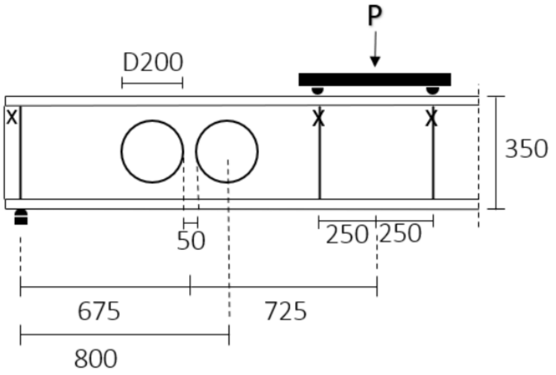 P D200 350 50 250 250 675 725 800	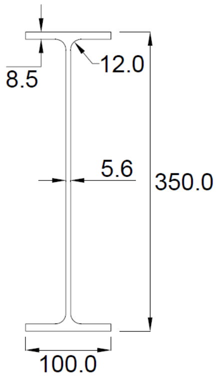 8.5 12.0 5.6 350.0 100.0
F	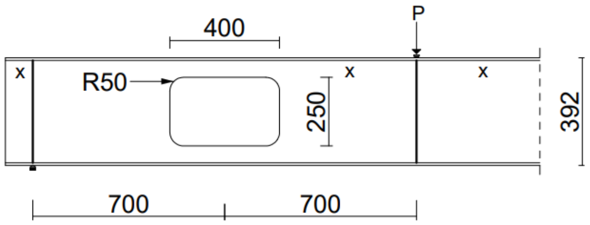 P 400 R50 250 392 700 700	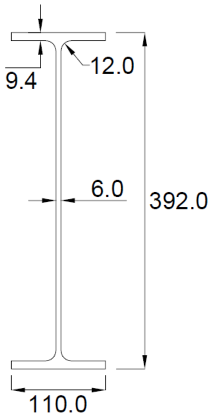 9.4 12.0 6.0 392.0 110.0
G	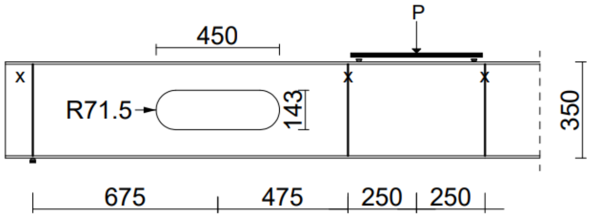 P 450 R71.5 143 350 675 475 250 250	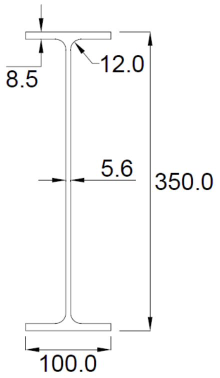 8.5 12.0 5.6 350.0 100.0

The chosen opening geometry for specimen F was primarily selected out of necessity, because the beam already had an existing opening made at this location. Consequently, the chosen opening is an elongation of the previous one, with a larger corner radius. This opening creates a situation where the effect of the corner radius, as well as Tees of section class 2, can be studied. In contrast, the opening of specimen G was made without such restrictions. Therefore, the selected opening was chosen to obtain section class 3 of the Tees in Vierendeel bending, in order to enforce elastic design rules. Moreover, the large opening length was chosen to ensure that Vierendeel bending would become the critical failure mode.

All material strengths of the specimens were determined by Masumi [10, p. 22] using coupon tensile tests, also reported by Grønland [5, p. 8]. The results are shown in Table 2.2, with corresponding sample locations shown in Figure 2.3. According to Grønland, the yield strength averages of sample locations S3 and S4 were argued to provide the most appropriate representation of the specimens due to their significant influence at the web openings.

Table 2.2: The yield strengths from tensile coupon testing reported by Grønland [5, p. 8].

Sample Location	**Beam made of two IPE 200, f$_y$ [MPa]**	**Beam made of two IPE 220, f$_y$ [MPa]**
S1	433	445
S2	443	451
S3	422	422
S4	410	426
S5	411	406
S6	390	395
S7	401	401
S8	403	405
S3 & S4 average	**417**	**424**

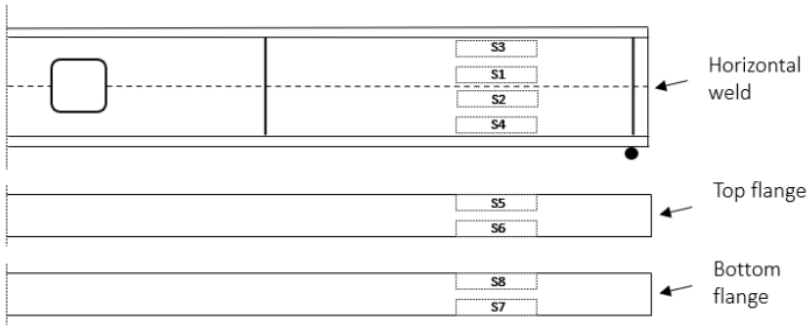

Figure 2.3: The sample locations for the tensile coupon testing. The figure was produced by Grønland [5, p. 8].

While the sample locations S3 and S4 are critical for the Tees at the openings, only the strain hardening properties of location S1 have been obtained from the previous studies. Thus, the material properties used in the parametric study in Section 5 are the data from sample location S1, in order to produce a realistic strain hardening in the numerical model. For comparison to the laboratory experiments, both the material properties from sample location S1 and the web averages for the corresponding beam height will be shown and discussed in Section 4.4.

2.2 Method

Figures 2.4 and 2.5 illustrate the two test setups. Both beams are 3.0 m long, with a 2.8 m span between the supports. The support opposite to the opening is free to roll, while the support close to the opening is restrained against all translations. The beams are loaded by a hydraulic jack capable of exerting loads up to 1000 kN. For the three-point bending test, the load is transferred through one half-cylinder at midspan, and for the four-point bending test it is transferred via an HEA 140 beam on top of two half-cylinders. Both beams are restrained against lateral torsional buckling at locations indicated by an 'x' in Figures 2.4 and 2.5, using rectangular hollow sections (RHS) with welded plates supporting each side of the beam at midspan, and clamps at the beam ends.

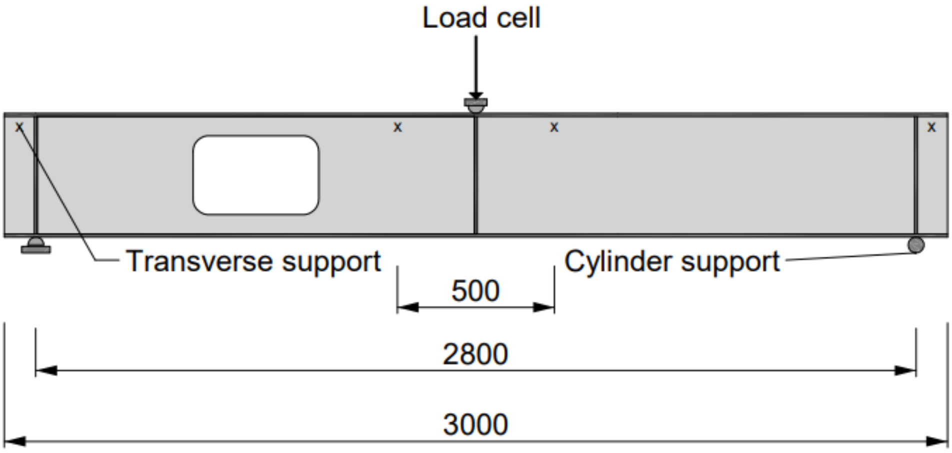
Load cell
x
x
x
x
Transverse support
Cylinder support
500
2800
3000

Figure 2.4: The experiment setup of specimen F with three-point bending. Dimensions are in mm.

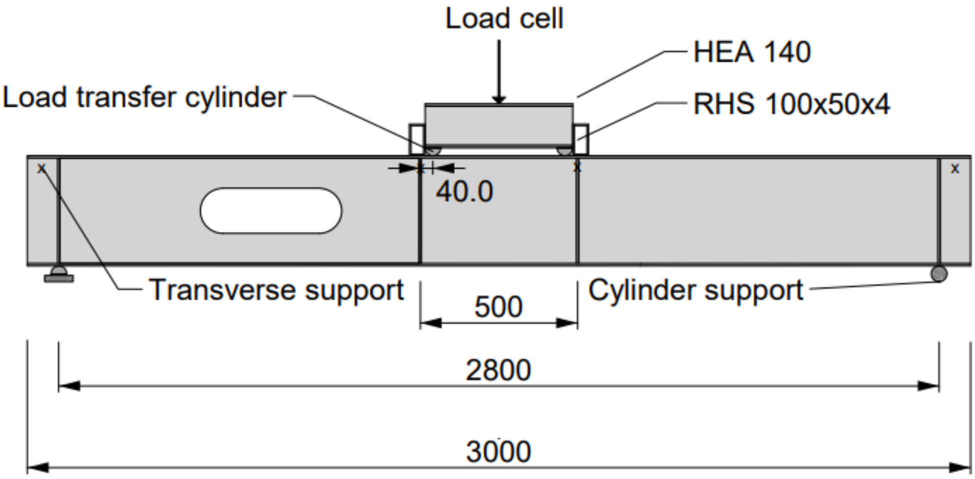
Load cell
HEA 140
Load transfer cylinder
RHS 100x50x4
40.0
x
x
x
Transverse support
Cylinder support
500
2800
3000

Figure 2.5: The experiment setup of specimen G with four-point bending. Dimensions are in mm.

The support conditions were created using one cylinder with a diameter of 50 mm which were able to roll, and one similar fixed half-cylinder. The constraints against lateral torsional buckling at the beams' ends were created by lightly fixing a small rectangular hollow section on top of the flanges above the stiffeners. Precisely allocating these clamps directly above the stiffeners was not always possible. Figure 2.6 shows an example where the clamp had to be placed beyond the support point. In this situation, the clamp will counteract the rotation occurring when the beam is bent. However, relative to the forces applied to the beam, stresses from the clamps are minuscule, and therefore considered negligible.

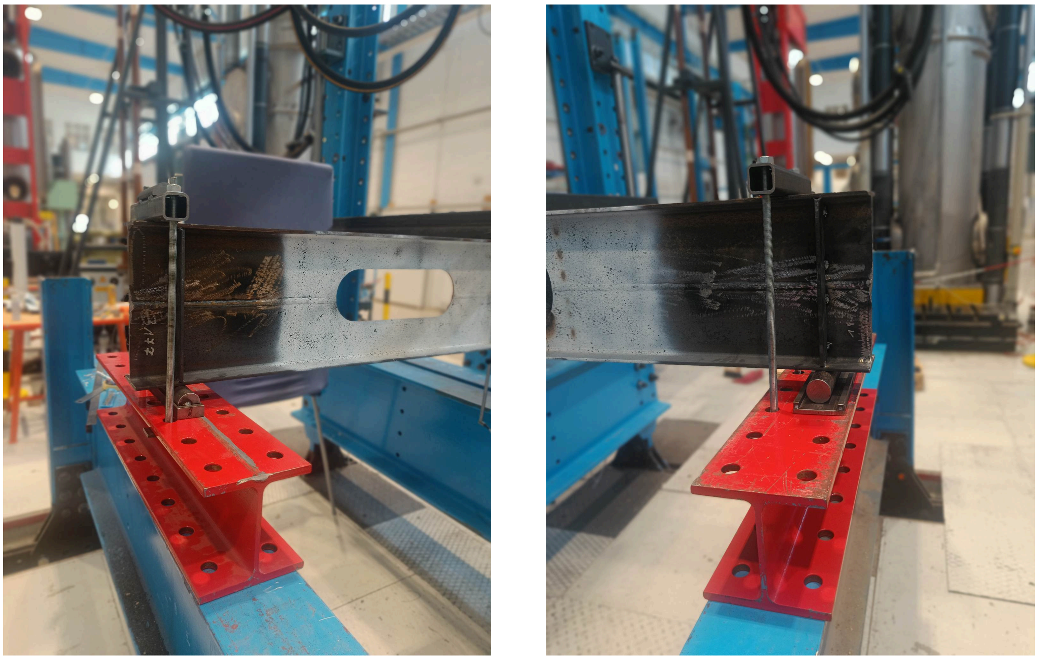

Figure 2.6: The end support conditions for specimen F. A similar configuration is also used for specimen G.

Figures 2.7a and 2.7b show how the load from the jack is transferred to the beams in the tests. In previous four-point bending tests conducted by Hovda and Hurum [3, p. 42], the load from the jack was transferred through the RHSs on either side of the midspan, with the help of a transferring beam. Consequently, they were able to direct the loads directly onto the transverse stiffeners of the beam. Here, the transferring beam, i.e. the HEA 140, was placed in between the RHSs, offsetting the pressure point of the load transfer of each half-cylinder, shown in Figure 2.7b, by 40 mm towards the center.

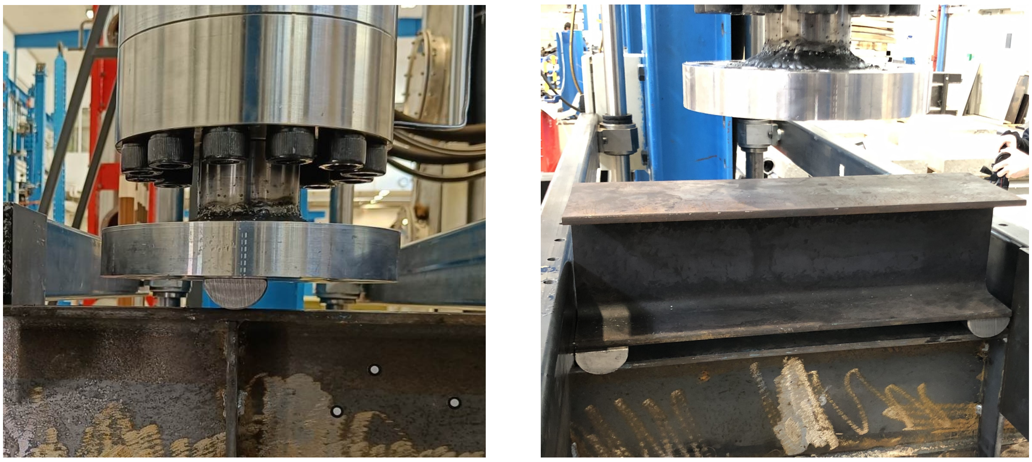

(a) One-point load transfer of the three-point bending of specimen F.

(b) Two-point load transfer of the four-point bending of specimen G.

Figure 2.7: The load transfers during the three- and four-point bending tests.

The jack was set to a displacement velocity of 2 mm/minute, resulting in test durations of 14 and 13 minutes for specimens F and G, respectively. The beams' displacements were measured at a frequency of 50 Hz using linear voltage displacement transducers (LVDTs). As shown in Figures 2.8a and 2.8b, the LVDTs were placed at the bottom flanges of the beams, below their vertical stiffeners at midspan - one for the three-point bending test, and two for the four-point bending test. Importantly, only the results from the LVDT closest to the opening of the four-point bending test will be used henceforth.

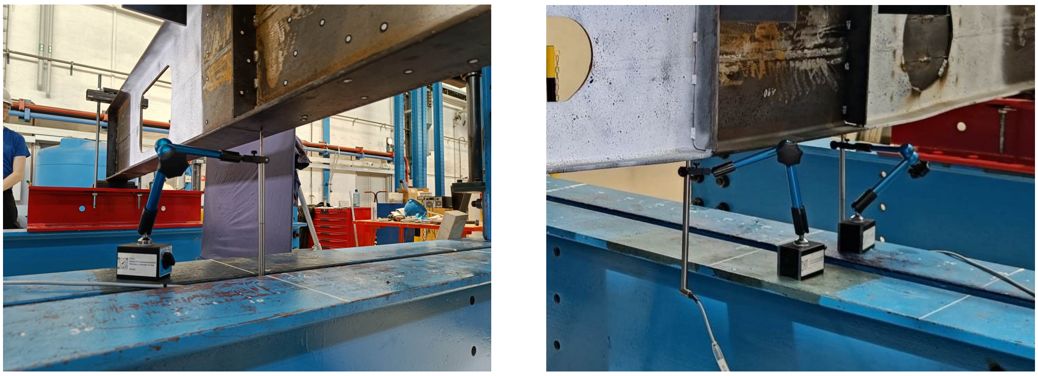

(a) The LVDT placement on specimen F. **(b)** The LVDT placement on specimen G.

Figure 2.8: LVDT placements during the three- and four-point bending tests.

Prior to testing the beams, the setup for 3D digital image correlation (DIC), shown in Figures 2.9 and 2.10, was prepared. This was done to obtain more accurate measurements of the out-of-plane deformations occurring around the web openings. By meshing grayscale images, the DIC is able to track the incremental changes in an object, thereby monitoring the strains of each steel grain in the beam. Therefore, the web surrounding the beam openings was spray-painted white, with an arbitrary pattern of black spots, creating anchor points for the mesh, as shown in Figure 2.9. Two cameras were placed to the side of the beam at distinct angles, displayed in Figure 2.10. The first camera enables a 2D DIC analysis by capturing the in-plane displacements of the web. The second camera enables the 3D DIC analysis by providing a depth of view, thus capturing the out-of-plane displacements. However, the necessary preparations for calibrating the cameras' relative positions to each other were not carried out. Consequently, only 2D DIC analyses of the web openings are presented. In order to make a rough comparison at a later stage, out-of-plane displacements were measured using 3D scans of the deformed beams after unloading, capturing only plastic deformations. The plastic deformations of the web opening corners of specimens F and G are shown in Figures 2.15 and 2.21, respectively.

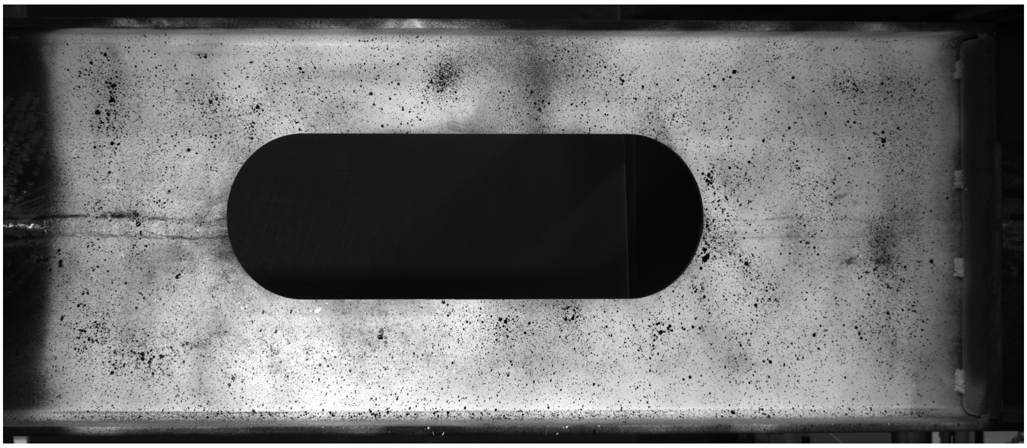

Figure 2.9: Spray-painted opening region for DIC meshing on specimen G.

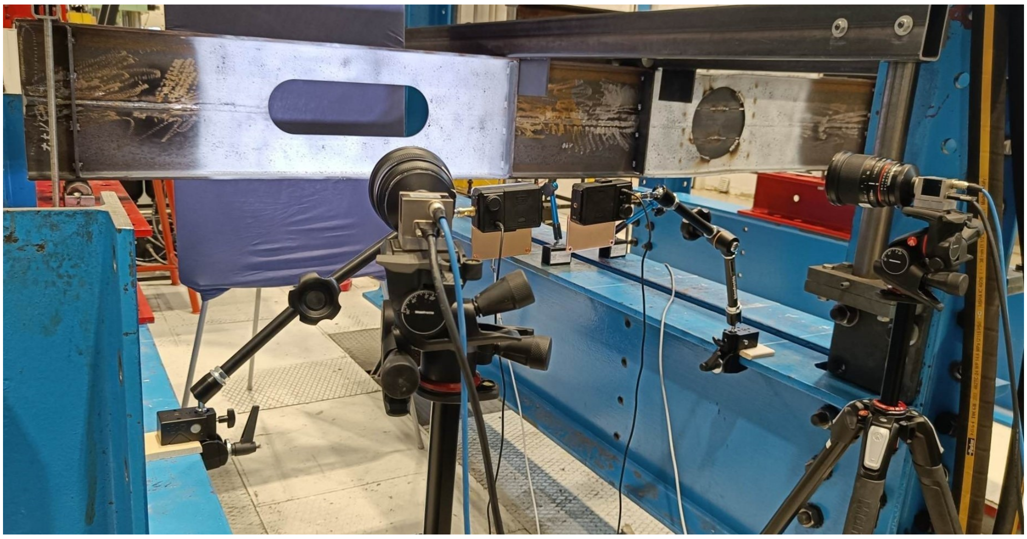

Figure 2.10: Two cameras at distinct angles for 3D DIC depth of view.

2.3 Geometric Imperfections

Table 2.3 presents manually measured imperfections at the opening side of the specimens prior to testing. Both beams had previously been used in similar bending tests. As a consequence, both specimens already had an end with extensive plastic deformations and an existing web opening welded shut. It is assumed that these deformed ends have little influence on the beam's ultimate load-carrying capacity, but they may have had a larger impact on its general stiffness. Perhaps the most critical of the imperfections was the location of the web opening of specimen G, which was intended to be centered along the neutral axis (N.A.). However, control measurements showed that the opening was shifted 10 mm closer to the compression flange, theoretically lowering its Vierendeel bending capacity. Moreover, this offset puts specimen G out of the study's scope. The consequence of specimen G's offset will be discussed in Section 4.4.7. It was not possible to reliably measure any imperfections vertically along the web of specimen F, both due to the longitudinal weld and the short Tee outstand depth.

Table 2.3: Geometric imperfections of the beam specimens prior to testing. The directions indicate orientation of a straight ruler placed along the measured part. Negative values signify amplitude towards the unpainted side.

Imperfection	**Specimen F**	**Specimen G**
Initial damages	Large deformations at other end, opening closed with welded plates	
Longitudinal weld	Increased web thickness at neutral axis, residual stresses	
Web, vertically	NA	-0.30 mm
Web, longitudinally	-0.35 mm	0.15 mm
Flange, longitudinally	0.10 mm	0.20 mm
Opening offset	-	10 mm up from N.A.

2.4 Test Results

In this section, the test results of Specimens F and G are presented. The test results of Specimens A-E from the years 2019-2021 will be introduced in Section 4.4. The main result from the experiment is the response curve, where the deformation shapes and maximum load are of key interest. In-plane strain fields will also be used for comparison to the numerical models, introduced in Section 3, although only qualitatively.

2.4.1 Specimen F

The recorded response curve from the bending test of Specimen F is shown in Figure 2.11. The observations of specimen F's behavior during bending are described below. The directions of this sections descriptions are based on the point of view shown in Figure 2.12.

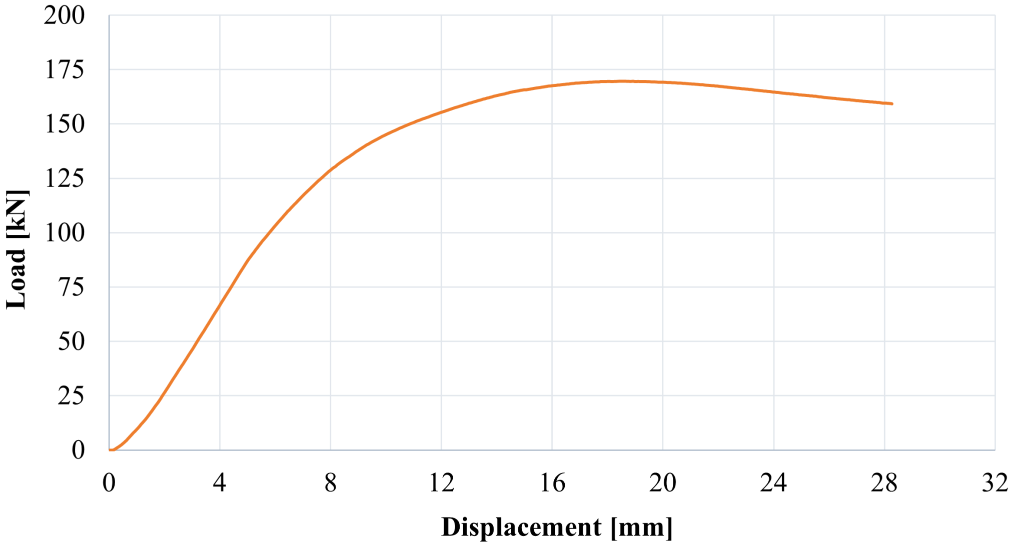

Figure 2.11: Recorded response curve from the three-point bending test of Specimen F. Displacements are measured using an LVDT below the load-point, under the stiffener at midspan.

Initially, the beam's deflections were invisible to the naked eye. When a load of 100 kN was registered, the beam's flanges started twisting slightly. Around 125 kN, the twisting ceased. However, a vertical difference between the opening's left and right side became apparent, forming a distinct linear slope over the length of the opening towards the beam's midspan. Specimen F reached its ultimate load at 169.7 kN, recorded at 18.4 mm displacement. As the load declined slowly, an indentation in the opening's bottom-right corner started growing away from the point of view. Upon reaching 22 mm of midspan displacement, an indentation in the top-left corner also began to develop. From this point on, the slope over the opening grew steeper and the indentations became more pronounced. Eventually, the corners started folding into "S-curved" shapes. The test was manually terminated at 28 mm displacement. The deformations at the end of the experiment are shown in Figure 2.13.

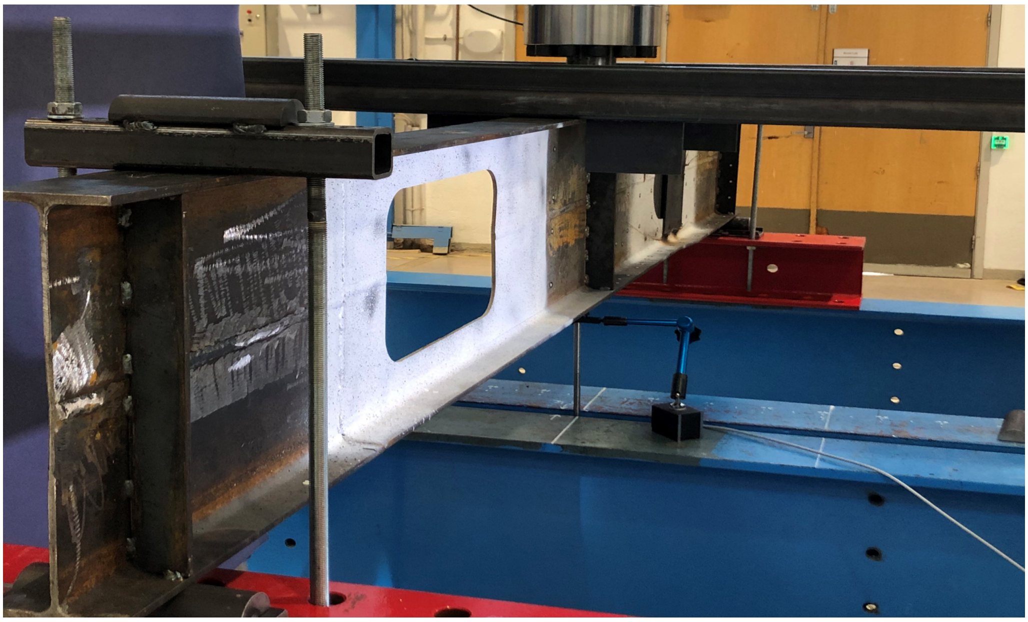

Figure 2.12: The early stages of the bending test of specimen F. No visible deformations.

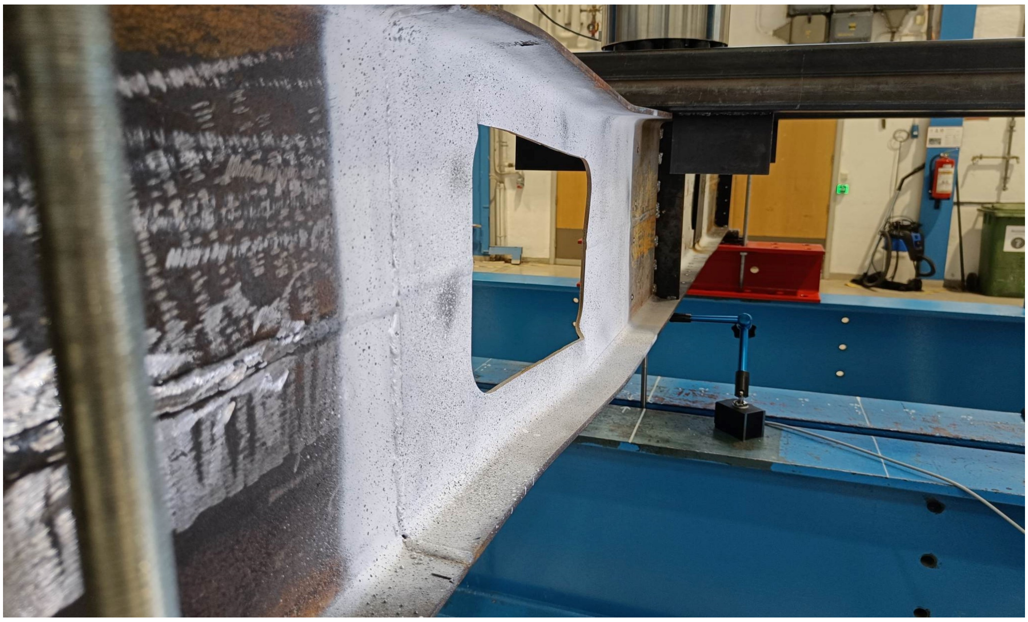

Figure 2.13: Deformation of specimen F at the end of the test, before unloading. A distinct slope over the opening's length and clear indentation of the top-left and bottom-right opening corner can be seen.

During the initial loading of the beam, the stiffness of the system increased rapidly. It was not until the recorded displacement exceeded 2 mm that the response curve eventually exhibited a linear trend. This is primarily interpreted as a consequence of the many mechanically interconnected parts in the test rig, such as support cylinders, beams and bolts, falling into place. In total, the rig was composed of 7 connected parts including the beam (but excluding bolts), between the jack and the floor. To idealize the results, the response curve is therefore shifted to the left so that its linear trend intersects with the origin of the plot (see Figure 2.14). This way, the additional displacement resulting from the initial slack in the test rig is eliminated.

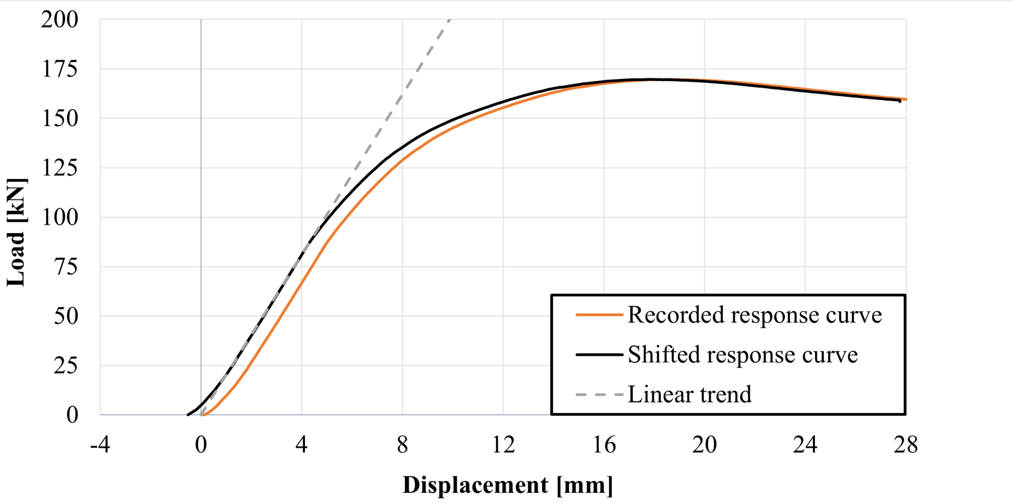

Figure 2.14: Shifting the response curve of specimen F.

As the 3D DIC was not properly calibrated, accurate out-of-plane deformations were not obtained for the specimens. However, the plastic deformation of each opening corner was measured using a 3D scan after testing and unloading the beam. The measured values are shown in Figure 2.15, where positive quantities indicate amplitudes facing the reader. The measurements are made relative to the web, and for the bottom-left corner, the two values shown in Figure 2.15b indicate deformations in both directions. The positive value refers to the corner area close to the Tee, while the negative value refers to the corner area towards the solid web.

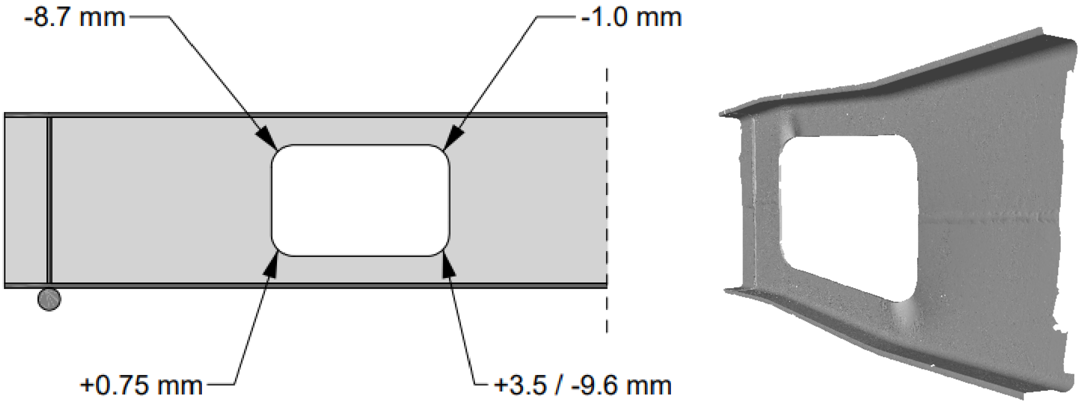

(a) CAD drawing. **(b)** 3D scan.

Figure 2.15: Measured out-of-plane displacements at the opening corners for specimen F after completed testing. Positive values indicate amplitudes facing the reader. The values were obtained from the 3D scan.

As stated in Section 2.2, the in-plane strains around the web opening were recorded with 2D DIC. The maximum and minimum principal strains recorded at the latest data frames of the tests are shown in Figure 2.16. While the specific strain values are not of particular interest, the figures clearly illustrate the locations of stress concentrations. These concentrations occur at the ends of the Tees before the corner round-offs begin, where the Tees have the smallest depth. The top-right and bottom-left corners of the opening edges are in tension, while the top-left and bottom-right corners are in compression, as indicated by the legend signs in the figures.

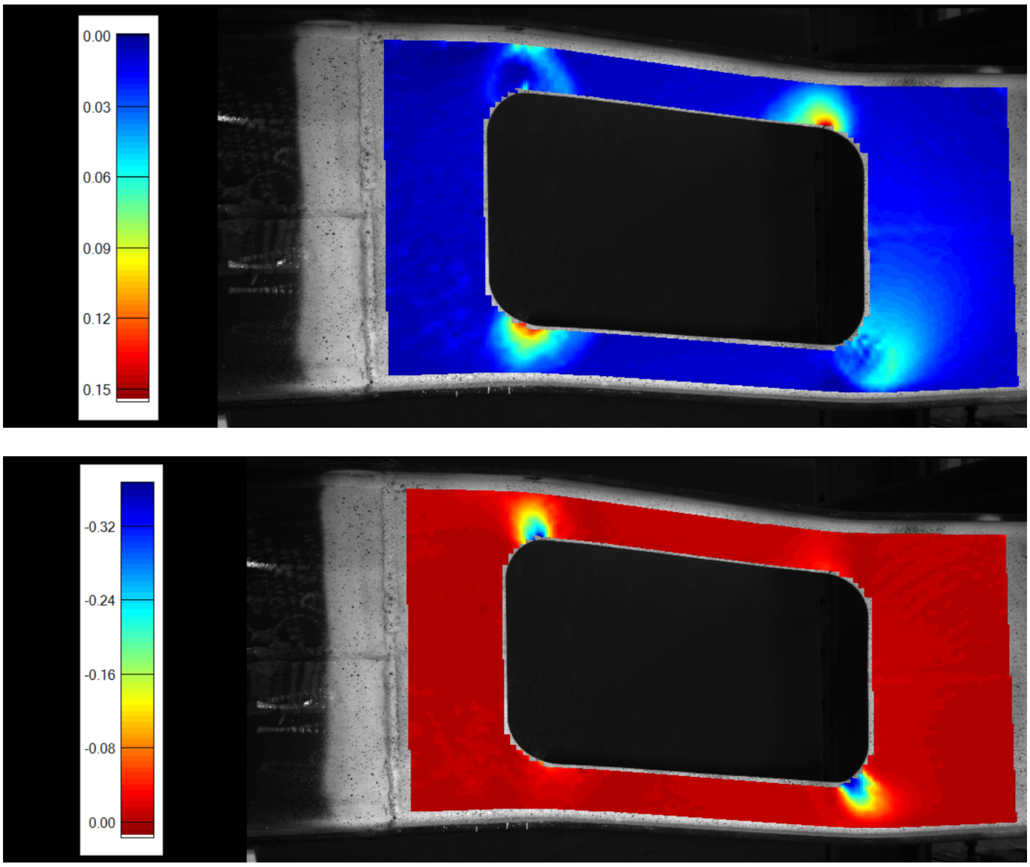

Figure 2.16: The maximum and minimum in-plane principal strains of the web opening region of specimen F, obtained from 2D DIC.

2.4.2 Specimen G

The recorded response curve from the bending test of Specimen G is shown in Figure 2.17. Observations of specimen G's behavior during bending are described below. The directions of the descriptions are based on Figure 2.18's point of view.

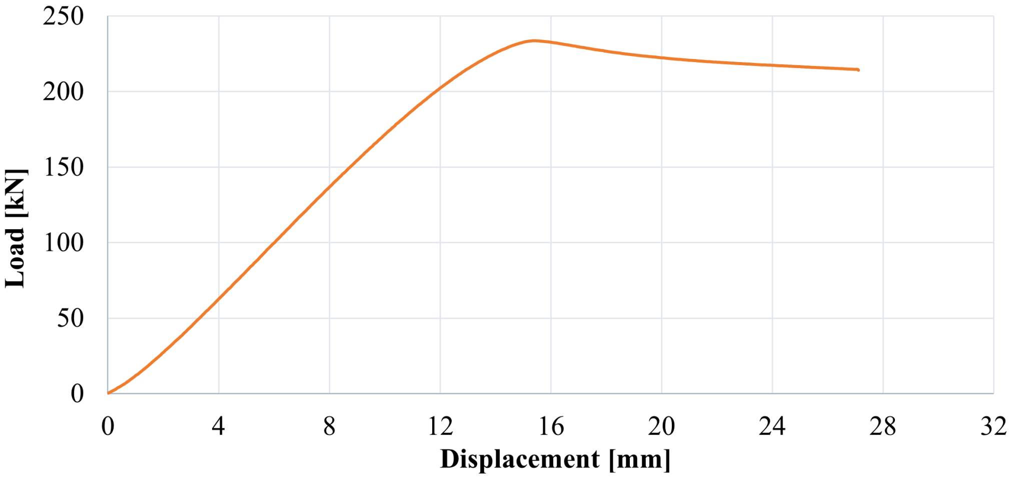

Figure 2.17: Recorded response curve from the four-point bending test of Specimen G. Displacements are measured using an LVDT under the stiffener closest to the web opening.

Deformations of the beam were not easily visible until the load reached around 200-225 kN. At that point, the largest deformations were observed at two corners of the opening, specifically at the locations where the Tee outstands became compressed due to the bending of the Tees. These corners are the top-left and bottom-right corners of the opening, and bulges started to become visible. In Figure 2.19, the bulge at the top-left corner may be the most noticeable. Unlike specimen F, these bulges were not as sharp but more rounded, covering a larger area. The maximum load was reached shortly after the appearance of these indentations and was recorded at 233.8 kN, with a corresponding displacement of 15.4 mm measured at the load load point closest to the web opening. The test was manually terminated at 27.1 mm displacement at the same location. In contrast to specimen F, the failure occurred much more abruptly, meaning that the linear deflection pattern of the response curve mostly remained until the maximum load was reached.

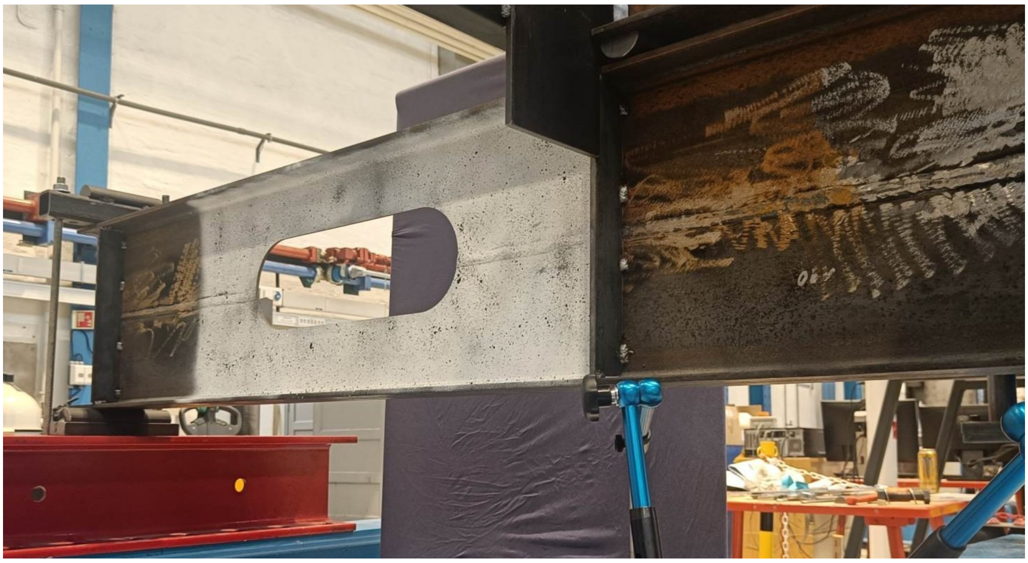

Figure 2.18: The early stages of the bending test of specimen G. No visible deformations were observed.

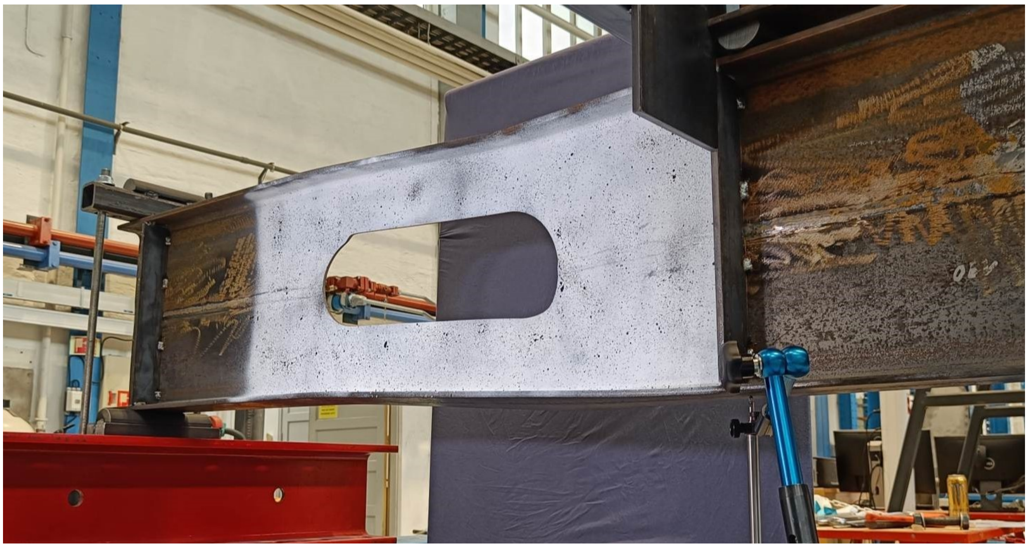

Figure 2.19: The opening deformation of specimen G at the end of the bending test, before raising the jack, reveals a distinct slope over the length of the opening and a visible indentation of the top-left opening corner.

Similarly to specimen F, the measured response in the beam only becomes linear elastic after approximately 2 mm of displacement, primarily due to the slack in the test rig. To account for this initial slack and make the curve comparable to an ideal scenario, the curve is shifted in Figure 2.20, removing 0.7 mm of the displacements. It should be noted that the stiffness of the test rig is not directly measured but influences the overall system stiffness, resulting in larger measured deformations that are not solely attributed to the beam specimen. The displacement corresponding to the maximum load for the shifted response curve is 14.7 mm.

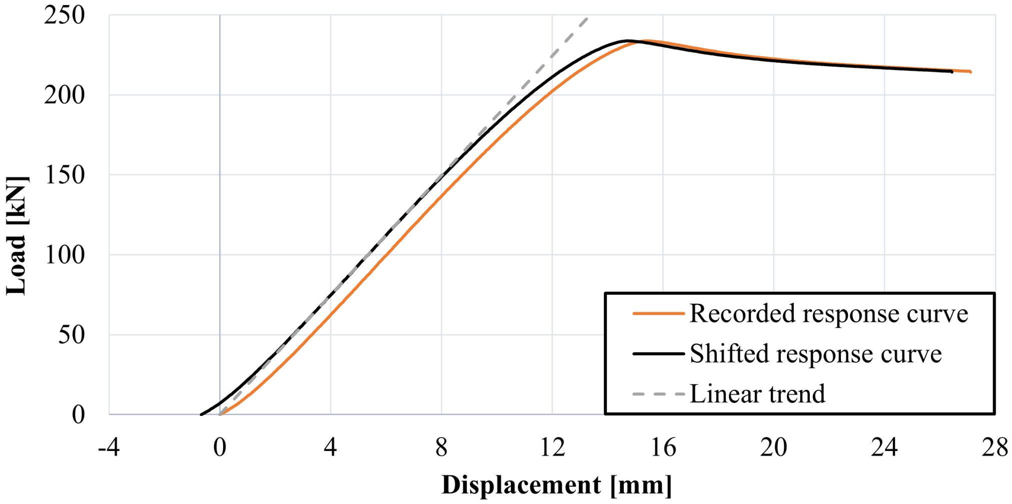

Figure 2.20: Shifting the response curve of specimen G.

Due to the lack of data on out-of-plane deformations, it is not possible to conduct a detailed and valid comparison between the opening deformations observed in the experiment and those predicted by the FE models. However, Figure 2.21 displays displacements measured using a 3D scan at the opening edges after unloading the beam. The largest measured deformation was observed at the bottom-right corner. It is worth noting that all four corners exhibited deformations in the same direction. Additionally, similar to specimen F, one of the opening corners exhibited visible deformations folded in both directions.

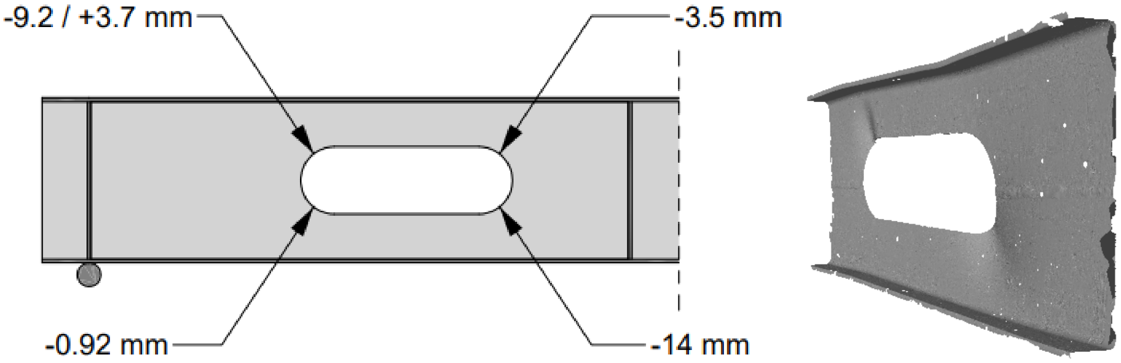

(a) CAD drawing (b) 3D scan

Figure 2.21: Measured out-of-plane displacements at the opening corners for specimen G after completed testing. Positive values indicate amplitudes facing the reader. The values were obtained from the 3D scan.

The in-plane strains around the web opening of specimen G were recorded using 2D DIC, similar to specimen F. The maximum and minimum principal strains recorded at the latest data frames of the tests are shown in Figure 2.22. While the DIC analysis of the maximum strains exhibits patterns as expected, with compression observed at the top-left and bottom-right corners, the DIC analysis of the minimum strains presents conflicting results. The analysis shows in-plane tension strains at the same locations as the in-plane compression strains, which contradicts both the observations during the experiment and the theoretical stress distribution expected from Vierendeel bending. The conflicting results could be attributed to the challenges faced by the 2D DIC in accurately analyzing the large and rounded deformation shapes of the opening corners.

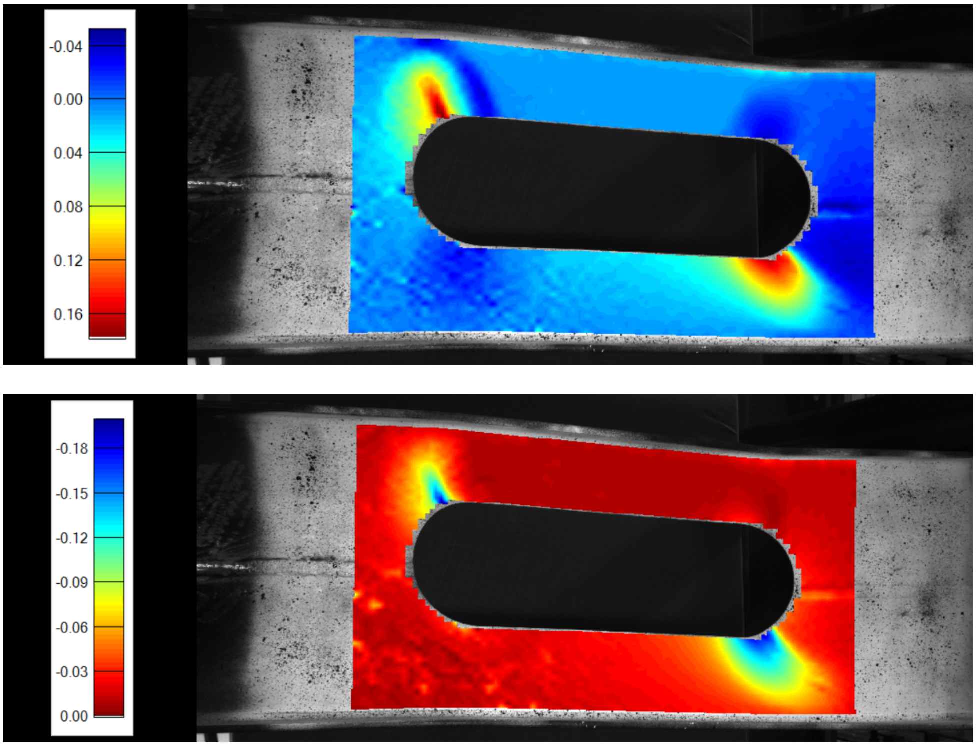

Figure 2.22: The maximum and minimum in-plane principal strains of the web opening region of specimen G, obtained from 2D DIC.

3 Numerical Modeling

For further study of beams with large web openings, numerical model replicas of all specimens tested in the laboratory were created using the finite element analysis (FEA) softwares Abaqus 2019 and Abaqus 2022. A summary of the general input in the FE models is shown in Table 3.1. Due to the controlled and idealized physical test setup, a linear analysis method was chosen for the models, significantly simplifying the modeling problem. All models were designed following the same steps, but with varying web openings, cross sections and material properties. In this section, the design choices of the numerical models are elaborated upon, and their precision is discussed in Section 4.

Table 3.1: Abaqus input details.

Meshing		
	Global	Opening region
Element type	S4R	S3
Mesh size	20mm	5mm

Analysis Type		
Time step	Linear perturbation, buckling	Static, riks
NLGEOM	NO	YES
Number of eigenvalues/ arc length (min, max)	4	1E-06, 0.02

Imperfection Amplitude	
Smallest positive eigenvalue	h/200

Material Data		
Elastic	E = 210000 GPa	$\nu = 0.3$
Plastic	True strain [-]	True stress [MPa]
	0.000	446
	0.029	459
	0.038	500
	0.077	565
	0.154	625

3.1 Cross Section

The basis for the FE models is a 3D deformable shell model with a length (called depth in Abaqus) equal to the beams' total length of 3000 mm. The sections of the models, i.e. the web, flanges and stiffeners are sketched using their center lines. Consequently, the drawn height of the cross section extrusion is one flange thickness lower than the beam's height, and the flanges and web overlap slightly. The correct cross section height is achieved when adding the thickness to the shell elements. Additionally, since the model thickness is a result of the shell element thicknesses, the root fillets of the cross sections are not modeled. The above mentioned choices are shown in Figure 3.1 and their effects are discussed in Section 4.1.

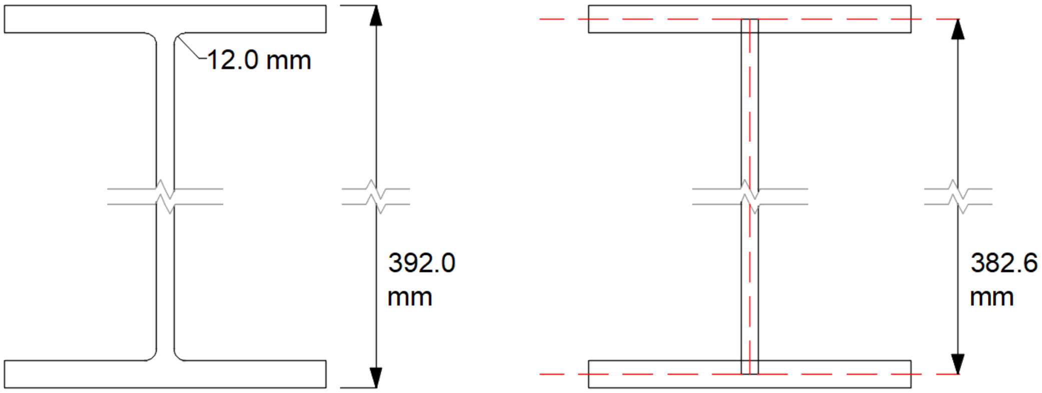

Figure 3.1: Specimen cross section (left) compared to modeled cross section (right). The shell model does not include root fillets and the web and flanges are defined at their center lines, resulting in two small overlapping rectangles where the web meets the flanges.

3.2 Material Data

The material property input for the FE models consist of both elastic and plastic components, and are presented in Table 3.2. The elastic properties, namely Young's modulus and Poisson ratio, are the same for all the numerical models. However, the plastic properties, i.e. the yield strength and plastic hardening, vary. To calibrate the numerical models to their respective specimens, the yield strength averages of sample locations S3 & S4 from Table 2.2 were selected for each corresponding specimen. Additionally, a simplified plastic strain hardening trend was applied, following the guidelines of EN 1993-1-14: *Design assisted by finite element analysis* [11]. In this case, Clause 5.3.2(1) was used, adopting a linear plastic material model with nominal plateau slope of $tan^{-1}(E/10000)$. However, for the parameter study, a non-linear hardening material model based on the values reported by Bjerch and Aksnes [4, p. 37] was utilized.

Table 3.2: Material property input of Abaqus models.

Elastic	
E = 210000 GPa	ν = 0.3

Plastic					
Specimen A, B, C & F		Specimen D, E, & G		Parameter study	
True strain [-]	True stress [MPa]	True strain [-]	True stress [MPa]	True strain [-]	True stress [MPa]
0.000	424	0.000	417	0.000	446
0.048	425	0.048	418	0.029	459
				0.038	500
				0.077	565
				0.154	625

3.3 Boundary Conditions and Loading

The boundary conditions of the models replicate the physical constraints of the lab tests. The boundary conditions and loads for models A, B, C and F are shown in Figure 3.2, and the boundary conditions and loads for models D, E and G are shown in Figure 3.3. The beams are modeled as simply supported beams, restrained from translations in all directions at one support and in two directions at the other support, while being free to move in the longitudinal direction. The distance between the two supports is 2800 mm, leaving two free ends of 100 mm on each beam end. To avoid lateral torsional buckling, the lab specimens were restrained against sideways displacement at four points on the upper part of the web along the beam span. To replicate this, the models' upper flange is restrained at the same locations along the beam: above the supports and 250 mm to each side of the midpoint.

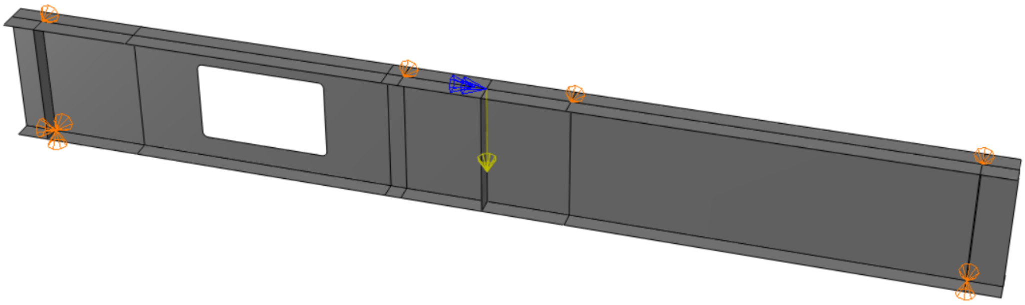

Figure 3.2: Boundary conditions and load positioning in Abaqus model of specimens A, B, C and F.

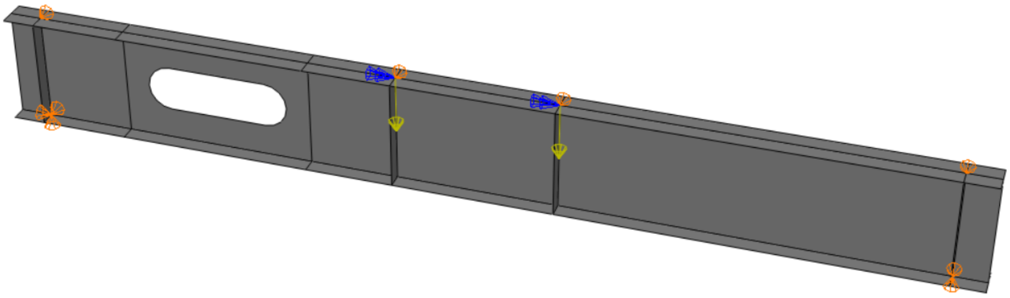

Figure 3.3: Boundary conditions and load positioning in Abaqus model of specimens D, E and G.

Additionally, the lab specimens were restrained against rotation about the longitudinal axis at the line of contact with the load transfer cylinders. To reproduce this, a *rigid body, tie constraint* was employed in the same area of the models, tying the displacement and rotations of the line together. Subsequently, the load from the load cell is modeled as a point load at the middle of the aforementioned midspan line, acting downwards in the beam's lateral direction. For beam specimens D, E and G, the load point configuration was duplicated, acting on the two restrained points on each side of the midpoint, as shown in Figure 3.3.

3.4 Analysis Methods

To account for the geometrical nonlinearities of the *Vierendeel bending* and *web buckling at the opening* failure modes, the Abaqus models were executed using the ”Static, Riks” analysis, which incorporates nonlinear geometries (NLGEOM). The Riks method is a load-deflection analysis that simultaneously solves for loads and displacements. Consequently, it employs another parameter, an ”arc-length”, to track the progress of the solution. In the load-displacement domain, the arc-length continuously measures the next step along the static equilibrium path by following a circular pattern around the current step [12]. Using a sufficiently small arc-length allows for capturing and describing abrupt changes in the equilibrium path due to buckling behavior. In most cases, a minimum arc-length of 10^{-6} proved to be adequate.

Furthermore, prior to the nonlinear analysis, a linear bifurcation analysis (LBA) in Abaqus was performed for each geometry to control the post-buckling behavior of the models. Unless the buckling behavior of a model is prescribed, the Riks method becomes discontinuous at the point of buckling. Therefore, by conducting an LBA, the eigenmodes of the beam were obtained to introduce geometric imperfection to the models, prescribing their response at bifurcation. The use of imperfections is further explained in Section 3.5. The Abaqus time step input is shown in Table 3.3, and the number of increments required generally ranged from 100 to 150 increments, depending on the beam and opening geometry.

Table 3.3: Time step details of Abaqus models.

Linear perturbation, buckling	
NLGEOM	NO
Requested eigenvalues	4

Static, Riks	
NLGEOM	YES
Arc length (min, max)	1E-06, 0.02

3.5 Imperfections

Following EN 1993-1-14 Clause 5.4.1(2)b [11], equivalent geometric imperfections were selected for the FE models to account for the possible effects of both geometrical imperfections and residual stresses. As mentioned in Section 3.4, an LBA was performed on the geometries to obtain their eigenmodes, representing their least stable configurations of buckling. For consistency, the smallest positive eigenmode for each geometry was exclusively chosen as the most critical buckling mode, in line with observations made by Hovda and Hurum [3, p. 68] and Bjerch and Aksnes [4, p. 39].

Similarly, according to EN 1993-1-14 Clause 5.4.1(3)c [11], the imperfection shape should be based on an LBA corresponding to the eigenmode associated with the expected failure mode. Concordant with beam theory, the area of failure for this eigenmode coincides with the location of the model experiencing compression stresses from both the global bending moment and local bending of the Tees (see Figure 3.4). Therefore, an imperfection was positioned at the area of failure of the eigenmode, with an amplitude of $h/200$, where h represents the beam height. This is in line with the guidelines provided in EN 1993-1-14 Table 5.6: *Equivalent geometric imperfections for cross sections of plated structures* [11]. The most common sets of specimen eigenmodes are shown in Appendix A and B for specimens F and G, respectively. Due to the difference in height between the specimens of IPE220 and IPE200, the imperfection amplitudes in Abaqus were set to 2.00 mm and 1.75 mm for the two different beam heights, respectively.

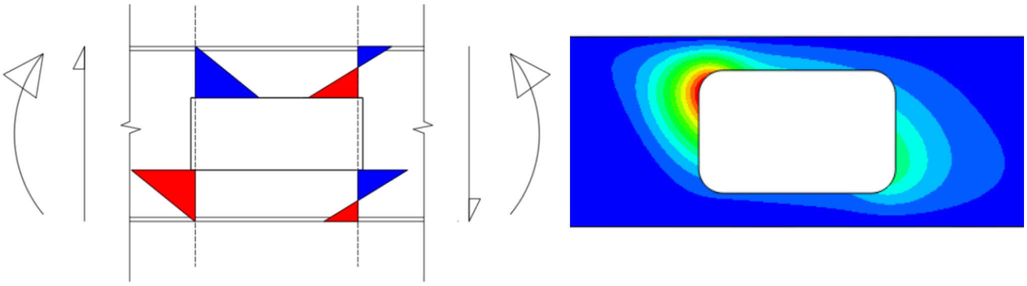

Figure 3.4: Theoretical stresses in web opening region by Grønland [5, p. 29] (left), where blue color indicates compression and red indicates tension. First positive eigenmode of Abaqus model of specimen F (right). The eigenmode coincides with largest concentration of compression stresses.

Ambiguously, according to EN 1993-1-14 Clause 5.4.2 Note 1 [11], 80 % of the geometric manufacturing tolerances can be used as the imperfection amplitudes of the cross section. However, despite the intention for the geometrical imperfection inputs to be smaller than the equivalent ones, this leads to an imperfection amplitude of 2.40 mm for all models, based on the tolerances provided in NS-EN 1090-2 [13]. The impact of this discrepancy is demonstrated in Section 4.2. Ultimately the imperfection inputs of 2.00 mm and 1.75 mm were selected.

3.6 Element Assignment

The S4R element was chosen as the foundation for the models, while the more geometrically flexible S3 element was utilized in the opening regions, as depicted in Figure 3.5. The S4R element is a 4-noded, quadrilateral, stress/displacement shell element with reduced integration, while the S3 element is a 3-noded, triangular, stress/displacement shell element. These elements demonstrate efficient performance in large-strain and buckling analyses, as they allow for arbitrary large rotations. Additionally, they employ thick shell theory, which enables a more detailed interpolation of transverse shear strains when the web and flanges of the models undergo bending and buckling. It is worth noting that while these elements account for finite membrane strains, their accuracy may be compromised in situations involving large membrane strains [12].

Because the chosen elements only consist of two nodes along their edges, they are only capable of representing linear deformations in the models. Consequently, these elements are unable to accurately capture bending behavior on their own and exhibit an overly stiff response. Nevertheless, by employing a sufficiently refined mesh with an adequate number of elements along the models' edges, a linear interpolation of the recorded displacements can yield accurate results.

3.7 Meshing

To mitigate the stiff behavior of the linear elements of the model, a "mesh refinement test" was conducted, aiming to assess the convergence of the results relative to the analysis run-time, similar to the approach employed by Bjerch and Aksnes [4, p. 40]. The test was performed on models of specimens B and F, as these exhibited significant mesh distortions in the opening regions. The results of the mesh refinement test are presented and discussed in Section 4.3.

Ultimately, a global element size of 20 mm with an element size of 5 mm at the opening edges, referred to as ”20:5” hereafter, was chosen. This mesh configuration is depicted in Figure 3.5. The 20:5 mesh demonstrated relatively stable response accuracy while maintaining an acceptable analysis run-time. However, it is important to note that the 20:5 mesh exhibited signs of stiff behavior in the more severe cases of distortion. In comparison to the 5:5 mesh used for specimen F, the 20:5 mesh demonstrated a 6% higher maximum load and up to 10% stiffer behavior after yield.

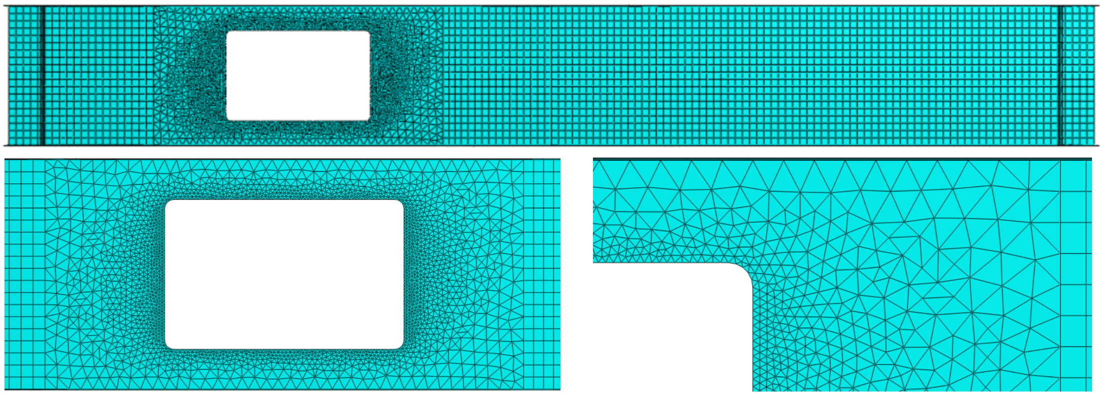

Figure 3.5: The chosen element and mesh combination for the Abaqus models consists of S4R elements as a basis, complemented by S3 elements in the opening region. The global element size is set to 20 mm, with a specific element size of 5 mm at the opening edge.

4 Precision of the Numerical Models

In order to conduct a comprehensive parametric study on beams with large web openings, a reusable numerical model was developed to ensure efficiency and reliability. Considering the need for more than 100 analyses, the models were designed to minimize run-time while maintaining a satisfactory level of accuracy. In this section, the accuracy of the design choices outlined in Section 3 is examined.

The precision of the general numerical model is evaluated by comparing its response curve to the response curves obtained from the laboratory tests. In the most extreme cases, the numerical model overestimates the ultimate load-carrying capacity by 9 %, while there is a general uncertainty of ± 3 %. These errors can be attributed, in part, to the coarse meshing employed near distortions.

4.1 Variations in the Second Moment of Area

When modeling beam sections in Abaqus, shell parts will overlap at intersections by default, as previously shown in Figure 3.1. Theoretically, this overlapping of areas leads to an increase in beam stiffness by affecting the second moment of area of the cross section. Table 4.1 demonstrates the disparity between the theoretical stiffness and the linear gradient of the Abaqus response curve of a modeled section, with and without overlapping. Additionally, the difference in maximum load of the two different modeled sections is presented.

Table 4.1: Comparison of strong axis moment of area, I_y, linear gradient and maximum load, of an IPE220 Abaqus model with and without overlapping sections.

	Modeled section with overlap	Modeled section without overlap	**Ratio**
I_y [$\times 10^6$ mm^4]	105.7	101.7	**1.039**
Linear gradient [kN/mm]	38.93	38.69	**1.006**
Max. load [kN]	408.9	404.3	**1.011**

Evidently, modeling without the default overlapping in Abaqus yields dissimilar results. Theory suggests a 3.9 % larger second moment of area when including an overlap. However, Abaqus results of the 3-point bending test only reports a 0.6 % increase in linear gradient and a 1.1 % increase in maximum load. Although ratios do not strictly correlate, an increase in stiffness from additional modeled area is indisputable.

Moreover, root fillets of the true section geometry are not included in the model, as described in Section 3.1. This too changes the theoretical stiffness of the beam, as modeling a section without root fillets reduces its second moment of area. Coincidentally, the default overlapping of Abaqus section modeling compensates for some of the loss in stiffness. To quantify, a comparison of theoretical second moment of area of the true and the modeled section geometry - with and without overlapping - is displayed in Table 4.2.

Table 4.2: Comparison of strong axis moment of area, I_y, of true beam geometry and Abaqus model with and without overlapping sections.

	Modeled section with overlap	True section geometry	**Ratio**
I_y [$\times 10^6$ mm^4]	105.7	105.8	**0.9991**

	Modeled section without overlap	True section geometry	**Ratio**
I_y [$\times 10^6$ mm^4]	101.7	105.8	**0.9612**

Seeing as the modeled section with overlap deviate from the true section's moment of area by less than 0.1 %, it was decided to model with the default overlapping of Abaqus. Furthermore, since the two modeled sections yielded at most a 1.1 % difference in both linear gradient and maximum load, a minor dissimilarity in second moment of area is considered inconsequential for further results.

4.2 Impact of the Imperfection Amplitudes

Figure 4.1 shows the response curves for specimen F and G with different imperfection amplitudes, depending on the use of EN 1993-1-14 Table 5.6 or Clause 5.4.2, as previously presented in Section 3.5. It is observed that for both specimens, the difference in amplitudes has little to no effect on the response curves. This suggests that the main influence of the imperfection is the activation of buckling modes, while minor differences in imperfection amplitude have little impact on the ultimate strength of the model, in line with observations made by Hovda and Hurum [3, p. 68] and Bjerch and Aksnes [4, p. 56].

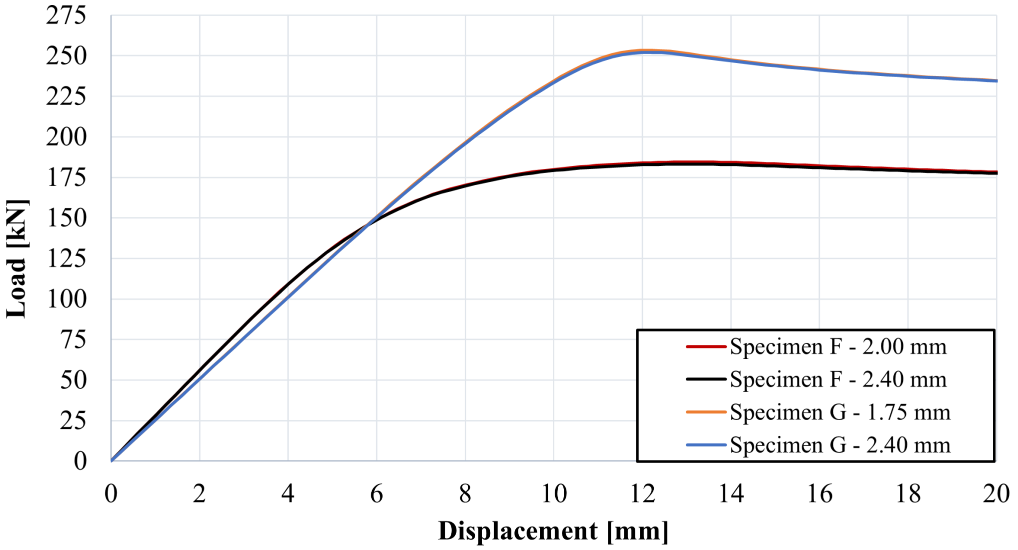

Figure 4.1: The response curves of specimen F and G modeled with different imperfection amplitudes of the first positive eigenmode, depending on applied design rule.

4.3 Mesh Size Significance

To obtain a mesh that achieves a low run-time while ensuring stable and accurate solutions, a mesh refinement test was conducted. The stability of a solution is particularly corrupted by element distortion. Therefore, models of specimens B and F were evaluated since they exhibit significant out-of-plane deformations in Vierendeel bending in the opening region.

In Tables 4.3 and 4.4, the maximum load and run time of the models with different meshes are presented. The ”relative accuracy” column compares the maximum load of all meshes to the 5:5 mesh, which is the closest to converging on the true solution. The ”relative run-time” column compares the run-time of all meshes to the chosen 20:5 mesh. Additionally, Figures 4.2 and 4.3 display the response curves of the examined meshes, providing insight on their behavior. It should be noted that Figures 4.2 and 4.3 are highlighting the relevant areas of the response curves (loads from 260-360 kN and 120-220 kN, respectively), where the deviations between the meshes may appear exaggerated.

Table 4.3: Results of the mesh refinement test on specimen B.

Mesh size [mm] (global:local)	**Max. load [kN]**	**Run-time [s]**	**Relative accuracy**	**Relative run-time**
20:20	339.1	124	1.04	0.71
20:10	345.9	148	1.06	0.85
20:5	332.3	174	1.02	1
10:10	329.5	557	1.01	3.20
10:5	326.0	640	1.00	3.68
5:5	324.9	3082	1	17.7

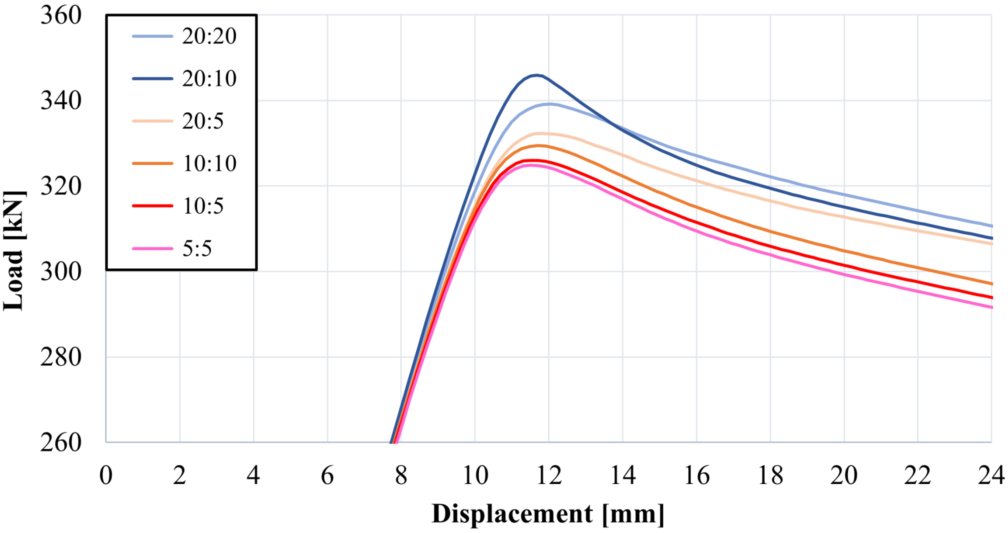

Figure 4.2: The response curves of the meshes included in the mesh refinement study of specimen B. Ultimate load area is zoomed in on, to present mesh instabilities.

In both models, the more refined meshes (10:10 and finer) steadily converged on the solution, with maximum loads deviating by up to 2 %. However, these meshes resulted in run-times exceeding 10 minutes in multiple cases. On the other hand, the coarser meshes (20:5 and coarser) stayed below 3 minutes of run-time but did show some unhealthy signs, such as sudden deviations from the equilibrium path and an overall stiff behavior. Most notably, the 20:20 mesh of specimen F, shown in Figure 4.3, illustrates the effect of shear locking as a result of the mesh being too coarse when using constant strain elements.

Table 4.4: Results of the mesh refinement test on FE model of specimen F.

Mesh size [mm] (global:local)	Max. load [kN]	Run-time [s]	Relative accuracy	Relative run-time
20:20	217.5	73	1.24	0.72
20:10	184.9	82	1.05	0.81
20:5	185.3	101	1.06	1
10:10	178.9	292	1.02	2.89
10:5	176.8	369	1.01	3.65
5:5	175.4	1816	1	18.0

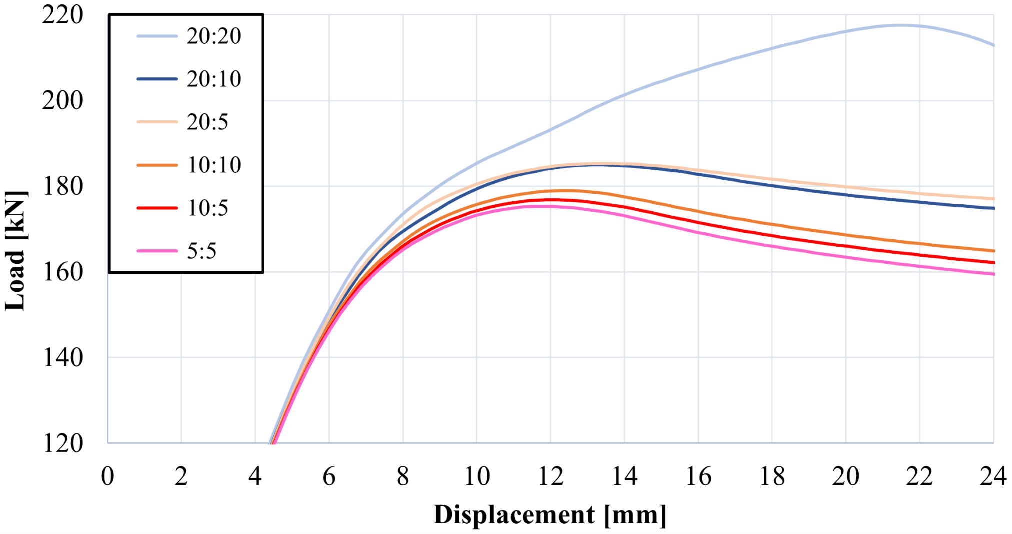

Figure 4.3: The response curves of the meshes included in the mesh refinement study of specimen F. Ultimate load area is zoomed in on, to present mesh instabilities.

In the middle of this performance spectrum is the 20:5 mesh, which provided a relatively stable solution and low run-time. However, it also showed signs of stiff behavior, particularly in the model of specimen F, with a 6 % exaggeration of the maximum load. Accordingly, to account for the uncertainty of the 20:5 mesh, a possible 6 % exaggeration of any model's stiffness in failure modes with significant distortions, e.g. Vierendeel bending and web buckling, is factored in when comparing models with specimens and Eurocode calculations.

4.4 Comparison of Experiments and Numerical Models

Table 4.5 provides a summary and comparison of maximum loads of all tests performed on specimens A-G and their respective numerical models. Due to the continuous variations in material input in studies from previous years, two extremes were chosen for the model-to-specimen comparison: the linear and nonlinear strain hardening material input models presented previously in Section 3.2, referred to as ”the weaker” and ”the stronger” material input model, respectively. Accordingly, in this section, the accuracy of both material input models are evaluated against the test results of each specimen. Additionally, 3D scanned and numerical model displacements of the specimens' web opening regions are compared.

Table 4.5: Comparison of the maximum load of the test results and numerical models.

Specimen	**Max Load Abaqus[1] [kN]**	**Max Load Abaqus[2] [kN]**	**Max Load Test Results [kN]**	**Ratio Abaqus[1]/ Test Results**	**Ratio Abaqus[2]/ Test Results**
A	216	195	228	0.947	0.855
B	330	313	321	1.03	0.975
C	293	278	300	0.977	0.927
D	259	242	255*	0.970	0.906
E	272	254	265	1.03	0.958
F	186	171	170	1.09	1.01
G	256	242	234	1.09	1.03

[1] Nonlinear strain hardening ($f_y = 446$ MPa),
[2] Linear strain hardening,
*Highest recorded value from failed test. 267 kN max. load estimated by Hovda and Hurum [3, p. 59].

For specimens A-E, the maximum load of the stronger material input model alternates within ± 3 % of the test results, with three models below and two models above their respective specimen's capacity. The weaker material input model's results are consistently conservative, but underestimate test results by up to 14 %. A similar pattern is observed for specimens F and G, although both FE models consistently report capacities larger than the experiment maximum loads. The stronger material input model overestimates both specimens' maximum load by 9 %, indicating that specimen material properties may vary significantly. However, as both specimens have been deformed in tests previously, the material input is arguably not the only factor influencing on the specimens' strength.

4.4.1 Specimen A

Figure 4.4 illustrates the recorded response curve obtained from testing by Marthinussen and Sandnes [2, p. 40] - shifted and corrected for stiffness - along with the response curves generated by the numerical model of specimen A, using the two different yield strengths. The model underestimates the test results for both material inputs. With the stronger material input, the model produces a maximum load of 216 kN, which is 5.3 % lower than the test result. This aligns closely with the reported maximum load from the model of Marthinussen and Sandnes [2, p. 55], which is 214 kN, 6.1 % lower than the test results. Meanwhile, the weaker material model underestimates the laboratory results by 14 %.

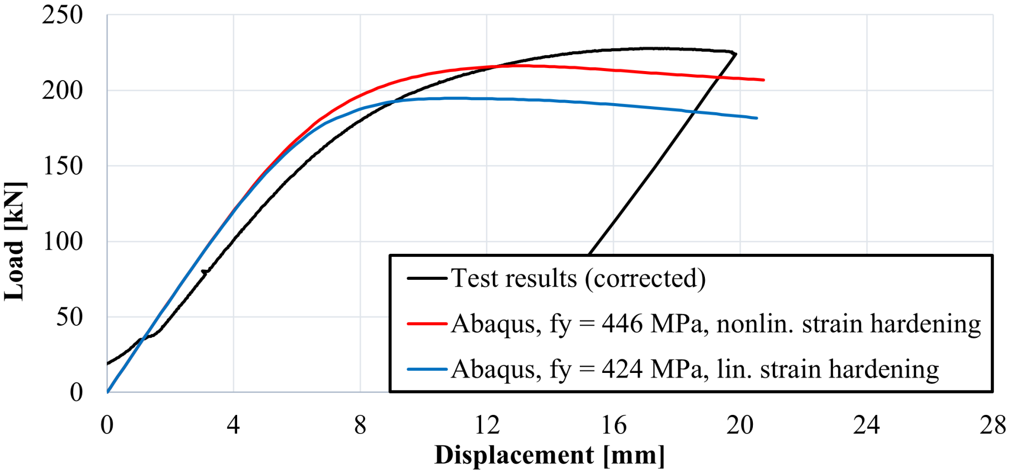

Figure 4.4: Response curves from the laboratory test and FE model of specimen A. The black curve represents the test results obtained by Marthinussen and Sandnes [2, p. 55].

The final numerical model of Marthinussen and Sandnes used a yield strength of 455 MPa, based on their own tensile coupon tests [2, p. 54], which is larger than any of the coupon tests reported by Grønland [5, p. 8]. Logically, this would result in a slightly higher capacity than for the model with a yield strength of 446 MPa. However, this is not the case, possibly as a result of a more refined element mesh, and/or an oversight in the model assembly illustrated by the buckling modes of their model [2, p. 54].

Seemingly, the test was terminated shortly after specimen A reached its maximum load, which makes it more challenging to compare the failure behavior of the model and the test. However, similar to the test, the numerical models exhibit a gradual and smooth transition between linear elastic behavior and the ultimate limit state. After reaching their maximum load, their strength slowly decline. Although probable, it is not possible to conclusively determine if the test would have exhibited the same behavior.

Upon inspecting the opening corner deformations in Figure 4.5, some minor differences can be observed. While the top-left opening corner seemingly exhibit similar deformation patterns, the bottom-right corner deflects in the opposite direction between the scan and FE model. In the FE model, this direction is primarily based on the orientation of the coordinate system, making it somewhat arbitrary. However, the main difference lies in the location of the initial bulge, which appears to be closer to the corner in the FE model than in the scan. This could imply that the buckling modes being a bit inaccurate, but mostly correct.

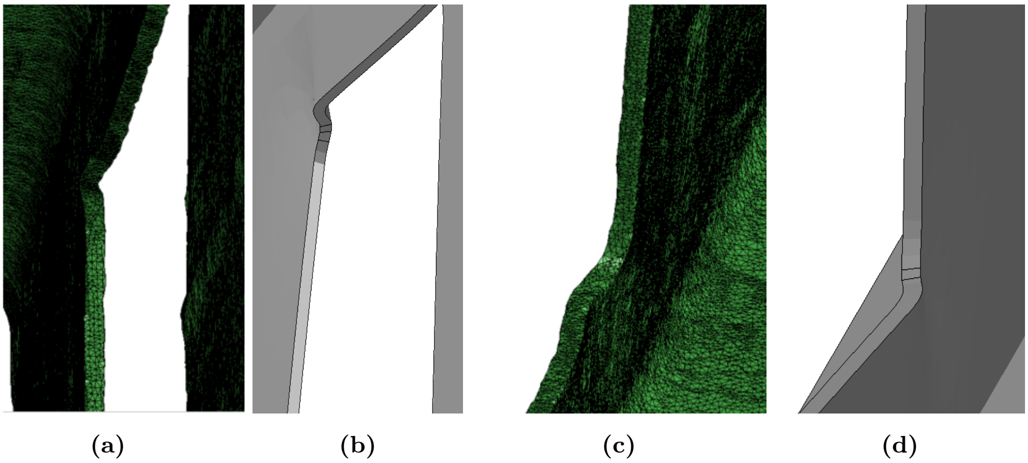
(a) (b) (c) (d)

Figure 4.5: Deformation shapes of the compressed opening corners. Figures (a) and (c) are 3D scans performed by Marthinussen and Sandnes [2, p. 44] of the top-left and bottom-right corners, respectively. Figures (b) and (d) are screenshots of the developed FE model.

Table 4.6 displays the maximum loads obtained from the numerical models, test results and EN 1993-1-13 (f_y = 446 MPa). They all indicate failure due to Vierendeel bending. Compared to the test results, the model using the 446 MPa yield strength is the closest to the actual value. Furthermore, the Eurocode design capacity largely underestimates the true beam capacity, similar to findings from previous studies conducted at NTNU.

Table 4.6: Maximum load of FE models, test results and EN 1993-1-13 for specimen A.

	Abaqus[1]	**Abaqus[2]**	**Abaqus[3]**	**Test Results**	**EN 1993-1-13**
Max. Load [kN]	216	195	214	228	167
Failure mode	Vierendeel bending	Vierendeel bending	Vierendeel bending	Vierendeel bending	Vierendeel bending

[1] Nonlinear strain hardening (f_y = 446 MPa),
[2] Linear strain hardening (f_y = 424 MPa),
[3] Marthinussen and Sandnes [2, p. 54] (f_y = 455 MPa).

4.4.2 Specimen B

Figure 4.6 displays the recorded response curve obtained from testing by Bjerch and Aksnes [4, p. 44] - shifted and corrected for stiffness - alongside the response curves generated by the numerical model of specimen B.

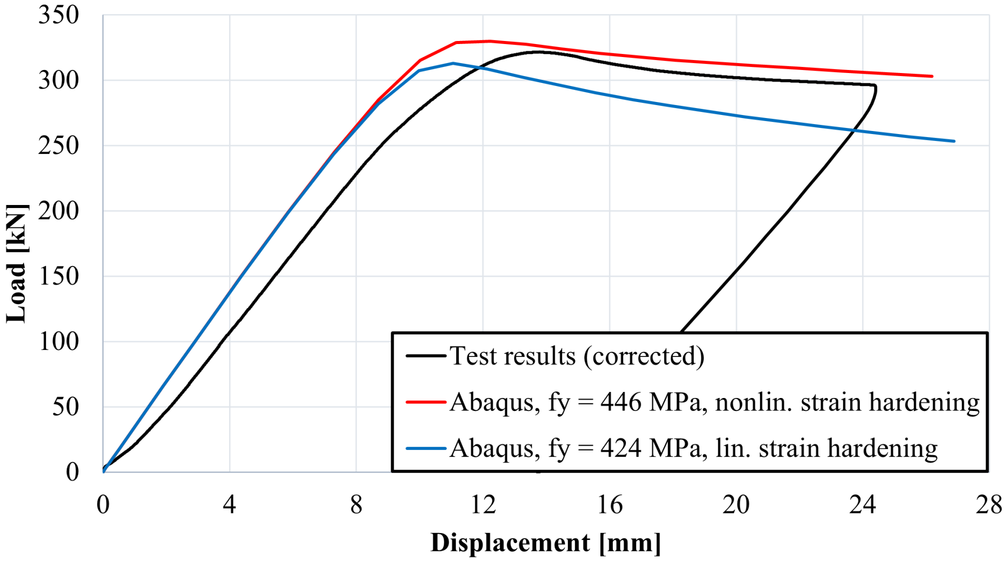

Figure 4.6: Response curves from the laboratory test and FE model of specimen B. The black curve represents the test results obtained by Bjerch and Aksnes [4, p. 44].

The response curves of the models closely resemble the test results, particularly for the stronger material input, indicating that the nonlinear strain hardening may be the most viable material model. However, there are minor discrepancies in strength and stiffness, which could be attributed to various model properties such as mesh, geometry, yield strength and buckling modes. The geometric imperfection study conducted by Bjerch and Aksnes [4, p. 45] demonstrates that it is possible to fine-tune the model properties, to precisely match the test results. This emphasizes how a general model may deviate from specific test results. Nevertheless, when comparing the opening deformations in the 3D scan and FE model presented in Figure 4.7, the model appears to accurately reproduce the correct failure mode.

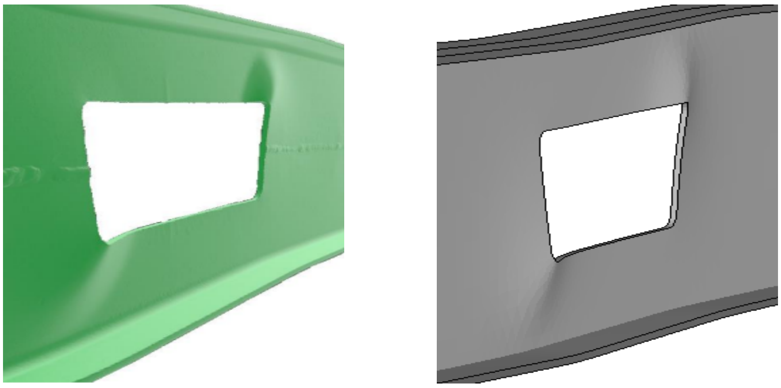

(a) (b)

Figure 4.7: Deformation shapes of the opening. Figure (a) is a 3D scan performed by Bjerch and Aksnes [4, p. 48]. Figure (b) is a screenshot of the developed FE model.

Furthermore, Table 4.7 provides an overview of the maximum load values obtained from the different numerical models, the test result and EN 1993-1-13, as well as their corresponding failure modes. Vierendeel bending is identified as the governing failure mode for both of the numerical models, testing and Eurocode calculations. The stronger material input overestimates the test result by 2.8 %, while the weaker material input underestimates them by 2.5 %. However, the Eurocode calculation significantly underestimates the true beam capacity, resulting in a maximum capacity that is only one third of the test result.

Table 4.7: Maximum load of FE models, the test result and EN 1993-1-13 for specimen B.

	Abaqus[1]	**Abaqus**[2]	**Abaqus**[3]	**Test Results**	**EN 1993-1-13**
Max. Load [kN]	330	313	321	321	104
Failure mode	Vierendeel bending	Vierendeel bending	Vierendeel bending	Vierendeel bending	Vierendeel bending

[1] Nonlinear strain hardening ($f_y = 446$ MPa),
[2] Linear strain hardening ($f_y = 424$ MPa),
[3] Bjerch and Aksnes [4, p. 37] ($f_y = 446$ MPa).

4.4.3 Specimen C

Figure 4.8 depicts the response curve obtained from the laboratory experiment conducted by Bjerch and Aksnes [4, p. 44], which has been shifted and corrected for stiffness, in comparison to the response curves generated by the numerical model for specimen C.

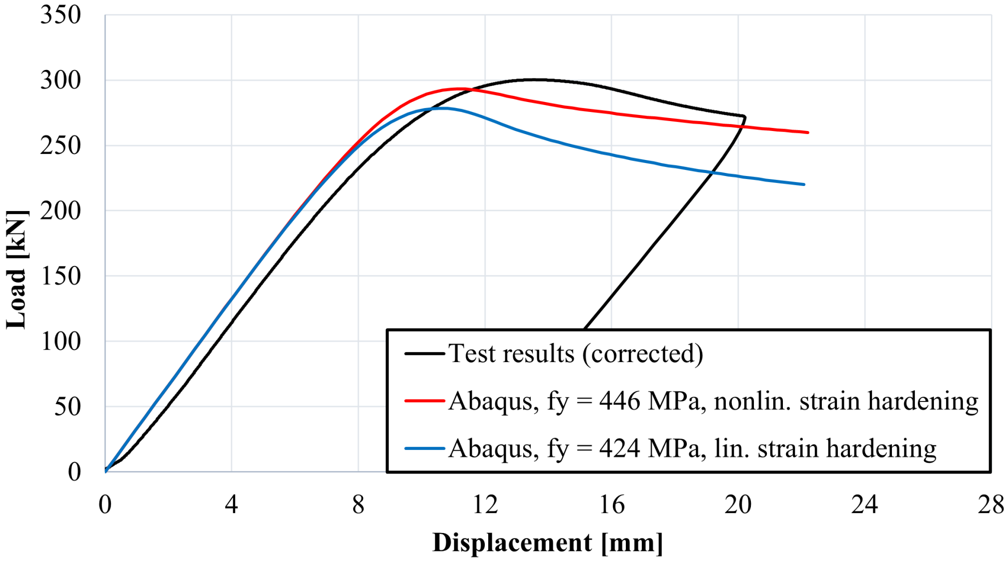

Figure 4.8: Response curves from the laboratory test and FE model of specimen C. The black curve represents the test results obtained by Bjerch and Aksnes [4, p. 44].

Although the load-resistances of the numerical models decline more rapidly than for the test after reaching the maximum load, they exhibit a similar shape in the response curve. This similarity may indicate that an appropriate imperfection shape was selected, despite the resistance being weaker after yield. Both numerical models, the test and the Eurocode all report Vierendeel bending as the critical failure mode. The resulting opening corner deformations are illustrated in Figure 4.9. Specifically, the Figures 4.9a and 4.9b depict largely similar deformations, particularly noticeable in the bottom-right opening corner.

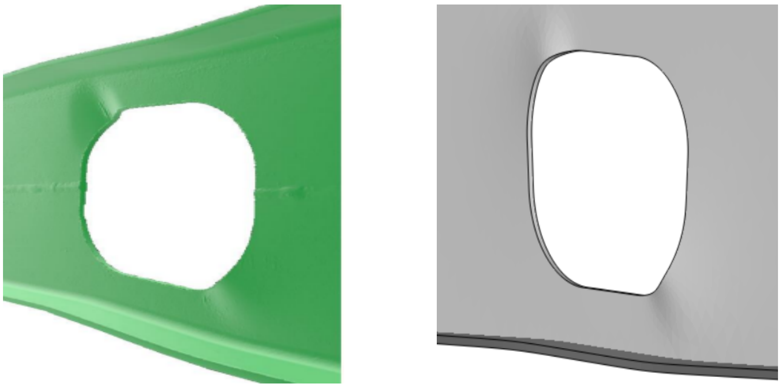

(a)

(b)

Figure 4.9: Deformation shapes of the opening. Figure (a) is a 3D scan performed by Bjerch and Aksnes [4, p. 52]. Figure (b) is a screenshot of the developed FE model.

Furthermore, Table 4.8 presents the maximum loads obtained from the two numerical models, the test result, and EN 1993-1-13, along with their respective failure modes. The numerical model consistently underestimates the laboratory results for both material inputs. When using the stronger material input, the maximum load reaches 293 kN, which is 2.3 % lower than the test result. This aligns with the reported maximum load of 296 kN obtained from the model of Bjerch and Aksnes [4, p. 50], which is 1.4 % lower than the test result. Moreover, the weaker material input underestimates the laboratory results by 7.9 %.

Table 4.8: Maximum load of FE models, test results and EN 1993-1-13 for specimen C.

	Abaqus[1]	**Abaqus**[2]	**Abaqus**[3]	**Test Results**	**EN 1993-1-13**
Max. Load [kN]	293	278	296	300	158
Failure mode	Vierendeel bending	Vierendeel bending	Vierendeel bending	Vierendeel bending	Vierendeel bending

[1] Nonlinear strain hardening ($f_y = 446$ MPa),
[2] Linear strain hardening ($f_y = 424$ MPa),
[3] Bjerch and Aksnes [4, p. 37] ($f_y = 446$ MPa).

Although, the Eurocode yet again underestimates the specimen's capacity, the underestimation is less pronounced compared to specimen B. Despite the Eurocode calculations allowing for the utilization of the beam's plastic capacity, the design resistance falls below 53 % of the actual load-carrying capacity of the specimen. This primarily arises as a consequence of the large opening corner radii not being taken into account in the calculations, which is an issue addressed in Section 5.2 of the parametric study.

4.4.4 Specimen D

Figure 4.10 shows the response curve obtained from the laboratory experiment conducted by Hovda and Hurum [3, p. 59], which has been shifted and corrected for stiffness, and compares it to the response curves generated by the numerical model of specimen D. As indicated by the two-part black curve, specimen D failed during testing and was loaded and unloaded three times in the process, where the second attempt was not recorded. The highest recorded value from testing was 255 kN. However, Hovda and Hurum [3, p. 59] estimates a maximum load of 267 kN based on the slope of their remaining response curve. Although it is difficult to quantify the specimen's maximum load, both the slope and magnitude of the response curves from Abaqus may be reasonable based on the last recorded load attempt of the experiment.

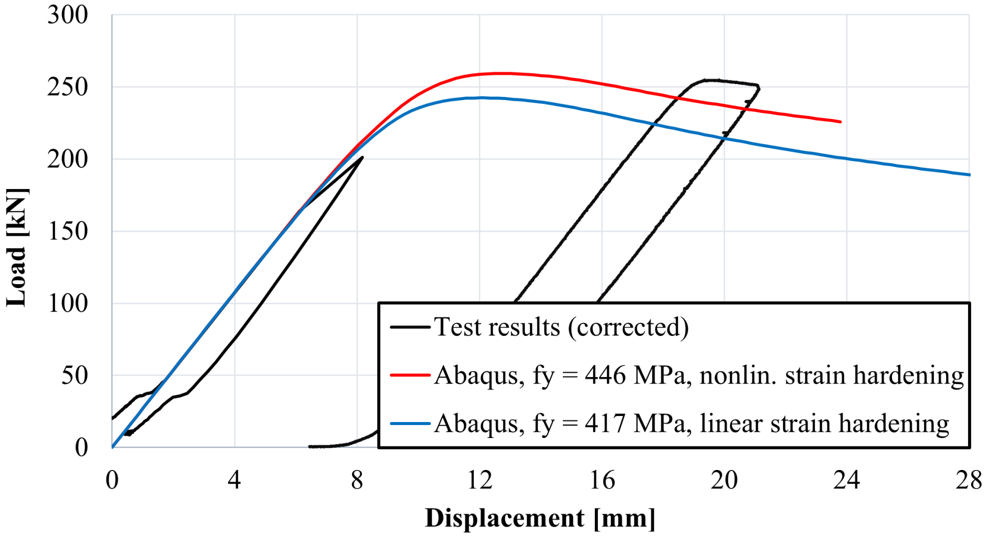

Figure 4.10: Response curves from test results and FE model of specimen D. The black curve is produced by Hovda and Hurum [3, p. 59].

Moreover, Figure 4.11 illustrates the opening deformations of the deformed specimen and the numerical model at maximum load. Although aligning the perspective between the 3D scan and numerical model is challenging due to different fields of view, the locations of the deformed opening corners appear to be very similar, particularly noticeable in the bottom-right corner due to the perspective.

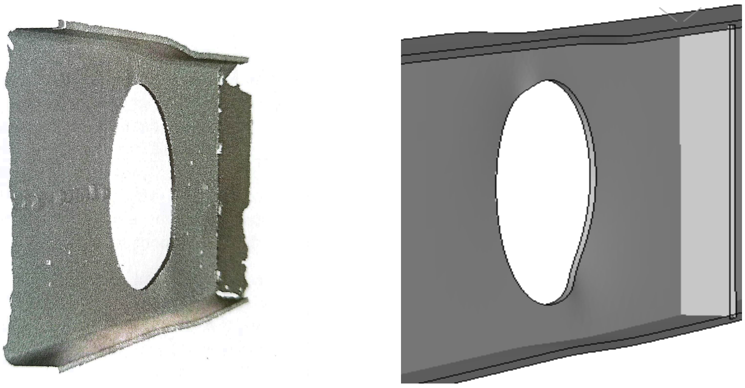

(a) **(b)**

Figure 4.11: Deformation shapes of the opening. Figure (a) is a 3D scan performed by Hovda and Hurum [3, p. 75]. Figure (b) is a screenshot of the developed FE model.

Table 4.9 provides a summary of the maximum loads and failure modes observed in the numerical models, test results and EN 1993-1-13. The maximum load achieved using the nonlinear material input exceeds the highest test result load by 1.6 %. However, it is assumed that this difference is smaller, if not nonexistent. Furthermore, while indicating the same failure modes, the Vierendeel bending design capacity in EN 1993-1-13 only reaches 70 % of the test results' maximum load.

Table 4.9: Maximum load of FE models, test results and EN 1993-1-13 for specimen D.

	Abaqus[1]	**Abaqus**[2]	**Abaqus**[3]	**Test Results**	**EN 1993-1-13**
Max. Load [kN]	259	242	263	255	185
Failure mode	Vierendeel bending	Vierendeel bending	Vierendeel bending	Vierendeel bending	Vierendeel bending

[1] Nonlinear strain hardening (f_y = 446 MPa),
[2] Linear strain hardening (f_y = 424 MPa),
[3] Hovda and Hurum [3, p. 48] (f_y = 438 MPa).

4.4.5 Specimen E

Figure 4.12 shows the laboratory recorded response curve of Hovda and Hurum [3, p. 57], which has been shifted and corrected for stiffness, compared to the response curves of the numerical model for specimen E. When compared to the test results, it is evident that both material inputs' response curves exhibit a rapid decline after reaching the maximum load. Moreover, both the FE model developed by Hovda and Hurum [3, p. 71] and the model incorporating the stronger material input, as depicted with the red curve in Figure 4.12, overestimate the capacity of the specimen. The latter reaches a maximum load-carrying capacity that is 2.6 % larger than the test results, while the model with the weaker material input underestimates its capacity by 5.6 %.

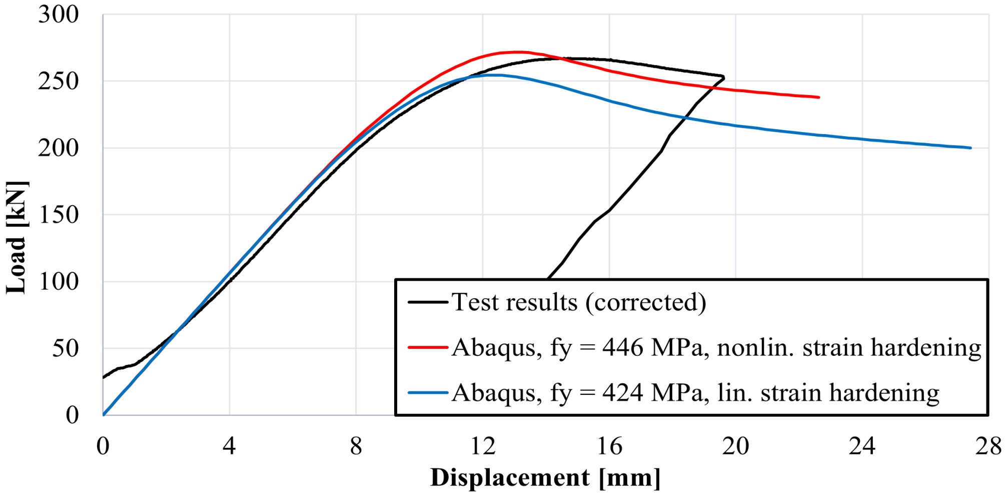

Figure 4.12: Response curves from test results and FE model of specimen E. The black curve is produced by Hovda and Hurum [3, p. 57].

Similar to specimen A, the testing of specimen E was terminated shortly after reaching the maximum load, making it more challenging to compare strain hardening behavior. However, inspecting the response curves after the yielding is initiated, it becomes evident that the linear strain trend yet again is too soft to accurately represent the physical beam response. Uncharacteristically, the response curve of the model employing the stronger material input exhibits an even steeper decline after reaching the maximum load compared to the linear strain hardening model. This discrepancy could be attributed to excessive distortions present in the 20:5 mesh, closely resembling anomalies observed in the coarser meshes previously discussed in Section 4.3.

Furthermore, since displacement directions of the deformed web-posts, shown in Figure 4.13, are opposite between Figures 4.13a and 4.13b, it becomes challenging to ascertain whether the correct deformation shape of the web-post has been achieved. However, it is evident that the critical failure in both the experiment and the numerical model occurs in the web-post. Moreover, the occurrence of plastic hinges in the web-post appears to be located at similar positions.

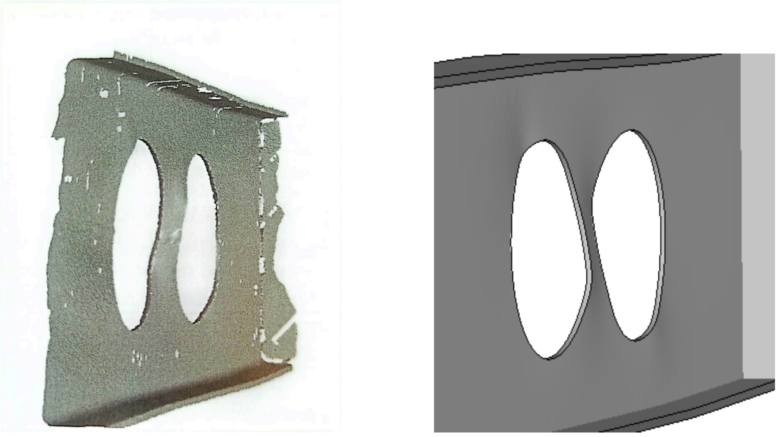
(a) (b)

Figure 4.13: Deformation shapes of the opening. Figure (a) is a 3D scan performed by Hovda and Hurum [3, p. 73]. Figure (b) is a screenshot of the developed FE model.

The maximum load and failure mode of the different material input models, test result and EN 1993-1-13 for specimen E, are presented in Table 4.10. According to the Eurocode, the critical failure mode is horizontal shear at the web-post. Although distinguishing between the web-post shear and buckling is difficult, the numerical models indicate web-post buckling as the failure mode. Moreover, Hovda and Hurum [3] do not explicitly mention the failure mode of Specimen E. Whether the Eurocode provides a more precise definition of the failure mode is not possible to determine, since the design load only reaches 68 % of the specimen's actual load-carrying capacity.

Table 4.10: Maximum load of FE models, test results and EN 1993-1-13 for specimen E.

	Abaqus[1]	**Abaqus**[2]	**Abaqus**[3]	**Test Results**	**EN 1993-1-13**
Max. Load [kN]	272	254	269	265	181
Failure mode	Web-post buckling/ shear	Web-post buckling/ shear	Web-post buckling/ shear	Web-post buckling	Web-post shear

[1] Nonlinear strain hardening (f_y = 446 MPa),
[2] Linear strain hardening (f_y = 424 MPa),
[3] Hovda and Hurum [3, p. 48] (f_y = 438 MPa)

4.4.6 Specimen F

Figure 4.14 displays the response curve of the numerical model and test results for specimen F. In this case, both material inputs overestimate the maximum load compared to the test results. The stronger material input model exceeds the test results by 9.4 %, while the weaker input exceeds it by less than 1 %. This may suggest that $f_y = 424$ MPa is closer to the material yield strength of the specimen.

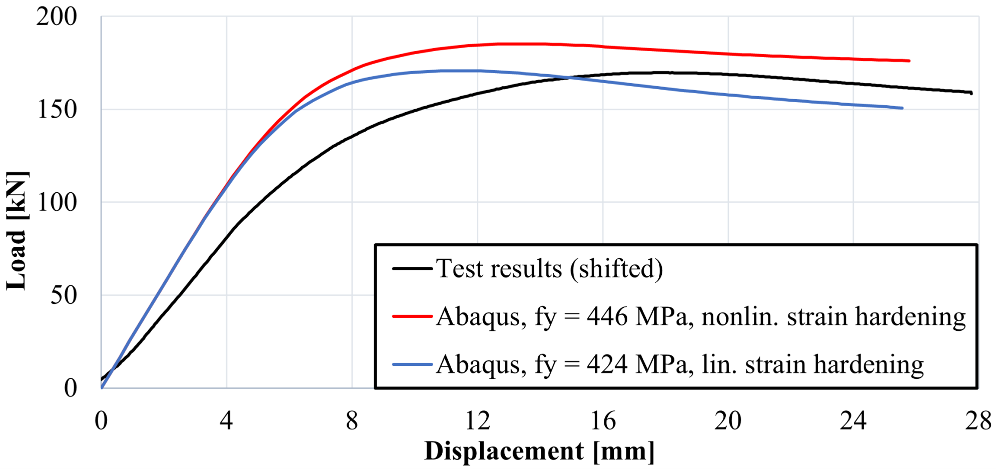

Figure 4.14: Response curves from the test result and the FE model of specimen F.

The response curve of the weaker material input shows a softer behavior after reaching the maximum load, obtaining a larger load decrease per mm displacement. However, the response curve of the stronger material input closely resembles the trend of the test results' response after the maximum load. When examining the comparison of response curves for specimen F independently, it appears that using a combination of the two material inputs can be an optimal approach, incorporating a yield strength of 424 MPa and nonlinear strain hardening.

While the experiment results for specimens A-E have been corrected and adjusted for the stiffness of their test rigs, specimens F and G have not undergone such adjustments. To facilitate comparison, Figure 4.15 shows the response curves for specimen F, including a response curve that has been adjusted to match the stiffness of the Abaqus models. This adjustment aims to eliminate the difference in elastic stiffness, according to Equation 1, where $k_{\text{experiment}}$ and k_{Abaqus} represent the constant stiffness values from the linear elastic portion of the response curves. Utilizing a weighted difference in stiffness, every displacement increment of the test, $w_{\text{i,old}}$, is updated to obtain a new displacement value, $w_{\text{i,new}}$, paired with the corresponding load increment, F_{i}. Accordingly, a new displacement pattern is derived.

$$w_{\text{i,new}} = w_{\text{i,old}} + \frac{k_{\text{experiment}} - k_{\text{Abaqus}}}{k_{\text{experiment}} \cdot k_{\text{Abaqus}}} \cdot F_i \tag{1}$$

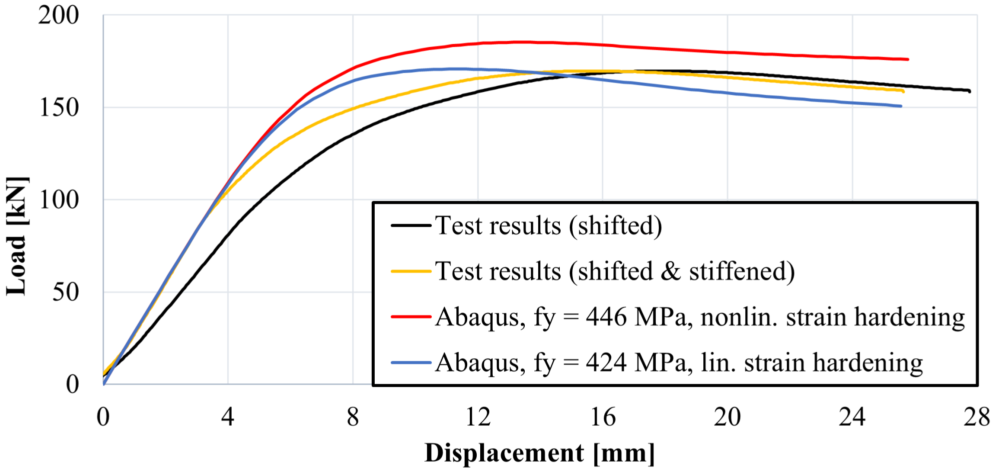

Figure 4.15: Response curves of specimen F, including the curve adjusted to match the FE model's elastic stiffness.

As a result, it becomes evident that the nonlinear strain hardening model closely replicates the shape of the response curve observed in the experiment. However, notable disparities exist between the numerical models and the experiment, leading to a higher load-carrying capacity in the numerical models. These differences may arise from variations in yield strength, geometric imperfections, inaccuracies in the experimental setup, as well as an overly stiff element model.

The maximum load and failure modes of the different material inputs, test results and EN 1993-1-13 of specimen F are presented in Table 4.11. All models display Vierendeel bending as the failure mode, and the Eurocode calculations are able to estimate 70 % of the actual beam capacity when using a yield strength of 446 MPa. However, by inspecting the response curves it is clear the nonlinear behavior in the specimen starts before the yielding of the linear strain hardening model using $f_\mathrm{y} = 424$ MPa.

Table 4.11: The maximum load of the FE models, test results and EN 1993-1-13 for specimen F.

	Abaqus[1]	**Abaqus**[2]	**Test Results**	**EN 1993-1-13**
Max. Load [kN]	186	171	170	120
Failure mode	Vierendeel bending	Vierendeel bending	Vierendeel bending	Vierendeel bending

[1] Nonlinear strain hardening ($f_y = 446$ MPa),
[2] Linear strain hardening ($f_y = 424$ MPa)

Figures 4.16a and 4.16b show the maximum in-plane principal strains around the opening of specimen F. Both plots represent the response for the same load situation after maximum load, specifically at 160.7 kN, near the end of the experiment. A key difference is the corresponding displacement, Δ, partly because the slack of the test rig contributes to the measured displacement during the experiment. Moreover, since the numerical model shows stiffer behavior and higher capacity, the compared opening deformations at equal load are likely given for different stages.

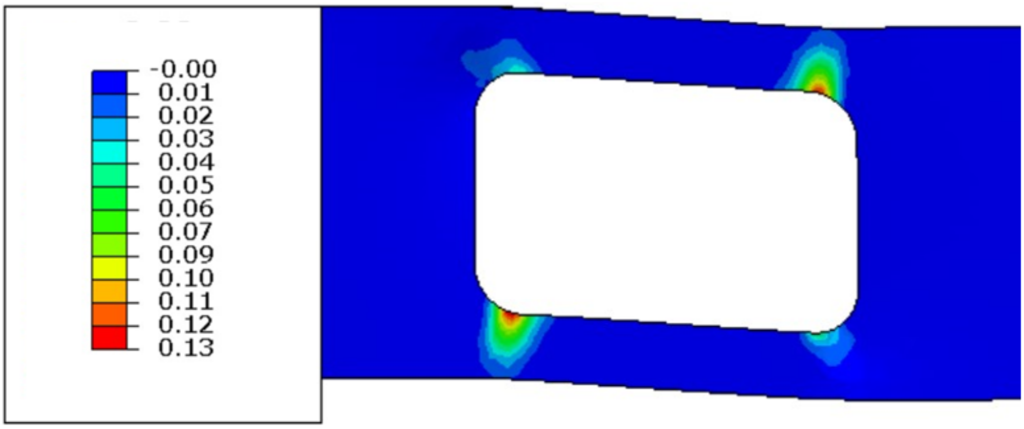

(a) Abaqus model run with linear strain hardening (f_y = 424 MPa). Values taken at F = 160.7 kN, Δ = 17.1 mm.

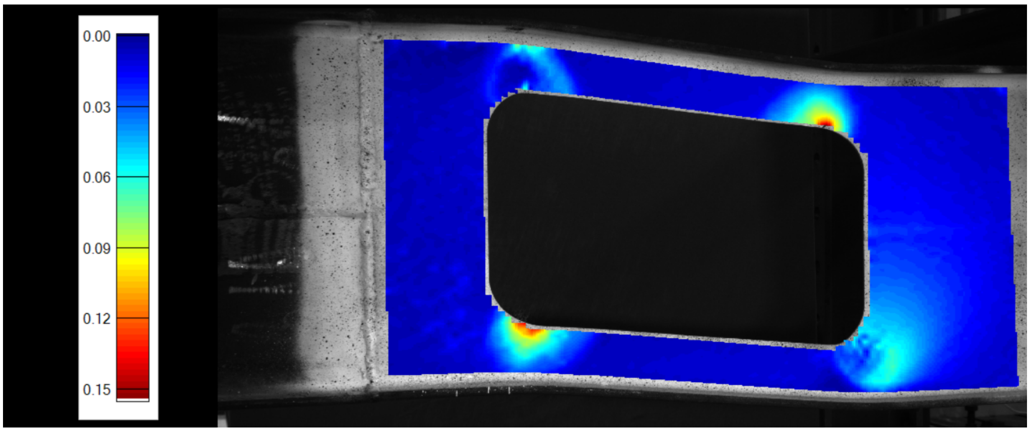

(b) 2D DIC from experiment. Values taken at F = 160.7 kN, Δ = 26.4 mm.

Figure 4.16: The maximum in-plane principal strains [-] of specimen F.

Observing the in-plane opening deformation, both the physical specimen and the numerical model obtain similar shapes, although at different scales, for the same external load, further suggesting a valid failure mode in the numerical model. Figure 4.16 further shows the critical locations for tension strains at the bottom-left and top-right corners, which is evidence of Vierendeel bending. The weak strain patterns appearing at the two remaining opening corners are likely the result of the heavily deformed corners in compression. Moreover, the strain values are not directly comparable, since the 2D DIC is unable to take the out-of-plane displacements into account.

Figures 4.17a and 4.17b show the minimum in-plane principal strains around the opening of specimen F. Both plots represent the same load situation as Figure 4.16. Figure 4.17 shows the critical locations for compressive strains at the bottom-right and top-left corners, which is further evidence of Vierendeel bending. Although reporting very different strain values, both figures show the largest values at the bottom-right corner, which notably is the location with the clearest observed deformations during the experiment. Importantly, this location corresponds to the buckling mode with the second smallest positive eigenvalue in the numerical model, while the top-left opening corner corresponds to the smallest positive eigenvalue.

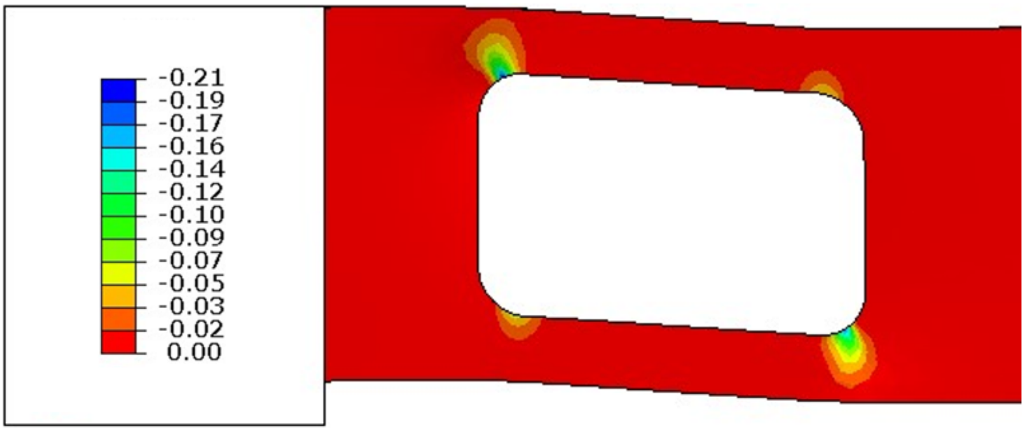

(a) Abaqus model run with linear strain hardening (f_y = 424 MPa). Values taken at F = 160.7 kN, Δ = 17.1 mm.

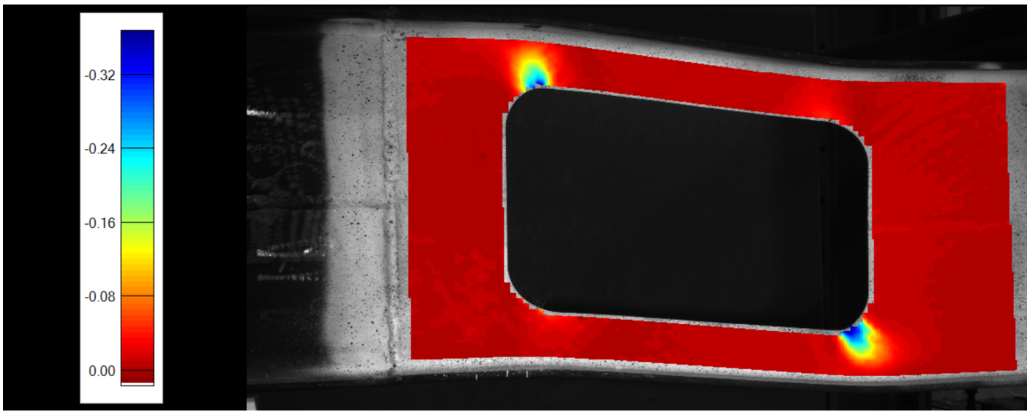

(b) 2D DIC. Values taken at F = 160.7 kN, Δ = 26.4 mm.

Figure 4.17: The minimum in-plane principal strains [-] of specimen F.

4.4.7 Specimen G

As mentioned in Section 2.3, the web opening of specimen G was unintentionally cut 10 mm closer to the beam's top flange, theoretically lowering its capacity. Figure 4.18 shows the difference in opening placement in the numerical model with and without an offset of 10 mm from the cross section's neutral axis, towards the top flange. Based on the small difference in maximum capacity shown in the figure, it is assumed that this offset has little to no influence on the results. The difference in maximum capacity for both material models is 1 %. Therefore, due to considerably more tedious Eurocode calculations for asymmetrically placed web openings, a symmetrically placed web opening will be used for comparisons when calculating Eurocode design capacities. However, the true measured geometry with the opening offset will be used in the numerical models.

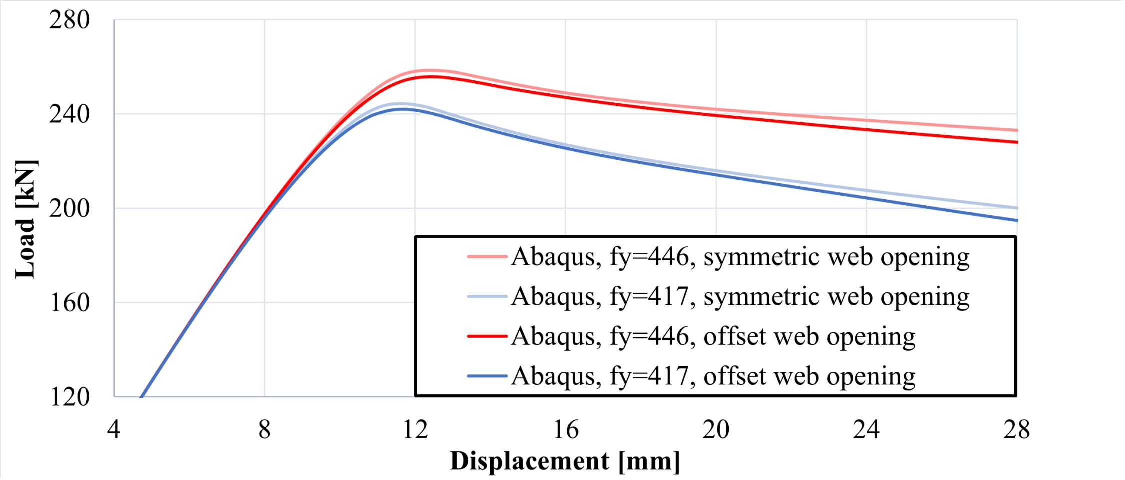

Figure 4.18: The response curves of the model of specimen G with a symmetrically located web opening and a 10 mm offset web opening. Ultimate load area is zoomed in on, to show dissimilarities more clearly.

Figure 4.19 shows the response curve of the numerical models compared to the experiment of specimen G. The maximum load is overestimated by 9.4 % and 3.4 % for the nonlinear and linear strain hardening models, respectively. Similar to specimen F, the weaker material input model's maximum load fits relatively well, but its strength declines too rapidly. This indicates that f_y = 417 MPa may be more realistic, although with the nonlinear strain hardening model after yielding.

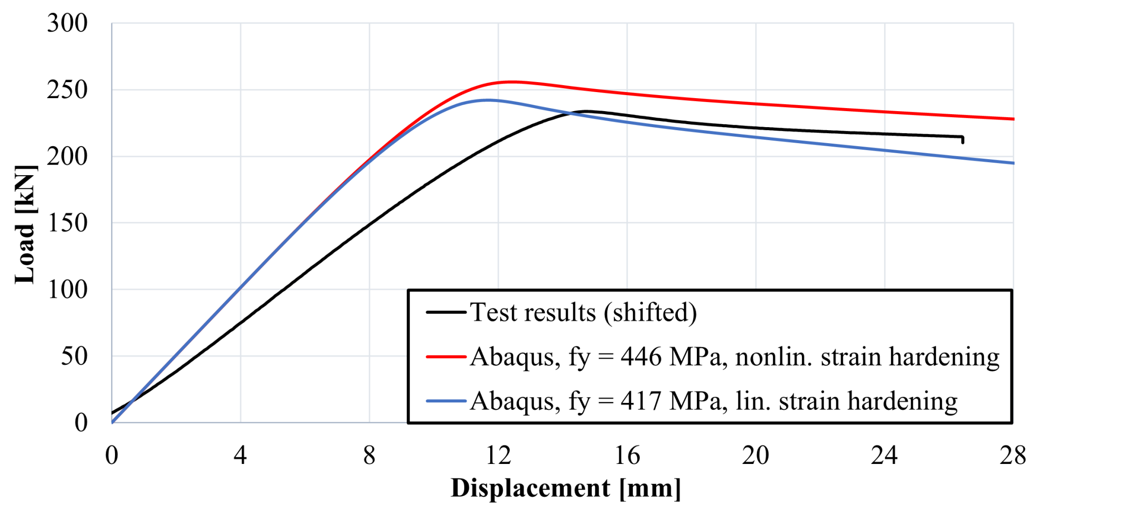

Figure 4.19: Response curves from test results and FE model of specimen G.

Similarly to specimen F, in Figure 4.20, the response curve's stiffness for specimen G has been adjusted to fit the numerical model. Comparing the adjusted test results to the numerical model with lower yield strength, a very similar response up to and around the maximum load is observed, with only a 3.4 % deviation in the maximum load. However, it becomes more evident that the material model is based on linear strain hardening.

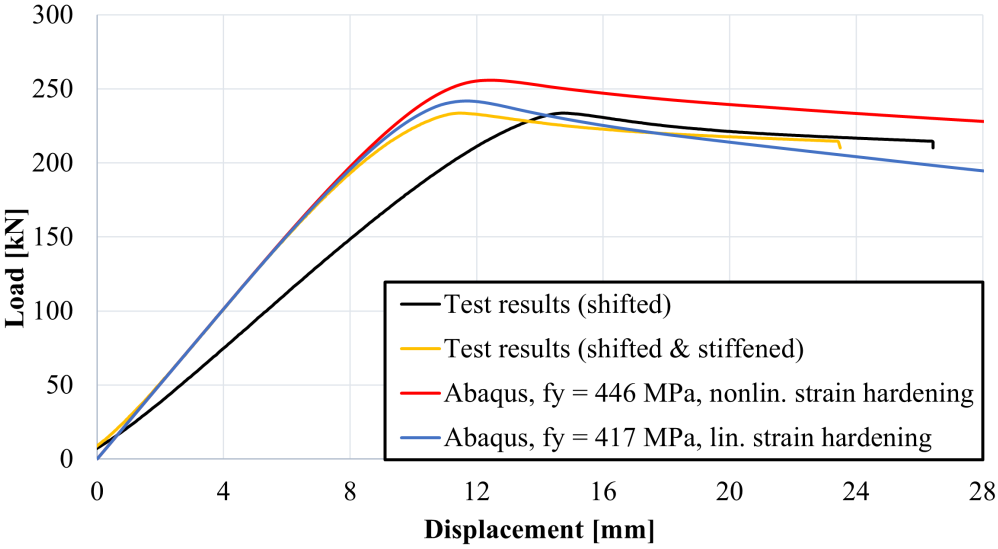

Figure 4.20: The response curves with the results of specimen G adjusted to the FE model's stiffness.

The maximum load and failure mode of the numerical models with different material inputs, experiment results and EN 1993-1-13 calculations of specimen G are presented in Table 4.12. The opening geometry was designed specifically to obtain Tee section class 3 in Vierendeel bending, when reducing the class according to the design rules of the Eurocode. Therefore, the use of elastic design capacity is required, which results in the calculated maximum design load of EN 1993-1-13 reaching only 35 % of the test result's load-carrying capacity.

Table 4.12: The maximum load of the FE models, test results and EN 1993-1-13 for specimen G.

	Abaqus[1]	**Abaqus[2]**	**Test Results**	**EN 1993-1-13**
Max. Load [kN]	256	242	234	81.7
Failure mode	Vierendeel bending	Vierendeel bending	Vierendeel bending	Vierendeel bending

[1] Nonlinear strain hardening (f_y = 446 MPa),
[2] Linear strain hardening (f_y = 424 MPa)

Figure 4.21 shows the maximum in-plane principal strains of specimen G with the numerical model and 2D DIC for the last increments of the four-point bending test. Both Figures 4.21 and 4.22 represent the in-plane principal strain situation for a load of 210 kN (after maximum load), while the corresponding displacements are different. Figures 4.22a and 4.22b display similar strain patterns for the minimum in-plane principal strains, although the largest strains are reached at opposite opening corners. This difference could be a result of somewhat dissimilar deformation shapes at the compressed opening corners.

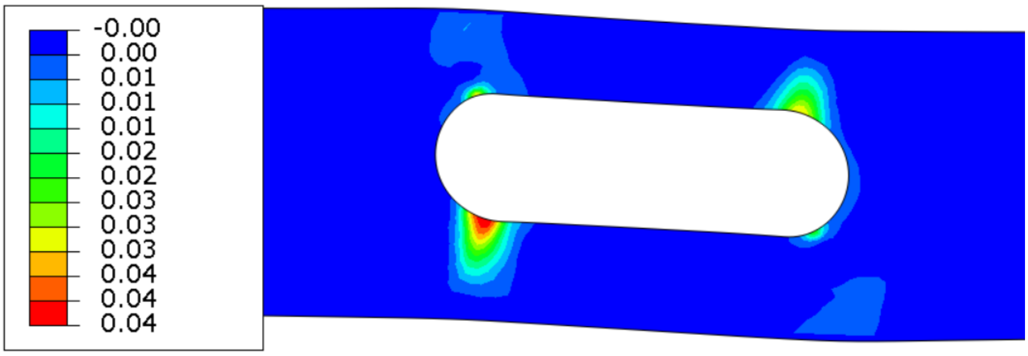
-0.00
0.00
0.01
0.01
0.01
0.02
0.02
0.03
0.03
0.03
0.04
0.04
0.04

(a) Abaqus model run with linear strain hardening (f_y = 417 MPa). Values taken at F = 210 kN, Δ = 21.5 mm.

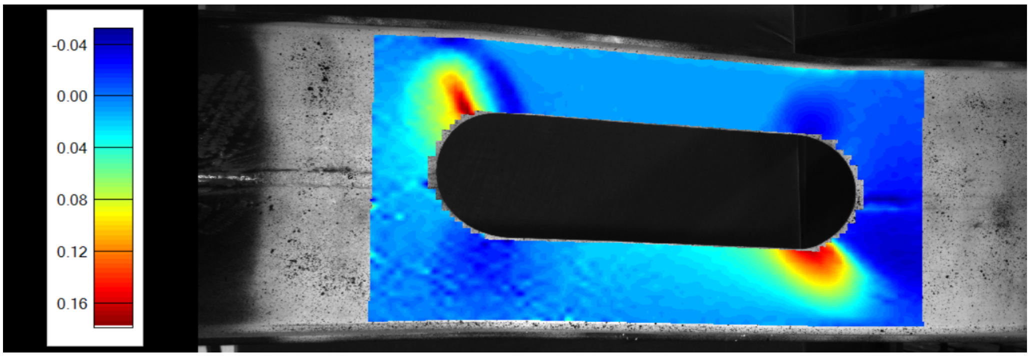
-0.04
0.00
0.04
0.08
0.12
0.16

(b) 2D DIC. Values taken at F = 210 kN, Δ = 27.1 mm.

Figure 4.21: Maximum in-plane principal strains [-] of specimen G.

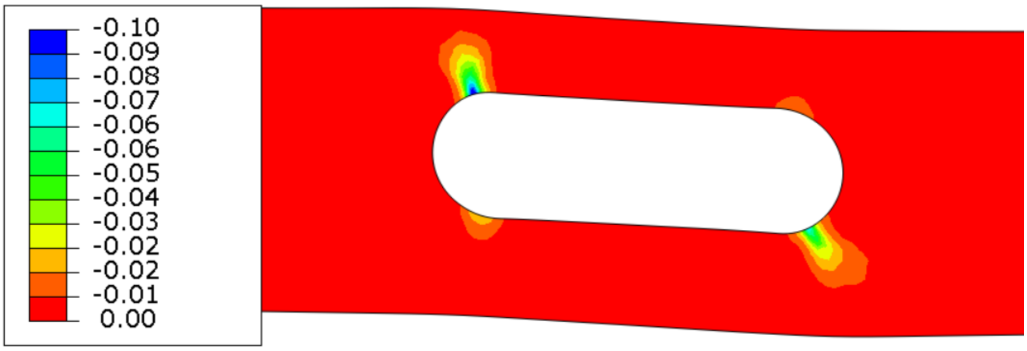
-0.10
-0.09
-0.08
-0.07
-0.06
-0.06
-0.05
-0.04
-0.03
-0.02
-0.02
-0.01
0.00

(a) Abaqus model run with linear strain hardening (f_y = 417 MPa). Values taken at F = 210 kN, Δ = 21.5 mm.

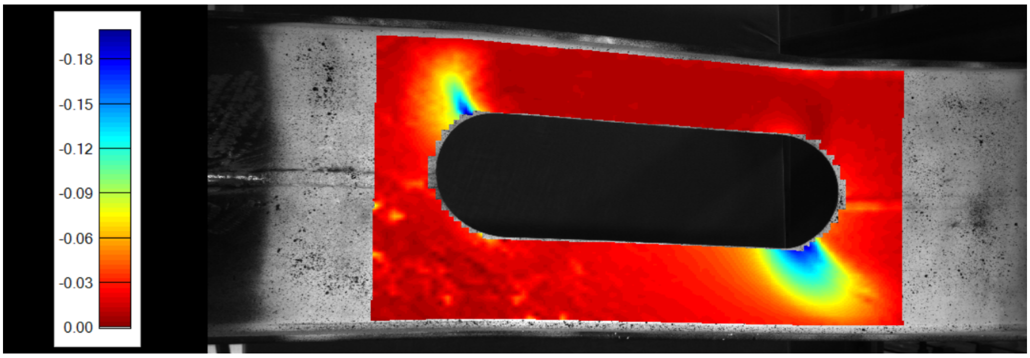
-0.18
-0.15
-0.12
-0.09
-0.06
-0.03
0.00

(b) 2D DIC. Values taken at F = 210 kN, Δ = 27.1 mm.

Figure 4.22: Minimum in-plane principal strains [-] of specimen G.

While Figure 4.21a shows the maximum in-plane principal strains of the numerical model at the bottom-left and top-right corners as expected, the DIC analysis in Figure 4.21b displays the two opposite corners: the upper-left and bottom-right. Consequently, Figure 4.21b is considered an error, since the maximum in-plane principal strains at the surface are displayed with almost the exact same pattern as the minimum in-plane principal strains in Figure 4.22b.

4.5 Assessment of the Numerical Model Precision

To summarize, observations indicate that all seven models achieve similar deformation shapes, though quantifiable measurements of the deformations for precise comparisons were unobtainable. For specimens A-E, a material model with nonlinear strain hardening and a yield strength of 446 MPa was found to generally provide the most accurate results compared to the experiments. It estimated both the maximum loads and the shapes of the response curves after the maximum load more accurately than the average material properties used by Grønland [5, p. 8]. All of these models produced maximum loads in the range ± 3 % of the experimental maximum loads.

However, when considering specimens F and G, the nonlinear material input model describes the response after the maximum load well, but overestimates the maximum load by 9 % in both cases. It is suggested that this larger deviation is mainly influenced by large mesh distortions, in addition to the existing deformations of the beams and possibly a lower yield strength as reported by Grønland [5].

Through mesh convergence studies, it is observed that the chosen mesh, used for all models in the subsequent parameter study, results in a 6 % larger capacity for specimen F and a 2 % larger capacity for specimen B. The larger error in capacity estimation is likely due to greater mesh distortions caused by the larger opening size. Consequently, a model error of ± 3 % must be expected, anticipated to increase to a 9 % overestimation in maximum capacity for openings causing severe mesh distortions in the opening region.

5 Parameter Study

In this section, a parameter study of opening shapes, the effect of corner radius for rectangular openings, opening positions and plastic design capacity of Tees, as well as definitions of small openings are presented. The analysis focuses on the maximum load obtained from numerical models in comparison to the ultimate design capacity determined by the Eurocode. Additionally, the corresponding failure modes are evaluated and compared. In the parameter study, a total of 128 different finite element analyses are presented and compared to Eurocode design capacities. The parameters considered in the study are opening shape, height and length, moment-shear ratio at the opening center and the Tee section class, which is manipulated by altering the web thickness.

5.1 Identification of Failure Modes

In order to evaluate the accuracy of specific ultimate design capacity clauses of the Eurocode, it is necessary for the failure modes identified by the Eurocode and the analysis to align. If there is a disagreement between the Eurocode and the model regarding the reason for failure, a simple comparison of maximum loads becomes less meaningful. For any given beam geometry, the design failure of the Eurocode is unambiguous. However, for each FE analysis, determining the failure mode by the model requires interpretation. In some cases, one failure mode may dominate, making the result explicit. However, often it is challenging to distinguish between multiple failure modes, as their combined effects influence the model's results.

When distinguishing the failure modes of the model, particular attention was given to studying the stress distribution and out-of-plane displacement of the beams' webs. For reference, clear examples of Vierendeel bending, web buckling and bending moment at midspan failures, are described in Figures 5.1, 5.2 and 5.4 below. Additionally, the most frequent combination of failure modes, namely Vierendeel bending and web buckling, as well as Vierendeel bending and bending moment at midspan, are presented in Figures 5.3 and 5.5, respectively.

Figure 5.1 showcases a clear example of the stress distribution and out-of-plane displacements of the beam opening region during Vierendeel bending. Stress concentrations can be observed at the corners of the opening, while displacements are particularly noticeable at the corners experiencing compression. One characteristic feature of the Vierendeel bending failure is that the sign of the out-of-plane displacement is identical for both opening corners in compression.

Likewise, Figure 5.2 illustrates a typical scenario of stress distribution and out-of-plane displacements of the beam opening region during web buckling next to the opening. Similarly, stress concentration is also observed at the corners of the opening. However, in web buckling, the out-of-plane displacements of the opening corners in compression are located adjacent to the opening, rather than above or below it. Additionally, the amplitudes of the web buckling on either side of the opening frequently have opposite signs.

Furthermore, Figure 5.3 displays an example where the stresses and out-of-plane displacements of the beam opening region are influenced by the combined effect of Vierendeel bending and web buckling. The stress distribution and out-of-plane displacement values resemble those of Vierendeel bending shown in Figure 5.1. However, similar to the web buckling scenario depicted in Figure 5.2, the out-of-plane displacements are positioned more towards the side of the opening.

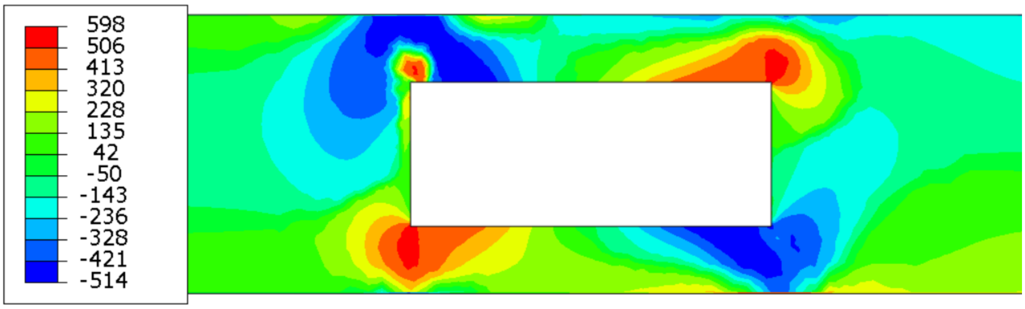

(a) Maximum and minimum in-plane principal stress [MPa].

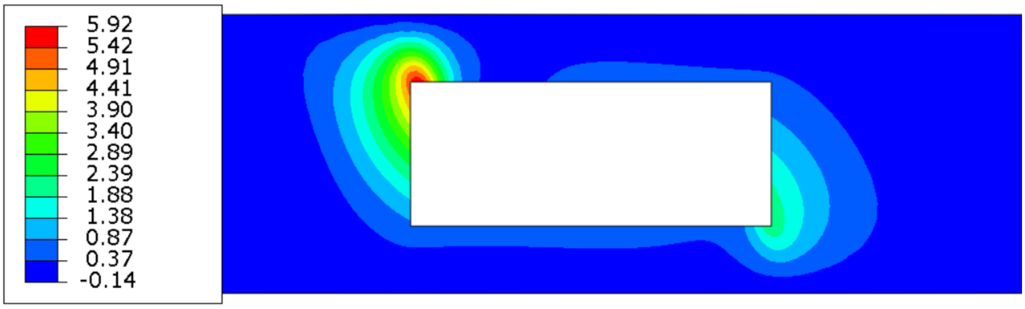

(b) Out-of-plane displacements [mm].

Figure 5.1: Example of Vierendeel bending failure. Stress distribution and out-of-plane displacements around an opening with dimensions: $h_o = 200$ mm, $a_o = 500$ mm.

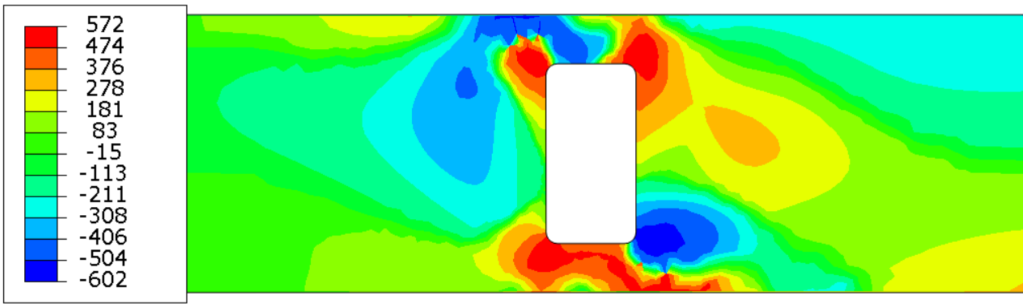

(a) Maximum and minimum in-plane principal stress [MPa].

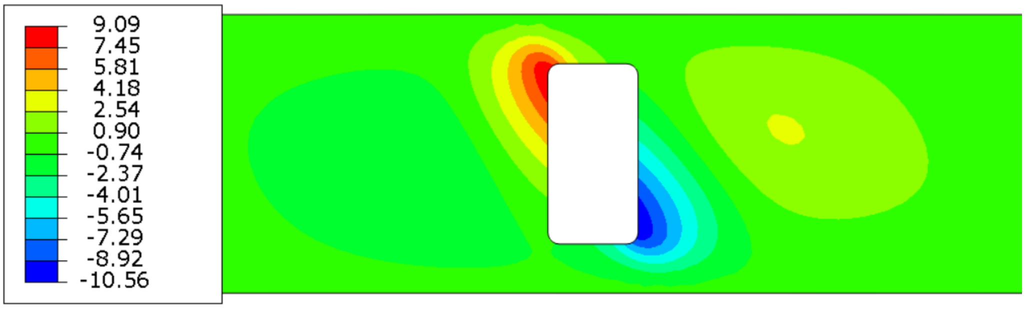

(b) Out-of-plane displacements [mm].

Figure 5.2: Example of web buckling failure. Stress distribution and out-of-plane displacements around an opening with dimensions: $h_o = 250$ mm, $a_o = 150$ mm, $r_o = 16$ mm and $t_w = 4$ mm.

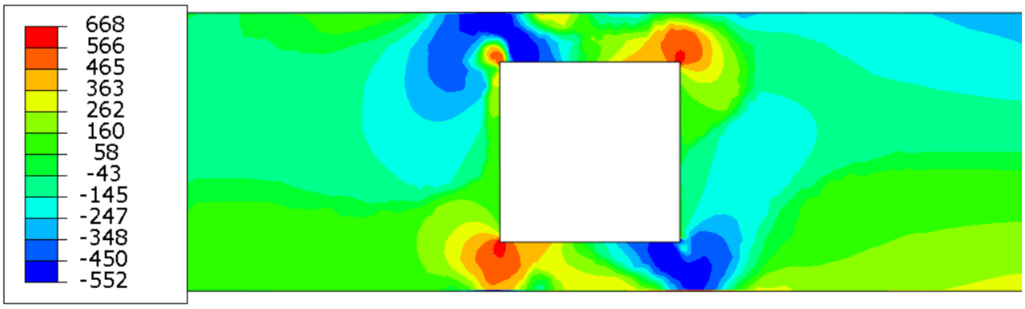

(a) Maximum and minimum in-plane principal stress [MPa].

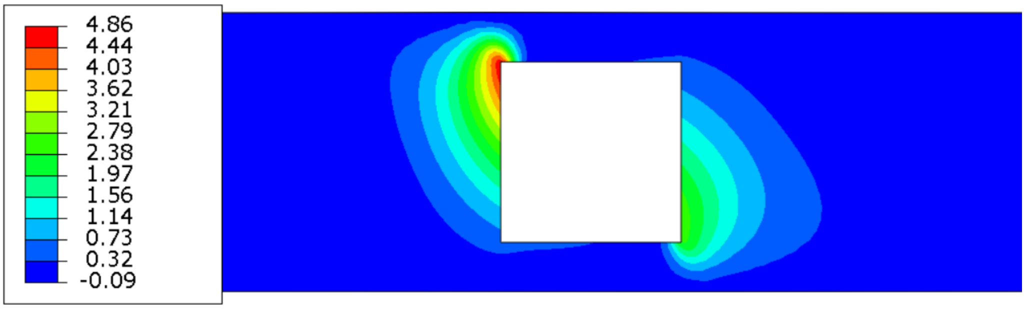

(b) Out-of-plane displacements [mm].

Figure 5.3: Example combination of Vierendeel and web buckling failure - Stress distribution and out-of-plane displacements around an opening with dimensions: $h_o = 250$ mm, $a_o = 250$ mm.

In Figure 5.4, the stress and displacements at midspan resulting from failure due to bending moment at midspan are depicted. For models with small or no openings, bending at midspan is generally the dominant failure mode. While stress concentrations still develop around the web opening, they have a negligible impact on the ultimate load-carrying capacity of the beam. Out-of-plane displacements play a lesser role in defining the bending moment at midspan as a failure mode.

Furthermore, Figure 5.5 presents the stress distribution and out-of-plane displacements of a case where the opening region's capacity converges on the capacity of the bending moment at midspan. In this case, the stresses of similar magnitude increase around the beam opening and at midspan before eventually reaching failure at the maximum load. In such cases, examining the response curve aids in distinguishing the failure modes. If the beam first fails due to the bending moment at midspan, the failure mode of the opening follows shortly after, visible from a sudden drop in capacity along the response curve after maximum load. An example of such a response curve is shown in Appendix C, Figure C.5.

In Figure 5.5, the specific combination of Vierendeel and moment at midspan failure is shown. Combinations of web buckling and bending moment at midspan failure, as well as combinations of all three failure modes may occur. Deciding on either of the failure modes in borderline scenarios like these is often futile, nor correct, as the numerical model only approximates the solution. Therefore, in the following sections, when the maximum loads of the different failure modes are within the estimated ±3 % precision of the numerical model (see Section 4.5), their combination is reported. For consistency, the same limit is applied to the reported capacities of the Eurocode clauses.

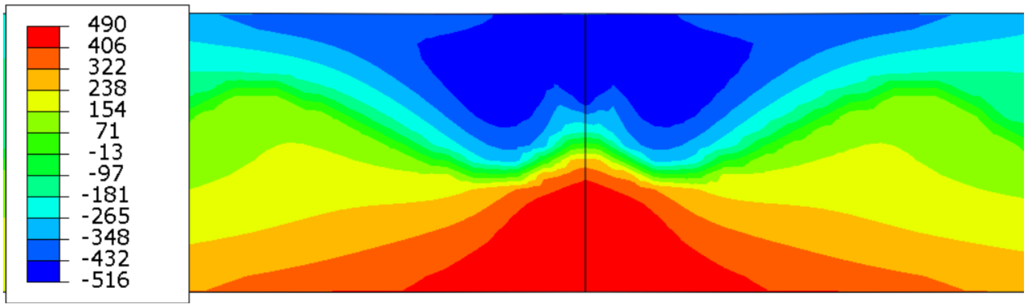

(a) Maximum and minimum in-plane principal stress [MPa].

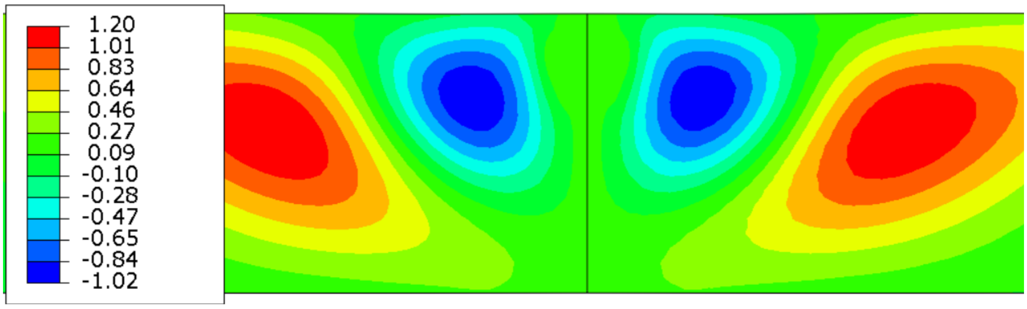

(b) Out-of-plane displacements [mm].

Figure 5.4: Bending moment at midspan failure. The stress distribution and out-of-plane displacements at midspan of beam specimen F without web opening.

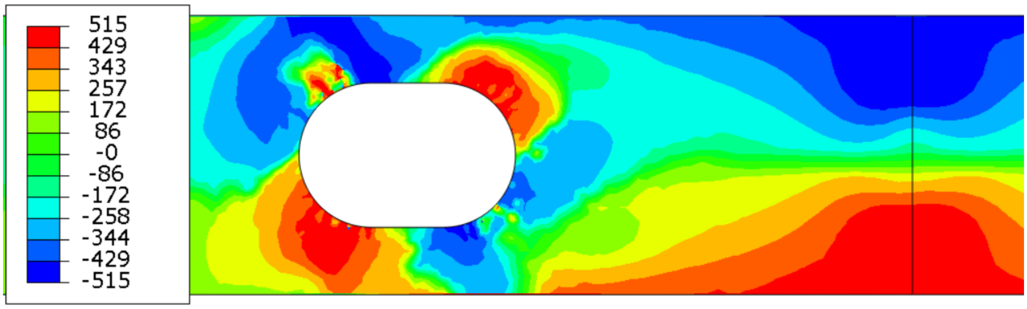

(a) Maximum and minimum in-plane principal stress [MPa].

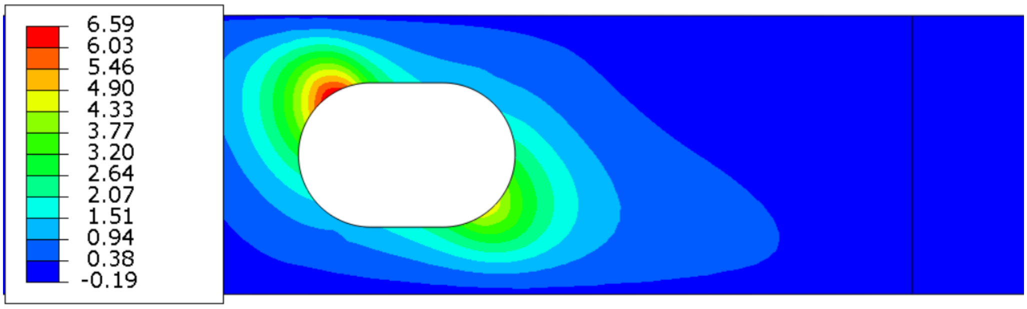

(b) Out-of-plane displacements [mm].

Figure 5.5: Combination of Vierendeel and moment at midspan failure - Stress distribution and out-of-plane displacements at midspan and around an elongated opening with dimensions: h_o = 200 mm, a_o = 300 mm.

5.2 Opening Corner Radius in Eurocode Design Capacity

While design checks in EN 1993-1-13 account for the rounded corners of both circular and elongated openings, the design checks for rectangular openings do not. Consequently, significant transitions in Eurocode design capacity occur between rectangular openings with rounded corners and elongated or circular openings. This issue was addressed by both Bjerch and Aksnes [4, p. 73] and Grønland [5, p. 45], where the former devised two formulas to rectify the design capacity transition. Their proposed formulae incorporate the opening corner radius, r_o, when calculating the equivalent lengths, a_eq, and the equivalent heights, h_eq, based on EN 1993-1-13 Table 8.3, as shown in Equations (2) and (3). The equivalent dimensions transition to the dimensions specified by the Eurocode for the elongated openings when the rounded opening corners eventually align, at $r_\text{o} = h_\text{o}/2$.

$$a_\text{eq} = a_\text{o} - 1.1 \cdot r_\text{o} \tag{2}$$

$$h_\text{eq} = h_\text{o} - 0.2 \cdot r_\text{o} \tag{3}$$

However, the equivalent lengths and heights are only used when calculating the resistance of the Tees in Vierendeel bending. Similarly, Eurocode cross section classification in Vierendeel bending does not account for the opening corner radius of rectangular openings. The key parameter in determining this section class is the effective length, a_eff, which is set equal to the opening length for any rectangular opening, regardless of the corner radius. Therefore, sudden transitions in cross section classification between rectangular and elongated or circular openings occur nonetheless, resulting in unrealistic variations in design capacity among similar openings. Building upon the proposal put forth by Bjerch and Aksnes [4, p. 75], a linear relationship, shown in Equation 4 is suggested, addressing the sudden changes in cross section classes for rectangular openings, specified in EN 1993-1-13 clause 7.5(4).

$$a_\text{eff} = a_\text{o} - 0.6 \cdot r_\text{o} \tag{4}$$

Furthermore, the impact of the corner radius of rectangular openings on the relative web slenderness is addressed to account for similar variations in calculations of web buckling next to the openings. In this regard, Equation 5 is proposed as an adjustment to the relative web slenderness of rectangular web openings in EN 1993-1-13 Equation (8.20).

$$\overline{\lambda}_\text{w} = \frac{3.5h_\text{o} - 2.2r_\text{o}}{t_\text{w} \cdot \lambda_1} \tag{5}$$

These modifications - both the formulae proposed by Bjerch and Aksnes [4, p. 75], as well as the proposal for the effective opening length and relative web slenderness - are implemented and assessed in Sections 5.4 and 5.6. In the study, the Eurocode design capacities utilizing the formulae are denoted as EC_mod.

5.3 Moment-Shear Ratio at Web Opening

In order to further validate the proposed modifications to EN 1993-1-13 regarding the impact of web opening radii, Bjerch and Aksnes [4] suggested conducting tests on beams with different geometries and with varying moment-shear (M/V) ratios. Therefore, in order to assess the ratio's influence on the study, analyses of various opening positions have been performed on two distinct beam geometries, namely specimens F and G. It should be noted that Vierendeel bending consistently emerged as the critical failure mode, regardless of the chosen opening geometries. Consequently, given the significant height-to-span ratios of the specimens, the investigation of the effect of the

M/V ratio primarily focuses on its influence on the Vierendeel bending capacity of the beams. Additionally, the openings were deliberately positioned away from the beam ends and loads to mitigate any influence from related failure modes on the results.

To evaluate the influence of the moment-shear ratio on the beam capacity, a combination of parameters including the opening radius and cross section class was chosen. The computed capacities are presented in Tables 5.1 and 5.2. The moment-shear ratio ranges from 500-700 mm. The Tees of the two cross sections studied are classified as class 2 and 3 in Vierendeel bending, resulting in elastic and plastic design methods, respectively. The opening corner radius varies across four intervals, ranging from non-rounded to perfectly elongated rectangles. The ratios of these intervals are based on the beam opening heights, h_o, and are displayed in the second column of the tables. The column titled "EC" displays the critical design capacity according to EN 1993-1-13, while the column titled "EC_{mod}" presents the critical design capacity of EN 1993-1-13 incorporating the modifications presented in Section 5.2, to account for the rectangular opening corner radius.

Table 5.1 presents the capacities of a model based on the geometry of specimen F, considering different M/V ratios and radii. The only differences compared to the actual specimen are the position of the opening and the corner radius. Vierendeel bending consistently emerges as the critical failure mode in both the Eurocode calculations and the finite element analyses. Although the numerical model invariably yields higher maximum loads, the ratios between the modified Eurocode calculations and Abaqus results remain consistent across all three moment-shear ratios.

Table 5.1: Eurocode and numerical model ultimate capacities, considering M/V ratio and opening corner radius. The beam geometry and opening size are of specimen F. Tees are in class 2 according to EN 1993-1-13 Clause 7.5.

M/V ratio	**Corner Radius,** $2 \cdot r_o/h_o$	**EC [kN]**	**EC_{mod} [kN]**	**Abaqus [kN]**	**EC/ Abaqus**	**EC_{mod}/ Abaqus**
500 mm	0	123		160	0.77	
	0.3	123	137	177	0.70	0.77
	0.6	123	156	202	0.61	0.77
	1	191		250	0.76	
600 mm	0	122		161	0.76	
	0.3	122	136	178	0.69	0.77
	0.6	122	154	202	0.60	0.76
	1	187		250	0.75	
700 mm	0	120		161	0.75	
	0.3	120	135	178	0.68	0.76
	0.6	120	152	201	0.60	0.75
	1	183		249	0.74	

Vierendeel bending

The findings of Table 5.1 confirm the Eurocode's tendency to exhibit high conservatism for large opening corner radii. Furthermore, for the particular beam configuration of specimen F, the elongated and rectangular openings obtain consistent results, with maximum load ratios varying by only 1 % between the two shapes for all three moment-shear ratios. When the modified formulae are introduced, a similar tendency is observed for all openings, indicating the benefit of the adjustment.

Similarly, Table 5.2 shows the capacities of a model based on the geometry of specimen G, considering different M/V ratios and radii. The long opening length and relatively short opening height result in large Tee outstand depths with significant effective lengths. As a result, the Tees obtain class 3 in Vierendeel bending, necessitating the application of elastic design rules. The last two columns of the table clearly demonstrate that the difference in Tee classification leads to capacities that are less than half as accurate compared to those in Table 5.1. Moreover, according to the Eurocode only one third of the numerically estimated load-carrying capacity is utilized. These findings suggest that the cross section classification limits may be overly strict. However, there are minimal differences observed between the modified and standard design rules compared to the FE model. This could be attributed to the relatively smaller influence of the radius as openings gets longer.

Table 5.2: Eurocode and numerical model ultimate capacities, considering M/V ratio and opening corner radius. The beam geometry and opening size are of specimen G. Tees are in class 3 according to EN 1993-1-13 Clause 7.5.

M/V ratio	**Corner Radius,** $2 \cdot r_o/h_o$	**EC** [kN]	$\mathbf{EC_{mod}}$ [kN]	**Abaqus** [kN]	**EC/ Abaqus**	$\mathbf{EC_{mod}}$**/ Abaqus**
500 mm	0	70.5		220	0.32	
	0.3	70.5	74.3	227	0.31	0.33
	0.6	70.5	78.6	239	0.29	0.33
	1	85.1		258	0.33	
600 mm	0	69.1		218	0.32	
	0.3	69.1	72.8	226	0.31	0.32
	0.6	69.1	76.9	237	0.29	0.32
	1	83.1		255	0.33	
700 mm	0	67.8		217	0.31	
	0.3	67.8	71.0	224	0.30	0.32
	0.6	67.8	74.5	235	0.29	0.32
	1	81.2		252	0.32	

Vierendeel bending

When comparing the capacities presented in the EC and EC_{mod} columns, the impact of the Eurocode modifications proposed in Section 5.2 becomes apparent. The EC capacities remain unchanged for all iterations of the radii, while the EC_{mod} capacities align with the trend observed in the numerical model. Specifically, the EC_{mod} capacities progressively increase as the corners of the openings become more rounded.

The two tables share an important common trend: the M/V ratios chosen for the study have almost no effect on capacities. The increase in bending moment, resulting from shifting the web opening by 100-200 mm (thus increasing the M/V ratio by 20-40 %), consistently influences both the numerical model's and Eurocode's capacities by a mere 1-2 %. Consequently, the influence of the M/V ratio on the beam geometries in this study is considered negligible. Therefore, the M/V ratio will be regarded as an irrelevant parameter going forward.

On a final note, the M/V ratio may have a more significant impact on failure modes other than Vierendeel bending. While it is unlikely for most failure modes, considering that Vierendeel bending is already greatly influenced by bending moments, there is a possibility of it affecting the bending and buckling of the Tees (which is accounted for in EN 1993-1-13 clause 8.3). However, the effect of the M/V ratio will still be disregarded, as the bending moments never reach a magnitude that would cause bending or buckling failure of the Tees.

5.4 Corner Radius of Rectangular Web Openings

To further evaluate the suggested modifications to the Eurocode's design rules regarding rectangular opening corner radius proposed in Section 5.2, various opening shapes were tested using the same four intervals of opening corner radius as in Section 5.3. This study focuses exclusively on the most common opening shapes, namely rectangular, elongated and circular openings. Furthermore, the openings are always positioned symmetrically about the beam's neutral axis and at the midpoint between a beam support and its closest load point.

Table 5.3 presents the ultimate load-carrying capacities of the numerical model and Eurocode, with and without the modifications, for a 200 mm wide web opening in the shorter beam geometry, i.e. the geometry of specimen D, E and G. The opening height varies between 200 mm, 225 mm and 250 mm, resulting in a vertical elongation of the opening. The opening Tees have cross section class 2, 2 and 1 in Vierendeel bending for the three opening heights, respectively.

Table 5.3: Ultimate load-carrying capacities according to EN 1993-1-13 and numerical models, considering opening corner radii on beam geometry D/E/G.

Opening Dimensions	**Corner Radius,** $2 \cdot r_o/h_o$	**EC** [kN]	**EC$_{mod}$** [kN]	**Abaqus** [kN]	**EC/ Abaqus**	**EC$_{mod}$/ Abaqus**
a_o = 200 mm h_o = 200mm	0	229		278	0.83	
	0.3	229	265	302	0.76	0.88
	0.6	229	304	337	0.68	0.90
	1	345		342	1.0	
a_o = 200 mm h_o = 225 mm	0	178		227	0.78	
	0.3	178	210	255	0.70	0.82
	0.6	178	253	296	0.60	0.85
	0.9*	178	298	342	0.52	0.87
a_o = 200 mm h_o = 250 mm	0	126		177	0.71	
	0.3	126	155	209	0.60	0.74
	0.6	126	198	254	0.49	0.78
	0.8*	126	238	292	0.43	0.82

*Maximum radius size reached due to vertical, not horizontal, opening elongation
Vierendeel bending , web buckling next to opening , bending moment at midspan ,
Vierendeel bending/bending moment at midspan .

Recurringly, the modified Eurocode capacities increase synchronously with numerical model capacities, for all corner radius intervals. In contrast, the unaltered Eurocode design capacities remain constant, at a low utilization ratio, until the opening corner radius reaches 100 % and the opening shape is redefined as elongated. The Eurocode design capacities exhibit overall greater precision in Table 5.3 than previously shown in Table 5.2, due to the utilization of plastic design capacity from Tees in class 2 and 1. However, the precision decreases as the opening height is increased, suggesting that the Vierendeel bending design capacity in EN 1993-1-13 may be too conservative for smaller Tee depths. Moreover, despite the expected increase in capacity ratio resulting from improved cross section stability, the Eurocode precision further decreases as the beams' Tees transition to cross section class 1. This discrepancy arises because EN 1993-1-13 does not differentiate between cross section class 1 and 2 in Vierendeel bending, even as the Tee depth continues to decrease.

Interestingly, as the opening corner radius of the smaller openings increases, the bending moment at midspan becomes the critical failure mode in the numerical model. In the case of the squared opening dimensions, both the Eurocode and the model indicate failure due to the bending moment at midspan. Consequently, a utilization ratio of 99 % is achieved. While the numerical model is expected to have at least a 3 % error, this could have been a concerning trend with respect to conservatism. However, for bending at midspan, the deviations in model results have been significantly lower due to the almost nonexistent mesh distortions.

Table 5.4 presents the ultimate load-carrying capacities of the numerical model and Eurocode, with and without modifications, for a 250 mm wide opening in the beam geometry of specimen D, E and G. The opening height varies between 190 mm, 220 mm and 250 mm, in this case ranging from a horizontally elongated to a perfectly squared rectangular opening. The opening Tees have cross section classes 3, 2 and 1 in Vierendeel bending, respectively.

Table 5.4: Ultimate capacities according to EN 1993-1-13 and numerical models, considering opening corner radii using beam geometry D/E/G.

Opening Dimensions	**Corner Radius,** $2 \cdot r_o/h_o$	**EC** [kN]	**EC$_{\text{mod}}$** [kN]	**Abaqus** [kN]	**EC/ Abaqus**	**EC$_{\text{mod}}$/ Abaqus**
$a_o = 250$ mm $h_o = 190$ mm	0	113		253	0.45	
	0.3	113	126	275	0.41	0.46
	0.6	113	142	305	0.37	0.47
	1	171		342	0.50	
$a_o = 250$ mm $h_o = 220$ mm	0	156		198	0.79	
	0.3	156	179	221	0.71	0.81
	0.6	156	208	254	0.61	0.82
	1	261		314	0.83	
$a_o = 250$ mm $h_o = 250$ mm	0	103		144	0.71	
	0.3	103	121	169	0.61	0.71
	0.6	103	148	205	0.50	0.72
	1	204		273	0.75	

Vierendeel bending , bending moment at midspan .

Further substantiating the promising performance of the modifications, the modified Eurocode capacities once again increase in sync with numerical model capacities. However, the difference in ratio of utilization between the first and second opening geometry is particularly noteworthy. Strikingly, according to EN 1993-1-13 design capacities, the beam's strength increases as the opening height is increased from 190 mm to 220 mm. Unambiguously, this phenomenon can be attributed to the transition from Tee class 3 and elastic design capacity, to Tee class 2 and plastic design capacity. Moreover, this finding serves as yet another indication of the significant underestimation of Vierendeel bending capacity by the elastic capacity design rules of EN 1993-1-13, when compared to the numerical model.

Table 5.5 addresses the effect of the opening corner radius on web buckling next to openings as the intended critical failure mode. The table presents ultimate capacities obtained using the proposed modifications to the relative web slenderness in EN 1993-1-13, as outlined in Section 5.2. These capacities are compared to the unchanged Eurocode capacities and the numerical model results. The analysis focuses on two openings with a more slender web configuration, situated on the taller beam, with geometry similar to specimen A, B, and F. This specific configuration was chosen to induce the desired web buckling behavior. It should be noted that, in this case, the opening radius ratios in the second column of the table are based on the opening length, a_o, rather than the opening height, h_o.

Table 5.5: Ultimate capacities according to EN 1993-1-13 and numerical models, considering opening corner radii using beam geometry A/B/F.

Opening Dimensions	***Opening Radius,** $2 \cdot r_o/a_o$	**EC [kN]**	**EC$_{mod}$ [kN]**	**Abaqus [kN]**	**EC/ Abaqus**	**EC$_{mod}$/ Abaqus**
$a_o = 100$ mm $h_o = 290$ mm	0	231		324	0.71	
	0.3	231	246	337	0.69	0.73
	0.6	231	262	359	0.64	0.73
	1	231	287	389	0.59	0.74
$a_o = 125$ mm $h_o = 250$ mm	0	263		374	0.70	
	0.3	263	288	390	0.68	0.74
	0.6	263	316	412	0.64	0.77
	1	263	360	415	0.63	0.87

*Radius ratio based on a_o, not h_o as previously due to vertical elongation
Web buckling next to opening , Bending moment at midspan ,
Web buckling next to opening/bending moment at midspan .

Even in this case, the trend for the modified Eurocode capacities remains consistent with the results obtained from the finite element analyses. As the opening radius increases, the capacities of both EC$_{mod}$ and the FE model increase at a similar rate. Meanwhile, the design capacities of EC remain constant. It should be noted that in this scenario, the capacities of EC and EC$_{mod}$ do not align for fully rounded corners, because the opening radius intervals are based on the opening length. As a result, the openings never reaches the typical horizontally elongated shape that would allow for the use of the same design rules in both methods.

Conclusively, based on the 32 Abaqus simulations and 64 Eurocode calculations conducted, the proposed modifications to EN 1993-1-13 presented in Section 5.2 provide more precise, yet sufficiently conservative results. The adjustments successfully replicate the impact of the corner radius on the load-carrying capacity, as observed in the numerical model, across all five tables presented above. This parametric study included variations in opening shape, Tee classification, opening corner radius, failure mode and M/V ratio (although deemed negligible). Convincingly, the proposed formulae are considered valid for beams with similar characteristics.

Importantly, the study was limited to openings positioned symmetrically about the beam's neutral axis. Although unlikely, it is possible that an opening shifted closer to the beams compressed flange could challenge the conservative nature of the proposed modifications. Furthermore, openings of the study was never positioned close to loading points nor supports. This would have introduced new failure modes, alongside the ones investigated in this study. However, since these failure modes are addressed by specific clauses in EN 1993-1-13, the findings of this study still hold valid. Nevertheless, it is possible that the modifications could be extrapolated to encompass those situations as well.

On a final note, although the modifications to the Eurocode remedies the significant disparity between numerical model capacity and the Eurocode's design capacity, as the opening corner radius increases, they do not rectify the overly conservative nature of the Eurocode in terms of elastic capacity design. Of particular concern, is the Eurocode's tendency to drastically drop in capacity, when the Tee section class transitions from 2 to 3, even when the opening is reduced in size. Consequently, according to the Eurocode, increasing the opening could potentially double the beam's capacity in many cases where the beam falls below the capacity requirements.

5.5 Plastic Design Capacity of Tees in Vierendeel Bending

Observations made in previous studies of beams with web openings at NTNU point to overly conservative EN 1993-1-13 elastic design capacities in Vierendeel bending for Tee outstands in class 3. Hovda and Hurum [3, p. 106], Bjerch and Aksnes [4, pp. 63-72] and Grønland [5, pp. 40-43] all suggested that the Eurocode's design method on this topic should be improved. In a similar fashion, they all identified that the plastic design method is superior to the elastic design method when estimating the ultimate capacity of beams with class 3 Tee outstands. The results of Sections 5.3 and 5.4 further support this finding. When the Tee outstand class is 3 and the elastic design method is utilized, the Eurocode's precision never surpasses 50 %. Even worse, in Table 5.2 (Section 5.3), the design capacities of EN 1993-1-13 only amount to 33 % of the numerical model's ultimate loads.

In this section, the plausibility of exclusively utilizing plastic design capacity in Vierendeel bending is assessed. More than 80 web openings, mostly with Tee outstand class 3, have been tested on the numerical model. Their ultimate capacities and failure modes have been compared to those suggested by both elastic and plastic Eurocode design. The specified comparison of 44 web openings - 16 rectangular, 16 elongated and 12 circular - is presented in Tables 5.6, 5.7 and 5.8, respectively. Simultaneously, the contour plots of the numerical model tests' web opening areas have been examined to evaluate the stress distribution in the Tee outstands. Two contour plots of each opening shape is displayed in Figures 5.6, 5.7 and 5.8. Note that the nonlinear strain hardening model (f_y = 446 MPa) and an M/V ratio of 700 mm are employed on the beam geometry of specimens A, B and F, consistently.

Table 5.6 lists and compares the ultimate capacities of the current design method and imposed plastic design method of the Eurocode to the numerical model results of 16 rectangular web openings. All of the rectangular openings have zero corner radius. Although this results in larger stress concentrations at the opening corners of the numerical model, it does not significantly influence the model's ultimate capacity. The current elastic design method and the suggested plastic design method for Vierendeel bending resistance of the Eurocode are reported in the "EC" and "$EC_{T,pl}$"

columns, respectively. Apart from plastic capacities utilizing ”plastic resistance” in EN 1993-1-13 Clause 8.4(6), the inputs of the elastic and plastic design calculations are identical. Markedly, each estimated or observed failure mode of the listed capacities is indicated with a unique cell coloring. Furthermore, to challenge the conservatism of the plastic capacities, opening lengths exceeding the limiting dimensions of EN 1993-1-13 Table 8.1 - *Limiting dimensions for different shapes of unstiffened openings* are frequently used. These opening lengths are marked with an asterisk (*) in all tables representing the study of the plastic capacity.

Importantly, the numerical model frequently experiences failure from bending moment at midspan. In those cases, its ultimate capacity converges on a constant value of 415 kN, regardless of web opening geometry, rendering a comparison to Eurocode Vierendeel bending capacity worthless. Therefore, the precision ratio between Eurocode and model is only considered when their estimated failure modes are alike.

Table 5.6: Ultimate capacities of elastic and plastic Eurocode calculations compared to numerical model results.

Rectangular Opening Shape

h_o [mm]	**a_o [mm]**	**Tee Outstand Class**	**EC [kN]**	**$EC_{T,pl}$ [kN]**	**Abaqus [kN]**	**EC/ Abaqus [-]**	**$EC_{T,pl}$/ Abaqus [-]**
50	200*	3	263	385	415	0.63	0.93
	300*	3	135	251	414	0.33	0.61
	400*	3	96.0	184	413	0.23	0.45
	500*	3	75.7	145	404	0.19	0.36
100	100	2	385	385	415	0.93	0.93
	200	3	263	385	414	0.63	0.93
	300*	3	135	251	414	0.33	0.61
	400*	3	96.0	184	396	0.24	0.46
150	150	2	385	385	414	0.93	0.93
	250	3	174	311	414	0.42	0.75
	350	3	112	212	346	0.32	0.61
	450*	3	84.5	162	296	0.29	0.55
200	200	3	193	317	390	0.50	0.81
	300	3	134	251	303	0.44	0.83
	400	3	96.0	184	241	0.40	0.76
	500	3	75.7	145	196	0.39	0.74

*Opening lengths exceeding limits of EN 1993-1-13 Table 8.1.
Vierendeel bending , bending moment at midspan , web buckling next to opening ,
Vierendeel bending/bending moment at midspan ,
web buckling next to opening/bending moment at midspan .

In continuation of the observed trend, elastic capacity accuracies of Table 5.6 are dire, never reaching 50 % of the numerical model’s results. Conversely, the plastic Vierendeel capacities consistently double the elastic ones, without ever approaching non-conservative values. A common denominator for both the elastic and plastic capacities is that their precision steadily decreases as the opening length increases. In contrast, accuracies improve as the opening height increases. Notably, in most cases, the Eurocode estimates Vierendeel bending long before the model's capacity is at all impacted by the web opening.

Figure 5.6 shows the maximum and minimum in-plane stress distribution around two of the web openings presented in Table 5.6. The contour plots display the stresses of the web surface facing the reader, specifically the fifth Simpson integration point of the web's shell elements. Elastic design capacity theory allows only the outermost fiber of a cross section's stress distribution to yield before failure. Meanwhile, plastic design capacity theory suggests that an entire cross section can yield prior to collapse. Applying this to the Tees of the analyzed openings, a Tee is categorized with a plastic behavior if its entire cross section reaches yield stress ($f_\text{y} = 446$ MPa) before the model achieves its ultimate load. Conversely, a Tee is classified with an elastic response if its cross section never yields uniformly, prior to model ultimate load.

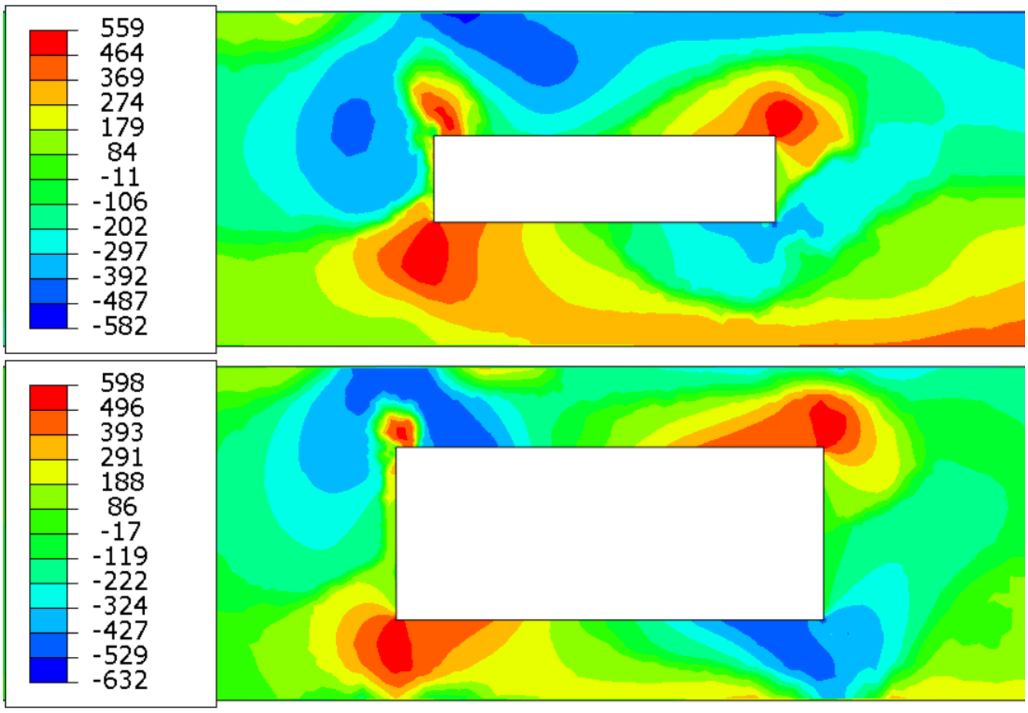

Figure 5.6: Maximum and minimum in-plane principal stress [MPa] distribution prior to ultimate load around rectangular web openings with dimensions $\text{h}_\text{o} = 100$ mm, $\text{a}_\text{o} = 400$ mm and $\text{h}_\text{o} = 200$ mm, $\text{a}_\text{o} = 500$ mm, respectively.

Importantly, the top-left and bottom-right corners of the web openings depicted in Figure 5.6 experience compression from the secondary bending moment, resulting from the shear force in the Tees. Consequently, the corresponding corners of the model start bulging as the load increases. In the displayed figures, the bulges consistently face the reader. Since these Tee outstand areas are prone to geometric instabilities, they are the regions of interest when categorizing Tee behavior. Furthermore, as the beam's bottom flange is subjected to tension from the global bending, the Tee section near the bottom-right opening corner rarely fully yields. Consequently, the top-left Tee area generally plays the defining role in this study.

Both contour plots in Figure 5.6 presents the in-plane stress distribution of the web after the bulging of the compressed opening corners begins, but before the model reaches its ultimate load. In the case of the model with the smaller web opening ($h_\text{o} = 100$ mm, $a_\text{o} = 400$ mm), the Tees never reach full plastic utilization, indicating an elastic response. However, for the increased web opening ($h_o = 200$ mm, $a_o = 500$ mm), specific sections of the Tees yield entirely. As a general note on the plots not presented here, a wider opening tends to lean towards an elastic behavior. Quite consistently, only the web openings that exceed the limits of EN 1993-1-13, exhibit a definite elastic reaction. Moreover, drawing conclusions for the tests with an opening height of 150 mm proved more challenging, as the stress distributions showed a more ambiguous middle ground between elastic and plastic response.

Summarizing the results of the study on plastic capacity of rectangular openings, the proposition of exclusively utilizing plastic design capacity in Vierendeel bending appears less credible, as the longest Tee outstands of the test clearly exhibited an elastic response. However, a significant portion of the shorter Tee outstands approached or even demonstrated a plastic behavior, despite being classified as Tee section class 3.

Table 5.7 compares the ultimate capacities of the Eurocode's current design method and imposed plastic design capacities to numerical model results of 16 elongated web openings. Similar to rectangular openings, the elastic capacities never exceed 50 % of the model's capacities, and the plastic capacities generally double the elastic capacities, yet never reach non-conservative values. Recurringly, Eurocode accuracy decreases as opening length increase, and improves for increasing opening heights.

Table 5.7: Ultimate capacities of elastic and plastic Eurocode calculations compared to numerical models.

Elongated Opening Shape							
h_o [mm]	**a_o [mm]**	**Tee Outstand Class**	**EC [kN]**	**$EC_{T,pl}$ [kN]**	**Abaqus [kN]**	**EC/ Abaqus [-]**	**$EC_{T,pl}$/ Abaqus [-]**
50	200*	3	337	385	415	0.81	0.93
	300*	3	149	275	414	0.36	0.66
	400*	3	102	197	413	0.25	0.48
	500*	3	79.0	153	409	0.19	0.37
100	200	3	385	385	414	0.93	0.93
	300	3	166	302	414	0.40	0.73
	400*	3	111	211	413	0.27	0.51
	500*	3	84.7	163	366	0.23	0.45
150	200	3	361	385	414	0.87	0.93
	300	3	189	333	413	0.46	0.81
	400	3	120	228	375	0.32	0.61
	500*	3	90.0	173	312	0.29	0.55
200	250	3	247	385	414	0.60	0.93
	300	3	200	351	403	0.50	0.87
	400	3	131	247	318	0.41	0.78
	500	3	96.1	184	253	0.38	0.73

*Opening lengths exceeding limits of EN 1993-1-13 Table 8.1.

Vierendeel bending , bending moment at midspan ,

Vierendeel bending/bending moment at midspan .

Figure 5.7 shows the maximum and minimum in-plane stress distribution around two of the web openings presented in Table 5.7. Similar to the rectangular openings, the top-left and bottom-right corners bulge slightly out of the paper plane due to compression from the secondary bending moments of the Tees. However, singular stress concentrations do not appear in this case, as the opening corners are completely rounded.

Recurringly, the longer of the studied Tee outstands exhibit elastic stress distributions, as observed in the first web opening of Figure 5.7. On the other hand, the second web opening of Figure 5.7 demonstrate that the shorter Tee outstands of the elongated openings approach a fully plastic behavior. Although one might assume an elongated opening would display more plastic behavior than a rectangular opening of the same dimensions, this was generally not the case. The elongated web openings of the study did not show any noteworthy distinctions compared to their rectangular counterpart.

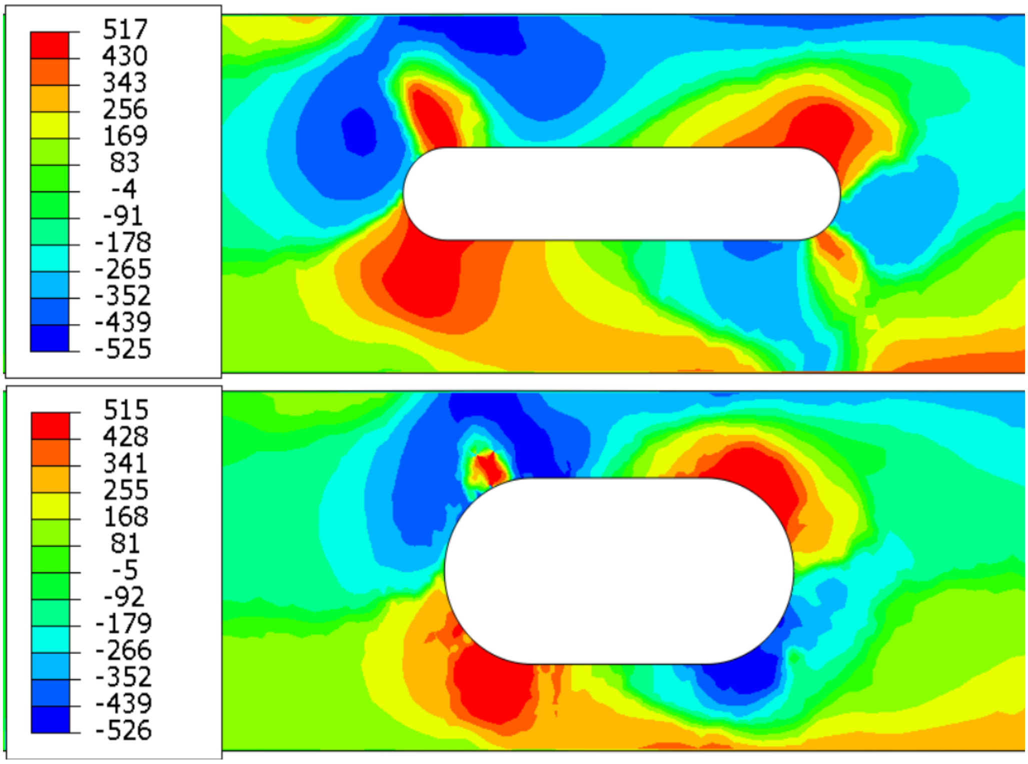

Figure 5.7: Maximum and minimum in-plane principal stress [MPa] distribution prior to ultimate load around elongated web openings with dimensions $\mathrm{h_o} = 100$ mm, $\mathrm{a_o} = 500$ mm and $\mathrm{h_o} = 200$ mm, $\mathrm{a_o} = 400$ mm, respectively.

Finally, Table 5.8 compares the ultimate capacities of the Eurocode's current and imposed plastic design capacity to numerical model results of 12 circular web openings. Initially, results from the general model, with a web thickness of 6 mm, are reported. However, as the higher Vierendeel bending section classes occur for larger effective opening lengths, and circular openings are limited by height, none of the general model circular opening Tees obtain cross section class 3. Consequently, in an attempt to find cases of circular web opening Tees that meet the cross section class 3 criteria in Vierendeel bending, the web thickness, t_w, was incrementally reduced to 5 mm and 4 mm. However, in tests with the most slender web, buckling failure modes started dominating, rendering the results ineffective for this study.

Nevertheless, the tests conducted with a web thickness of 5 mm yielded some results. More specifically, the 200 mm opening gave Tee cross section class 3. However, as commonly seen, the numerical model fails due to the bending moment at midspan, deeming a practical comparison not feasible.

It is worth noting that the Eurocode's plastic design capacities of circular web openings provide a much more accurate estimate of the capacities of the numerical model, compared to the rectangular and elongated openings. Conversely, the Eurocode's design capacity for web buckling next to the opening, obtained for the openings with a web thickness of 4 mm, significantly underestimates model capacities.

Table 5.8: Ultimate capacities of elastic and plastic Eurocode calculations compared to numerical models.

Circular Opening Shape							
t_w [mm]	**h_o, a_o [mm]**	**Tee Outstand Class**	**EC [kN]**	**$EC_{T,pl}$ [kN]**	**Abaqus [kN]**	**EC/ Abaqus [-]**	**$EC_{T,pl}$/ Abaqus [-]**
6	150	2	385	385	415	0.93	0.93
	200	2	385	385	414	0.93	0.93
	250	2	342	342	395	0.87	0.87
	300	1	178	178	271	0.66	0.66
5	150	2	316	316	386	0.82	0.82
	200	3	286	316	385	0.74	0.82
	250	2	298	298	313	0.95	0.95
	300	1	160	160	220	0.73	0.73
4	150	3	245	245	355	0.69	0.69
	200	3	200	200	303	0.66	0.66
	250	3	138	166	229	0.60	0.73
	300	1	141	141	161	0.87	0.87

Vierendeel bending , bending moment at midspan ,
web buckling next to opening , shear buckling at midspan ,
Vierendeel bending/bending moment at midspan ,
Vierendeel bending/web buckling next to opening .

Figure 5.8 illustrates the maximum and minimum in-plane stress distribution around two of the web openings presented in Table 5.8. For circular openings as well, the top-left and bottom-right corners bulge out of the paper plane due to the compression from the secondary bending moments. The Tees of the largest opening displayed in Figure 5.8 are classified as section class 2 in Vierendeel bending. Coherently, tendencies of plastic stress distributions in the Tees can be seen. The subsequent opening displayed, features Tees in section class 3. Although the model here eventually fails due to bending moment at midspan, its upper Tee vaguely exhibits a plastic stress distribution prior to ultimate load.

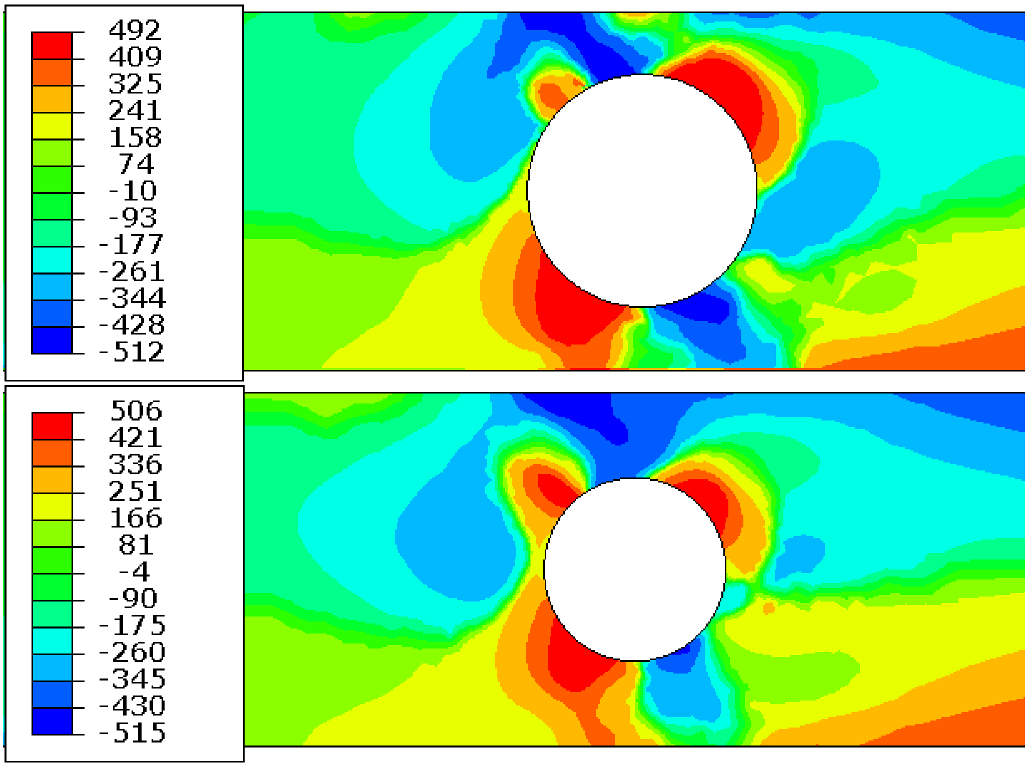

Figure 5.8: Maximum and minimum in-plane principal stress [MPa] distribution prior to ultimate load around circular web openings with dimensions h_o = a_o = 250 mm, t_w = 6 mm and h_o = a_o = 200 mm, t_w = 5 mm, respectively.

In conclusion, the results of the plastic design study refute the hypothesis of exclusively relying on plastic design capacity in Vierendeel bending. This is evident from the observed elastic stress distribution at maximum load in some of the longer Tee outstands, indicating the occurrence of local buckling. However, a greater fraction of the tested web openings with Tees in cross section class 3 showed a plastic response. Among the 44 web openings presented, 14 were in cross section class 3, with elastic Eurocode, plastic Eurocode and numerical model all suggesting Vierendeel bending failure. Out of these 14, only 4 had Tees with definite elastic response, while 10 had Tees showing significant to indisputable plastic behavior. At a minimum, this suggests that the cross section class limits for Vierendeel bending of EN 1993-1-13 is in need of an adjustment.

Markedly, all 4 tests conclusively exhibiting elastic stress distribution, had web openings exceeding the limiting dimensions of EN 1993-1-13 Table 8.1. Ruling them out, one could argue that the hypothesis of exclusively utilizing plastic design capacity in Vierendeel bending holds true, as all valid web opening Tees showed a plastic response. However, without further study of the transition between elastic and plastic response, a solid conclusion cannot be drawn.

Furthermore, in order to validate any conclusion of the plastic design capacity study, more beam geometries should be studied. In particular, accuracy of the Eurocode on beams with significantly larger moment-shear ratios, either through increased beam lengths or imposed artificial bending moments, is an essential but unattended topic of this study. Additionally, more instances of Tees with an elastic stress distribution could likely be achieved by examining beams with even taller webs. All openings presented concerning the plastic design were conducted using the same specimen geometry. Consequently, web opening configurations were limited. Analyses with the beam geometry of specimens D, E and G yielded similar results. However, as the two specimen geometries are relatively identical, both studies are not shown.

Importantly, adjusting the limits for elastic and plastic design in Vierendeel bending of EN 1993-1-13 does little to remedy its design capacity accuracy. In the results of the 14 tests mentioned above, elastic and plastic utilization ratios ranged from 19 % to 50 % and 36 % to 87 %, respectively. Evidently, Eurocode calculations fluctuate considerably, and only a fraction come close to estimating the model's capacity. Moreover, exclusively considering the tested web openings within the limiting dimensions of EN1993-1-13, the elastic and plastic Vierendeel bending design capacities' precision average at mere 41 % and 71 %, respectively.

On a final note, while analyzing contour plots of the plastic design capacity study, a constant change in stress and displacement focal point was observed, as shown in Figure 5.9. Seemingly, for particular web opening geometries, the characteristic corner deformation would occur further in towards to the opening center. The first image of Figure 5.9 displays the out-of-plane displacement of a squared opening. In the subsequent images, the deformation center has clearly shifted to the right. Ultimately, the registered tendency was that the lower and wider an opening is, the more the Vierendeel mechanism would shorten relative to the opening length.

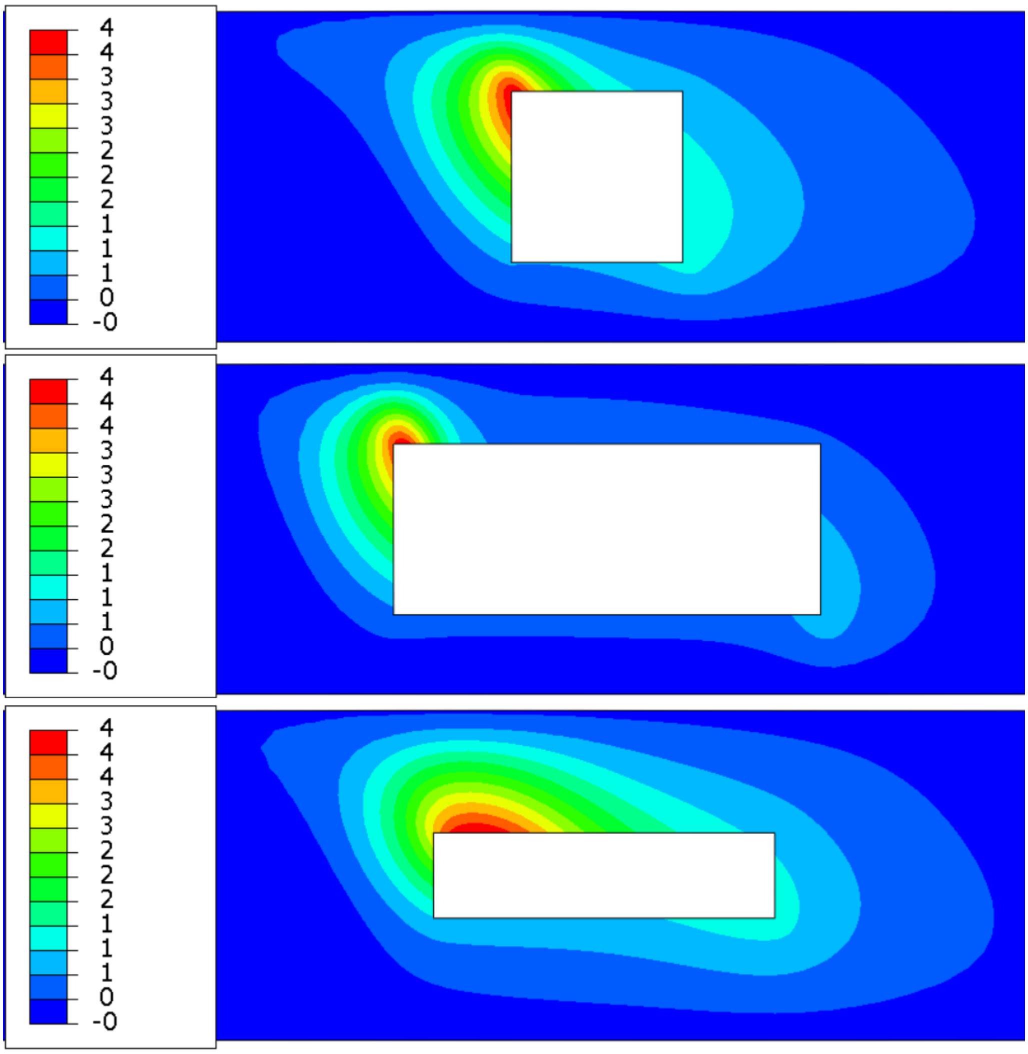

Figure 5.9: Out-of-plane displacement [mm] contour plots of web openings with dimensions h_o = 200 mm, a_o = 200 mm, and h_o = 200 mm, a_o = 500 mm and h_o = 100 mm, a_o = 400 mm, respectively. Displacement focal point changes depending on web opening geometry.

Similarly, lower and wider openings cause lower accuracy of Eurocode Vierendeel bending capacity. Therefore, as a suggestion to further study on this topic, it is recommended to make a general adjustment to the equivalent opening length, a_{eq}, of EN 1993-1-13 Clause 8.4(5) - *Shear resistance to Vierendeel bending*:

$$V_{\mathrm{Vier,Rd}} = (2M_{\mathrm{NV,bT,Rd}} + 2M_{\mathrm{NV,tT,Rd}})/a_{\mathrm{eq}}$$

Redefining the equivalent opening length could prove effective as it controls the theoretical length of the bending mechanism. More specifically, an idea could be to make the equivalent length a function of the compressed Tee's depth, $d_{\mathrm{t,T}}$, the material slenderness parameter, ε, web thickness, t_{w}, and opening width, a_{o}:

$$a_{\mathrm{eq}} = f(d_{\mathrm{t,T}};\ \varepsilon;\ t_{\mathrm{w}};\ a_{\mathrm{o}})\ ,$$

according to model and test observations. Reducing the equivalent width in this manner would address some of the Eurocode's consistent inaccuracies regarding Vierendeel bending capacity.

5.6 Small Web Openings

In a meeting of Subcommittee 3, *WG 20 - EN 1993-1-13 - Beams with Large Web Openings*, held on the 17th of March 2023, Hicks [14] raised questions about the validity of EN 1993-1-13 for smaller web openings. He pointed out that the initial aim of EN 1993-1-13 was to only consider 'large web openings'. However, in EN 1993-1-13 Clause 4.2(5) [1], the Eurocode now states:

> "(5) For widely spaced openings with maximum dimension less than 30 % of section depth and with eccentricity of its centre line not exceeding 10 % of the section depth, the shear verification in 8.2 may be considered as sufficient to satisfy checks in (2) provided that the web slenderness does not exceed 72ϵ. For circular opening, the maximum diameter may be increased to 40 % of the section depth."

As highlighted by Hicks, EN 1993-1-13 never specifically states that it does not cover the design of beams with 'small web openings', which poses the risk that a designer may apply the rules of EN 1993-1-13 even for an insignificant web opening. Consequently, Hicks proposed redefining the aim of EN 1993-1-13 to include consideration of all opening sizes, in some capacity. Furthermore, he proposed adding a definition of a 'small web opening' regardless of the Eurocode's area of application, to clarify for future readers. Finally, he also suggested that Clause 4.2(5) might be improved.

As of today, the Eurocode provides minimal guidance on calculating the capacity of beams with web openings, apart from EN 1993-1-13. In EN 1993-1-1 Clause 6.2.2.1 - *Gross Cross Section* [9], it is stated that "holes for fasteners need not be deducted, but allowance should be made for larger openings". Subsequently, in Clause 6.2.2.2 - *Net Area*, it is recommended to reduce the net area of the cross section by the less appropriate configuration of smaller openings. Therefore, clearly specifying a distinction between small and large web openings could be desirable to avoid unnecessary design calculations, which furthermore is shown to oftentimes yield overly conservative results.

This section aims to test the limits of EN 1993-1-13 Clause 4.2(5) to evaluate when the influence of a small opening on the beam capacity may be neglected. Firstly, to eliminate redundant parameters, the impact of a small web opening's position along the neutral axis of a beam is examined.

Subsequently, critical loads of potential failure modes of beams with varying sizes of circular, elongated and rectangular openings are analyzed, to assess when the different opening shapes can be considered 'small'. Lastly, potential improvements of EN 1993-1-13 Clause 4.2(5) is commented upon.

Figure 5.10 illustrates the design capacities of relevant failure mechanisms for a beam with a circular opening positioned at various locations along its length. The position of the opening center is described by the moment-shear ratio (M/V), where 0 mm indicates that the opening is positioned directly above the support, while 1400 mm is directly beneath the load point. Furthermore, the opening is consistently placed symmetrically about the neutral axis with a diameter, D, set to 30 % of the section's depth, i.e. the beam's height, h. The FE solution for the ultimate capacity of the beam is shown by the green graph, labeled "Abaqus". The remaining curves present the capacity of the different relevant failure modes.

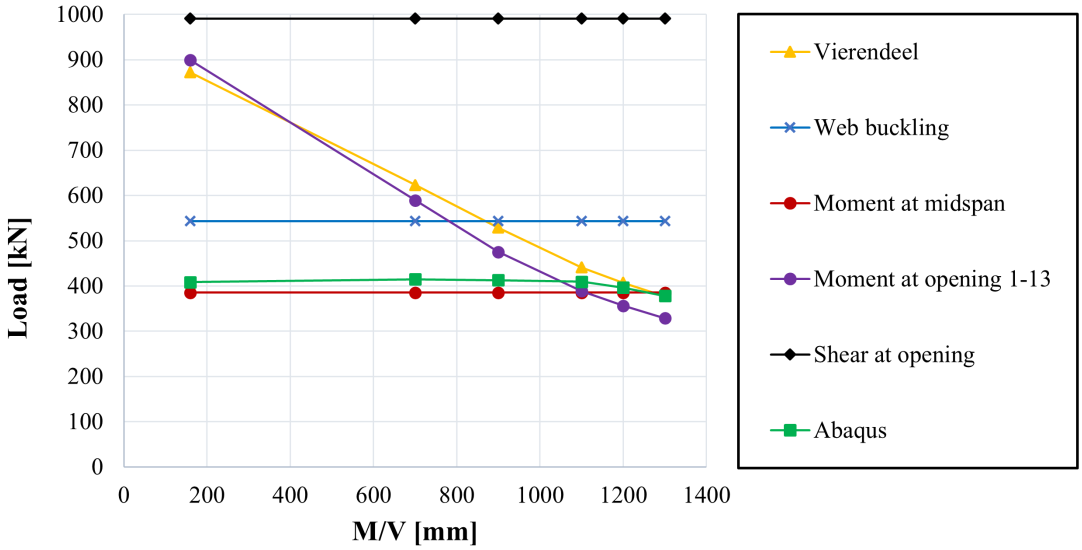

Figure 5.10: Numerical model and Eurocode design capacities for a beam with a circular web opening at various positions along its neutral axis. The web opening dimension is D/h = 0.3 and the beam geometry of specimen A, B and F is used.

Evidently, the beam's capacity is mostly uninfluenced by the relatively small circular opening, as the numerical model's capacity is mainly determined by the bending moment at midspan. However, when the moment-shear ratio exceeds 1100 mm, there is a noticeable decline in the numerical model's capacity. Importantly, the web opening approaches the region covered by EN 1993-1-13 Clause 8.8.2 - *Loads applied over or close to openings*. Consequently, there may be a direct interaction between the load and the opening position, possibly affecting the load distribution across the section. Simultaneously, as the bending moment in the reduced cross section of the opening increases, EN 1993-1-13 Clause 8.3 - *Bending resistance of a beam with web openings* becomes the critical failure mode according to the Eurocode. In the numerical model, a combination of mentioned effects were observed.

Clause 4.2(5) informs the designer that interaction between load and opening should be checked. However, it does not directly control the web opening's position. As the position parameter of the web opening has an impact on beam capacity, it may be advisable to include an additional verification of the web opening's position in Clause 4.2(5). To avoid that the web openings are positioned close to the load point which may impact further results, openings are consistently placed at midpoint between load and support for the rest of this study.

Figures 5.11 and 5.12 present graphs displaying the Eurocode design checks and numerical model capacities of beams with circular web openings of various sizes. The diameter of the web opening incrementally ranges from 0.3 to 0.7 times the height of the beam. The beams' geometries are identical to those of specimens D, E, and G, with the exception of customized web thicknesses, t_w, to manipulate the Tee outstand classes. Clause 4.2(5) states that "the shear verification in 8.2 is sufficient [...] provided that the web slenderness does not exceed 72ε", meaning the limit of the web section class 1 in EN 1993-1-1 Table 5.2. To challenge this limitation, the beam geometry used in Figure 5.12 uses $t_w = 5.2$ mm, resulting in 82ε and web class 2, right on the verge of being class 3. Meanwhile, the beam represented in Figure 5.11 has $t_w = 6$ mm, resulting in 71ε and web class 1 according to the classification.

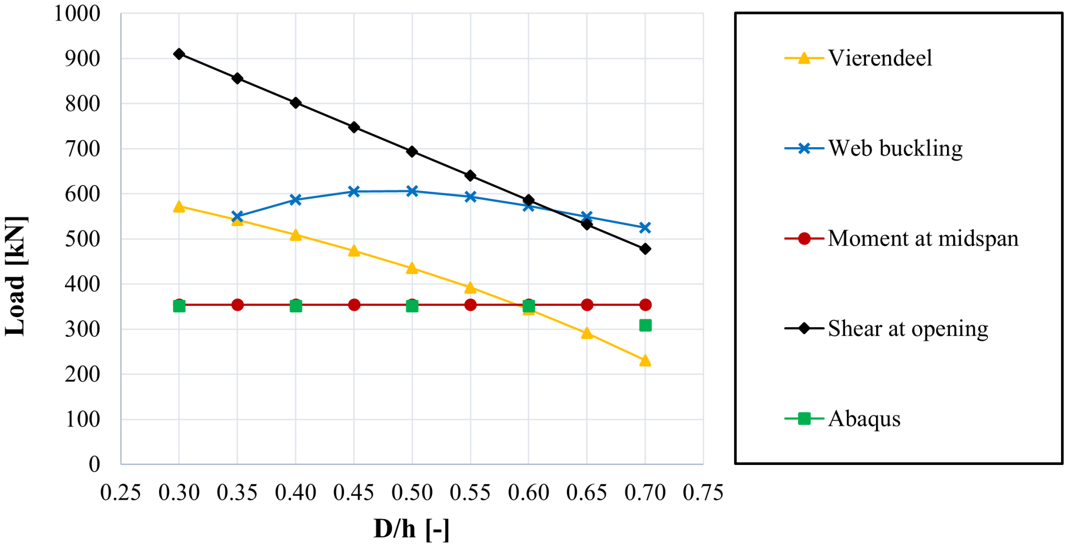

Figure 5.11: Numerical model and Eurocode design capacities of beam with a circular web opening, varying from D/h = 0.30 to D/h = 0.70 in size. Beam geometry of specimen D, E and G with web thickness, $t_w = 6$ mm are used.

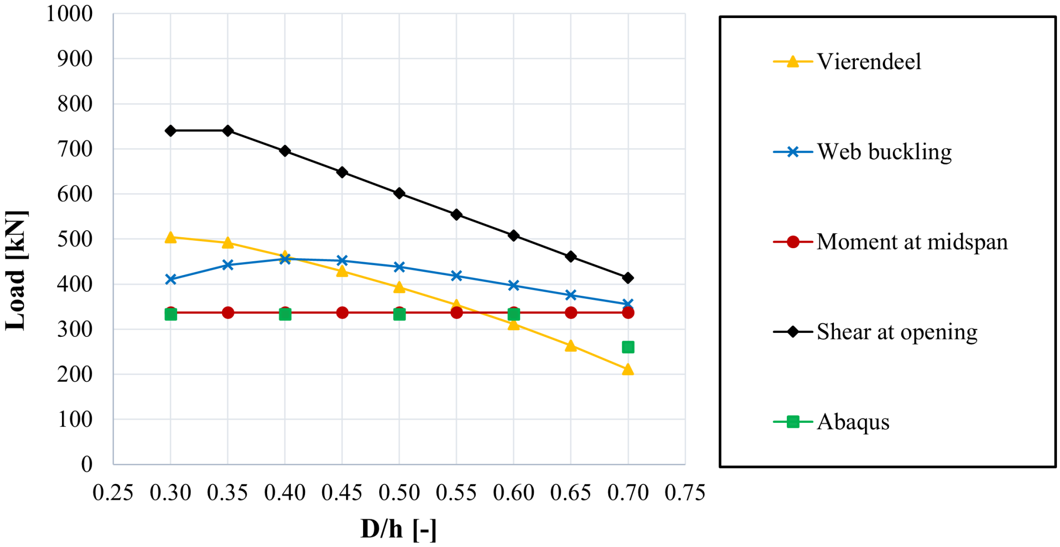

Figure 5.12: Numerical model and Eurocode design capacities of beam with a circular web opening, varying from D/h = 0.30 to D/h = 0.70 in size. Beam geometry of specimen D, E and G with web thickness, $t_w = 5.2$ mm are used.

It should be noted that for the smallest opening size of the class 1 web, web buckling at the opening is omitted according to EN 1993-1-13 Clause 8.5.1(4). Moreover, for efficiency, only certain samples of the opening sizes have been analyzed numerically, indicated with green, squared sample points in the figures.

For both selected web thicknesses, the specific design checks display similar trends. In both web class situations, web openings with D/h < 0.55 results in failure from bending moment at midspan. In these cases, model capacities generally differ from Eurocode moment at midspan capacity by less than 1 %. Unanimously, the stress distribution and displacements in the numerical model verify that moment at midspan is the critical failure in these scenarios. Furthermore, for opening diameters between 60-70 % of the opening height, both models fail as a result of Vierendeel bending, a while after the Eurocode's estimation. For Vierendeel bending and moment at midspan, a more slender web result in a corresponding drop in capacity. The reduction in web thickness has a more significant impact on the shear at opening and web buckling capacities. However, none of these capacities come close to matching either of the modeled capacities for any of the web opening dimensions.

Consequently, based on the study of circular web openings, it appears that the web slenderness limitation of 72ε stated in Clause 4.2(5) is overly conservative. The results indicate that it would be safe to increase the limit to that of cross section class 2, which corresponds to 83ε. Moreover, since the opening does not influence the beam capacity prior to D/h > 0.55, and no Eurocode design check of the opening is more critical than the bending moment at midspan, it seems safe to assume that EN 1993-1-13 clause 4.2(5) is conservative for circular openings. Arguably, the limit for when to neglect circular openings could be even larger than the current 40 % of the section depth.

Figures 5.13 and 5.14 show the results for elongated web openings. Similar to the circular opening study, the two figures display the capacities of beams with $t_w = 6$ mm and $t_w = 5.2$ mm. In the examination of non-circular openings, both opening length, a_o, and height, h_o, must be accounted for. Here, a_o is chosen as the governing parameter, while three different opening heights, up to 40 % of section depth, are presented.

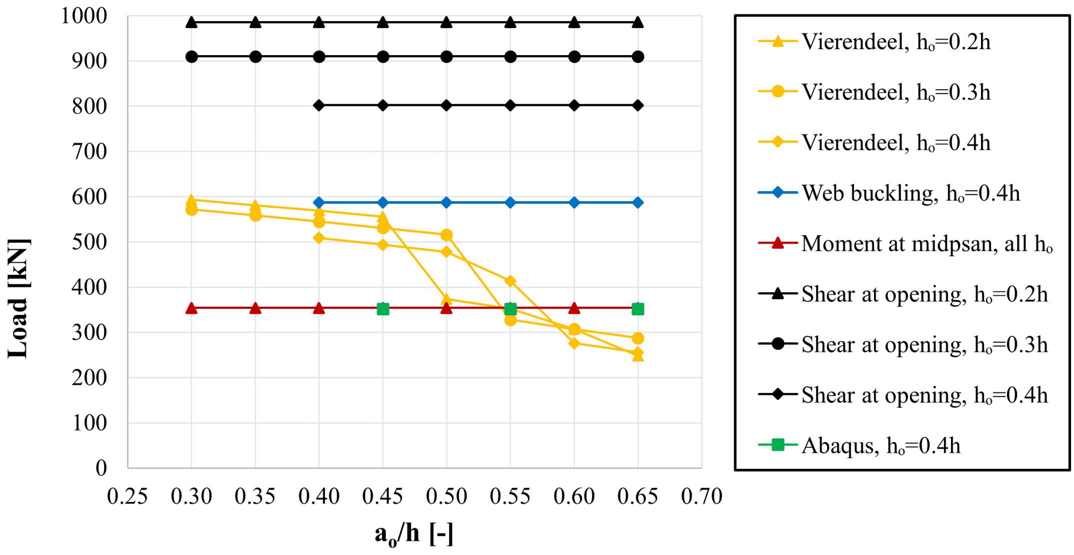

Figure 5.13: Numerical model and Eurocode design capacities of beam with an elongated web opening, varying from a_o/h = 0.30 to a_o/h = 0.65 in size. Beam geometry of specimen D, E and G with web thickness $t_w = 6$ mm are used.

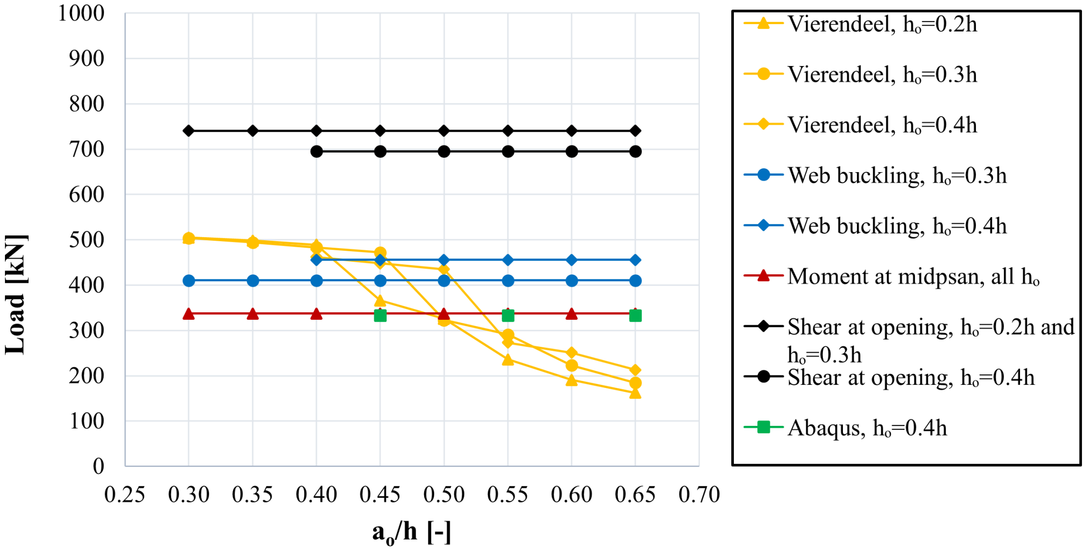

Figure 5.14: Numerical model and Eurocode design capacities of beam with an elongated web opening, varying from $a_o/h = 0.30$ to $a_o/h = 0.65$ in size. Beam geometry of specimen D, E and G with web thickness $t_w = 5.2$ mm are used.

In Figure 5.13, the web buckling capacity is only shown for $h_o = 0.4h$, as it may be omitted for all other selected cases according to EN 1993-1-13 Clause 8.5.1(4). For the more slender web, the web buckling is omitted for the smallest opening height entirely. For clarity, the numerical model's capacities of the largest web opening is shown exclusively, as the smaller openings yielded identical results.

For the study of elongated web openings, the numerical model fails exclusively due to bending moment at midspan. Unlike the circular study, where the numerical model's capacity eventually drop as the opening size increases, the numerical model is completely unaffected for elongated openings up to $a_o/h = 0.65$. While the opening heights are constant for the individual graphs, the shear at opening and web buckling capacities does not change along the x-axis. In contrast, the Vierendeel capacities according to EN 1993-1-13 exhibit visible fluctuations. For openings with $a_o/h > 0.45$, Vierendeel becomes the critical failure mode of the beam according to the Eurocode. Notably, the sudden drop in Vierendeel capacities serves as further evidence of the overly conservative elastic Vierendeel design capacity in EN 1993-1-13, as the Tees suddenly transition to cross section class 3 in Vierendeel bending.

Evidently, Figures 5.13 and 5.14 demonstrate that the current 30 % dimension limit for disregarding the influence of small elongated web openings on beam capacity is sufficiently conservative. Arguably, the limit could be increased, especially if the elastic Vierendeel design capacities of the Eurocode are adjusted. Additionally, as the capacities shown in Figure 5.14, with $t_w = 5.2$ mm and web cross section class 2, fall well within the limits of Clause 4.2(5), it seems safe to append elongated openings with web cross section class 2 to the Clause as well.

Finally, Figures 5.15 and 5.16 present the results for rectangular web openings. Invariably, the first and second figures illustrate the capacities of beams with class 1 and class 2 webs, respectively. For rectangular openings, an additional parameter, the opening corner radius r_o, ranging up to 40 % of the section depth, is considered. It should be noted that the suggested modifications to the Eurocode, regarding the opening corner radius are implemented, as discussed in Section 5.2. Accordingly, the affected design capacities, namely Vierendeel bending and web buckling next to the opening, are separately presented for each radius size tested. Importantly, to restrict the amount of parameters of the rectangular study, a_o and h_o are kept equal, resulting in explicitly squared openings. This will ensure the results to be conservative and applicable for lower opening heights as well. Furthermore, only the results of the numerical model without opening corner radius ($r_\text{o} = 0$) are shown, as they yield the most conservative results.

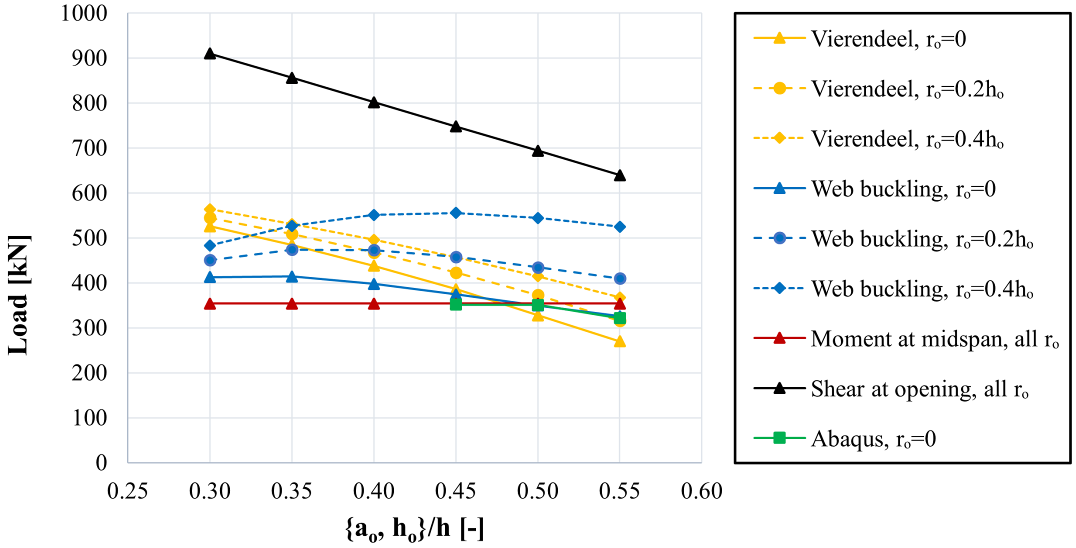

Figure 5.15: Numerical model and Eurocode design capacities of beam with a squared web opening, varying from $a_\text{o} = h_\text{o} = 0.30$ to $a_\text{o} = h_\text{o} = 0.55$ in size. Beam geometry of specimen D, E and G with web thickness, $t_\text{w} = 6$ mm are used.

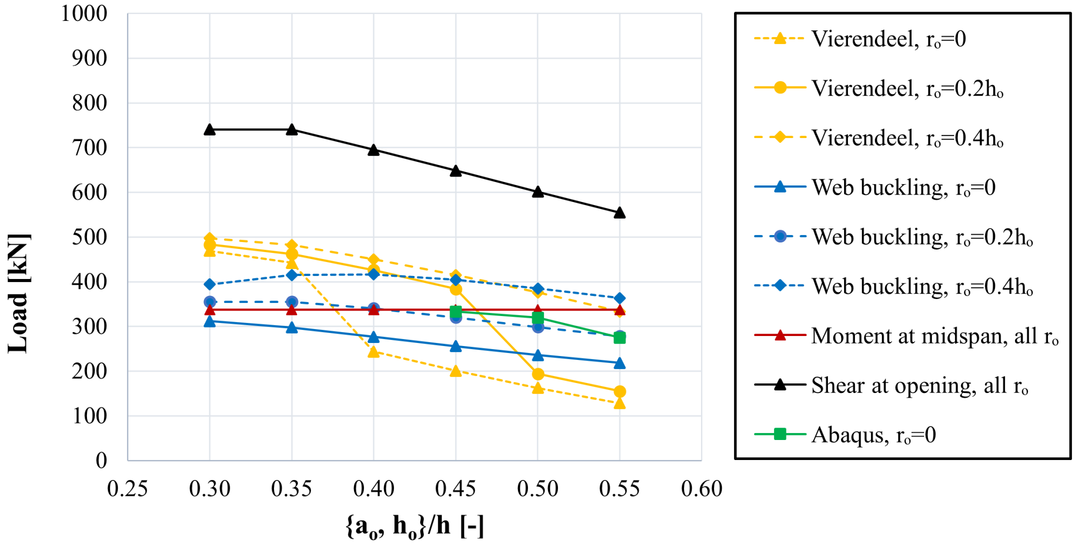

Figure 5.16: Numerical model and Eurocode design capacities of beam with a squared web opening, varying from $a_\text{o} = h_\text{o} = 0.30$ to $a_\text{o}, h_\text{o} = 0.55$ in size. Beam geometry of specimen D, E and G with web thickness, $t_\text{w} = 5.2$ mm are used.

For the study of small rectangular web openings, there are more noticeable differences in the results between the two web cross section classes. Particularly, for the more slender web, EN 1993-1-13 predicts web buckling next to the opening as the failure mode for the for the smallest openings with no corner radius. The numerical model however, fails due to moment at midspan for web openings with $a_\text{o} = h_\text{o} < 0.45h$. Beyond this point, the model's capacity steadily decline as Vierendeel bending becomes the critical failure mode. The Vierendeel bending capacities of the beam with $t_\mathrm{w} = 6$ mm steadily decline as the Tees consistently remain in cross section class 2. As a result, Vierendeel capacity is actually relatively well approximated in this case. For the more slender web however, the Tees enter cross section class 3 and the capacities plummet instantly.

Consistently, considering opening corner radius of the small rectangular web openings results in higher capacities. However, neglecting any influence of the corner radius is arguably the most practical approach when determining whether design checks should be performed, since it would further complicate the reading of Clause 4.2(5) and does not pose significant implications.

The fact that the numerical model never exhibits signs of web buckling for the small rectangular web openings, strongly suggests that the critical web buckling capacities in Figure 5.16 are overly conservative. Based on this presumption, the 72ε web slenderness limit stated in Clause 4.2(5) could be increased to 83ε. Accordingly, the 30 % dimension limit for neglecting small rectangular web openings' influence on beam capacity in EN 1993-1-13 is sufficiently small. However, extending the limit for rectangular openings would require deeming both the web buckling and Vierendeel design capacities of the Eurocode unreasonable. Therefore, such an extension is considered unjustifiable.

In summary of the small web opening study, all analyzed opening geometries support the current limit specified in EN 1993-1-13 Clause 4.2(5) regarding the dimensions at which the influence of web openings on the beam capacity can be disregarded. Additionally, it is suggested that the criterion of web class 1 can be expanded to include web class 2, specifically for circular, elongated, and rectangular opening shapes. Furthermore, the results unanimously demonstrate that the limiting dimensions in Clause 4.2(5) for these opening shapes can be increased. A proposed adjustment to Clause 4.2(5) is outlined below, conservatively summarizing the findings of this study. Suggested modifications to the Clause are highlighted in bold font.

> ”(5) For widely spaced openings with maximum dimension less than 30 % of section depth, and with eccentricity of its centre line not exceeding 10 % of the section depth, the shear verification in 8.2 may be considered as sufficient to satisfy checks in (2) provided that the web slenderness does not exceed **83ϵ**. **For elongated and circular openings the maximum dimension may be increased to 40 % and 50 % of the section depth, respectively.**

6 Conclusions and Suggestions

6.1 Conclusions

Based on a total of seven laboratory experiments on beams with web openings, a general numerical model was calibrated. On average, the model estimated the maximum load of the experiments with an error of ± 3 %. However, maximum loads of specimens F and G were overestimated by 9 %, as a consequence of stiff element behavior in an overly distorted mesh, variations in material input and deformations from former experiments. Accordingly, model precision was assessed at ± 3 %, increased to +9 % for beams with more distorted opening regions.

Utilizing the numerical model, a parameter study was conducted on four main topics, comprising the moment-shear ratio of web openings, the corner radius of rectangular web openings, the plastic design capacity of Tees in Vierendeel bending and small web openings. In total, the results of 128 finite element analyses of various beam and opening geometries have been presented and compared to their respective design capacities of the draft version of EN 1993-1-13 from September 26th, 2022.

Viable M/V ratios to study were limited, as the specimens used, had relatively short spans. Nevertheless, 24 analyses on various opening positions with up to 40 % variation in M/V ratio were conducted. Thereof, a maximum of 2 % change in FE model's ultimate load was observed. Consequently, the M/V ratio parameter was deemed negligible for the subsequent parameter studies. All following web openings were positioned in the middle between the load point and the support.

As the current draft version of EN 1993-1-13 does not account for rectangular web opening corner radii, four formulae addressing the effect of opening corner radius have been presented. Two of these relationships were originally proposed by Bjerch and Aksnes [4, p. 75]. Primarily, the suggested modifications are aimed at segueing the design capacities of Vierendeel bending and web buckling for circular, elongated and rectangular openings. To evaluate these modifications, the results of 56 finite element analyses, involving various opening corner radii, opening dimensions and beam geometries have been compared to their respective EN 1993-1-13 design capacities, both with and without modifications. Unanimously, all studied cases indicated that the suggested formulae drastically, yet conservatively, improves the precision of the design capacity for rounded rectangular web openings.

Subsequently, the plausibility of exclusively utilizing plastic design capacity of the Tees in Vierendeel bending was examined, as inferior precision of elastic design capacities were repeatedly observed. The results of 44 finite element analyses on beams with rectangular, elongated and circular web openings have been compared to their respective elastic and plastic design capacities. The dimensions of the openings in the study were specifically configured to cause Tee cross section class 3, thereby requiring elastic design according to the current draft of EN 1993-1-13. Upon inspection of the stress contour plots of the finite element analyses, it was found that most Tees exhibited a plastic stress distribution. However, as the most slender Tee outstands showed distinct elastic behavior, the initial hypothesis on the study of utilizing the plastic capacity was disproven.

Additionally, a consistent deviation from the numerical model's capacity was observed for both elastic and plastic EN 1993-1-13 Vierendeel bending design, further substantiated by their average precision of 41 % and 71 %, respectively. This deviation was further supported by the examination of the displacements in the opening region using the numerical model, which revealed the potential cause for the inaccuracy. Especially for lower and wider web openings, the Vierendeel bending mechanism appeared to be shortened. Accordingly, a modification to the equivalent opening length of EN 1993-1-13 Clause 8.4(5) has been proposed. The suggested modification aims to reduce the equivalent length of an opening, by a function of Tee outstand slenderness, according to modeled and tested observations.

Lastly, a proposal for an adjustment to EN 1993-1-13 Clause 4.2(5) regarding the definitions of small web openings has been made. The proposal is based on the analysis of 102 opening configurations, which revealed that the limits for small circular and elongated openings can be expanded. Furthermore, the results unanimously indicate that expanding the definition in Clause 4.2(5), to include web cross section class 2, is a conservative approach.

6.2 Suggestions for Further Study

Since this parametric study was limited on several topics, the following suggestions are made to complement the research. The suggestions include considering web opening eccentricity for the analyzed cases, especially considering the complete definition of small web openings, as well as exploring the plastic development of the Tees further. The study would also benefit from different load scenarios, where application of external axial force and loads close to or at the opening are suggested options.

Though less commonly used in practice, expanding this study to include sinusoidal and hexagonal web openings may provide additional insights and complete the study. Furthermore, extending the parameter study to different beam geometries, where larger variations in the moment-shear ratio are possible, would help validate the results on a broader scale.

Bibliography

[1] EN 1993-1-13, Eurocode 3 - Design of steel structures - Part 1-13: Rules for beams with large web openings, draft of Sep. 26 2022, Brussel: European Standardisation Organisation Technical Committee 250 ”Structural Eurocodes”, 2022.

[2] E. A. Marthinussen and H. H. Sandnes, ‘Bjelker med rektangulære åpninger i steget’, M.S. thesis, Department of Structural Engineering, NTNU, Trondheim, 2021.

[3] M. L. Hovda and V. M. Hurum, ‘Bjelker med sirkulære åpninger i steget’, M.S. thesis, Department of Structural Engineering, NTNU, Trondheim, 2021.

[4] G. W. Bjerch and P. A. Aksnes, ‘Bjelker med åpninger i steget’, M.S. thesis, Department of Structural Engineering, NTNU, Trondheim, 2021.

[5] N. A. C. Grønland, ‘Steel beams with unstiffened web openings’, M.S. thesis, Department of Structural Engineering, NTNU, Trondheim, 2021.

[6] N. C. Hagen, ‘On the shear capacity of steel plate girders with large web openings’, Ph.D. dissertation, Department of Structural Engineering, NTNU, Trondheim, 2005.

[7] R. M. Lawson and S. J. Hicks, ‘Design of composite beams with large web openings’, *The Steel Construction Institute*, no. SCI P355, 2011.

[8] F. P. V. Ferreira, C. H. Martins and S. D. Nardin, ‘Advances in composite beams with web openings and composite cellular beams’, *Journal of Constructional Steel Research*, vol. 172, no. 106182, 2020.

[9] EN 1993-1-1, Eurocode 3 - Design of steel structures - part 1-1 - General rules and rules for buildings, Brussel: European Standardisation Organisation Technical Committee 250 ”Structural Eurocodes”, 2005.

[10] A. Masumi, ‘Stålbjelker med åpninger i steget’, M.S. thesis, Department of Structural Engineering, NTNU, Trondheim, 2021.

[11] EN 1993-1-14, Eurocode 3 - Design of steel structures - part 1-14 - Design assisted by finite element analysis, draft of Sep. 19 2022, Brussel: European Standardisation Organisation Technical Committee 250 ”Structural Eurocodes”, 2022.

[12] Simulia. Abaqus online documentation: Version 6.6-1, (Apr. 26 2022), [Online]. Available: https://classes.engineering.wustl.edu/2009/spring/mase5513/abaqus/docs/v6.6/books/usb/default.htm?startat=pt06ch23s06alm15.html.

[13] Execution of steel structures and aluminium structures Part 2: Technical requirements for steel structures, Secretariat: Standard Norge, 2008, European Standardisation Organisation Technical Committee 135 ”Structural Eurocodes.

[14] S. Hicks, ‘Wg20 report: Steel beams with large web openings’, European Standardisation Organisation Technical Committee 250 ”Structural Eurocodes” Sub Committee 3 ’Eurocode 3 - Design of steel structures’, 2023.

Appendix

A Numerical Model Eigenmodes of Specimen F

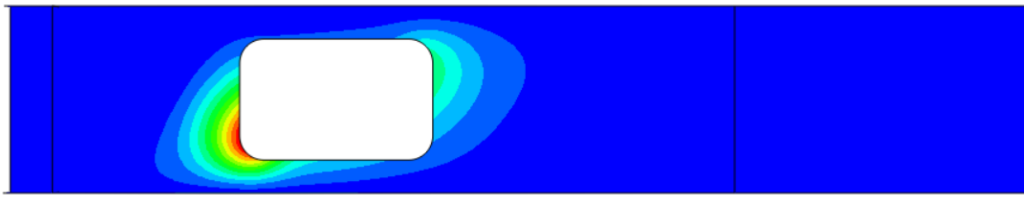

(a) λ_1 = -406 kN

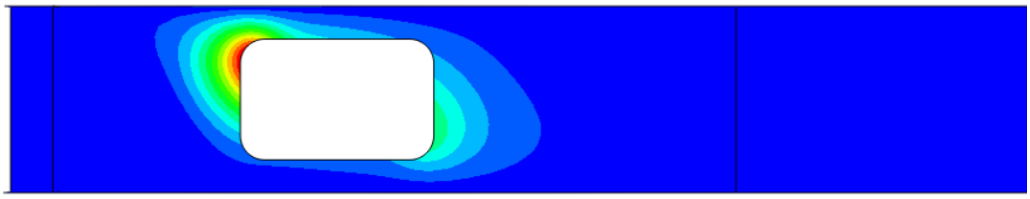

(b) λ_2 = +408 kN

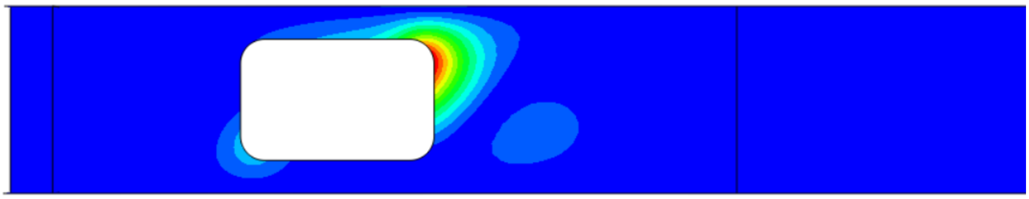

(c) λ_3 = -432 kN

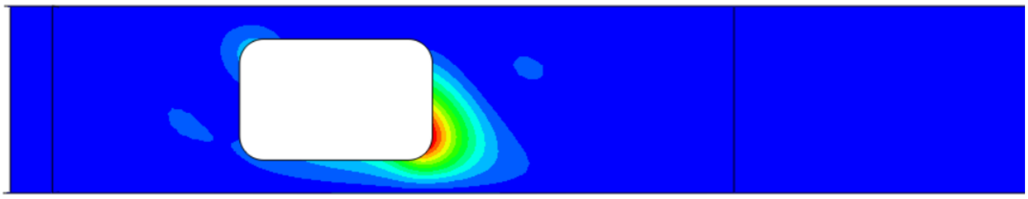

(d) λ_4 = +435 kN

Figure A.1: The first four eigenvalues and corresponding eigenmodes of specimen F.

B Numerical Model Eigenmodes of Specimen G

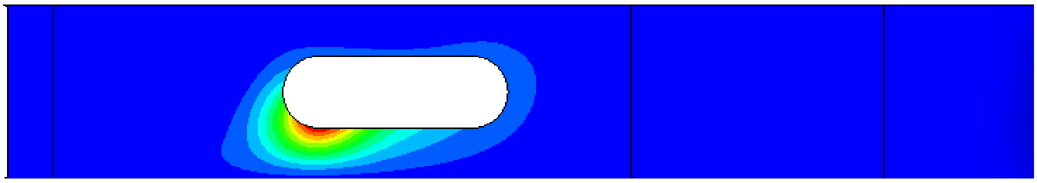

(a) λ_1 = -160 kN

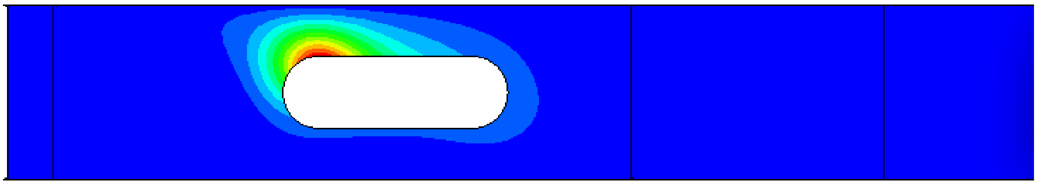

(b) λ_2 = +160 kN

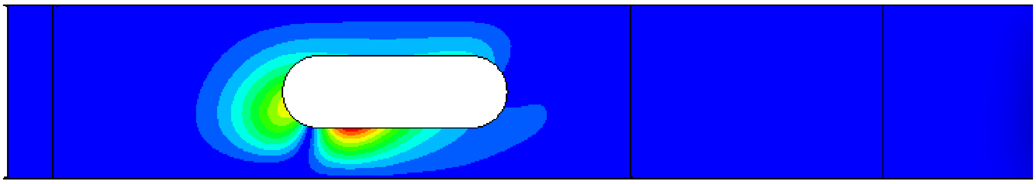

(c) λ_3 = -204 kN

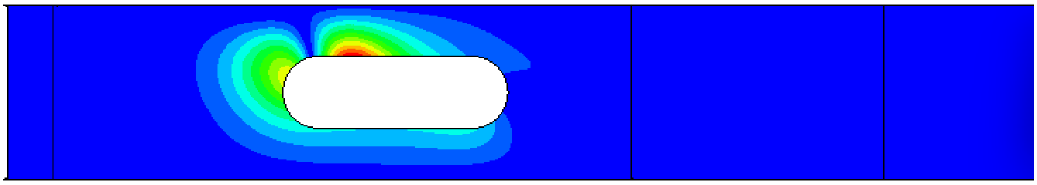

(d) λ_4 = +204 kN

Figure B.1: The first four eigenvalues and corresponding eigenmodes of specimen G. Note that eigenvalues are halved compared to eigenvalues of specimen F, as they are distributed between the two loads of specimen G.

C Response Curves of Various Failure Modes - Examples

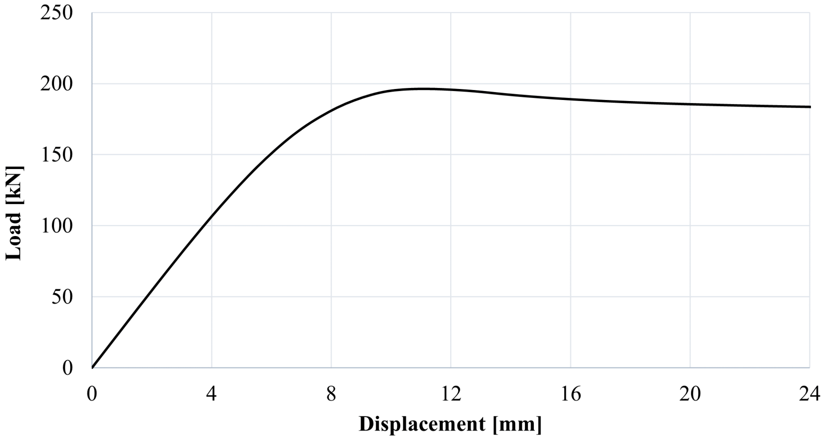

Figure C.1: Response curve with **Vierendeel bending** as critical failure mode. Beam geometry similar to specimen A, B and F. h_o = 200 mm, a_o = 500 mm, r_o = 0 mm, M/V = 700 mm.

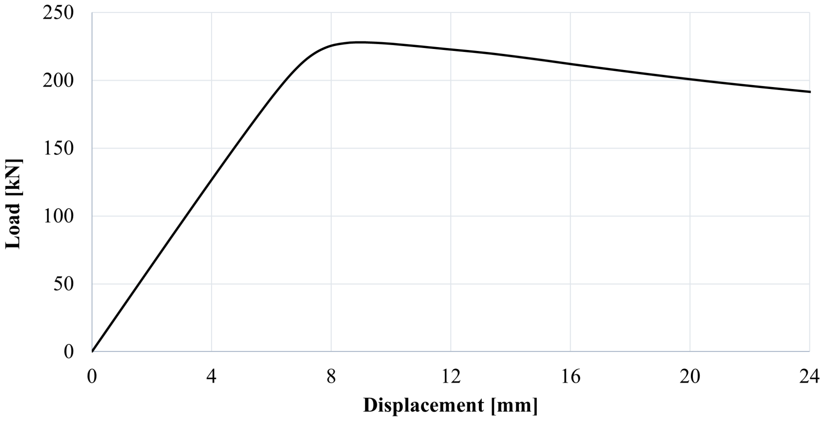

Figure C.2: Response curve with **web buckling next to the opening** as critical failure mode. Beam geometry similar to specimen A, B and F. h_o = 200 mm, a_o = 500 mm, r_o = 0 mm. t_w = 4 mm, M/V = 700 mm.

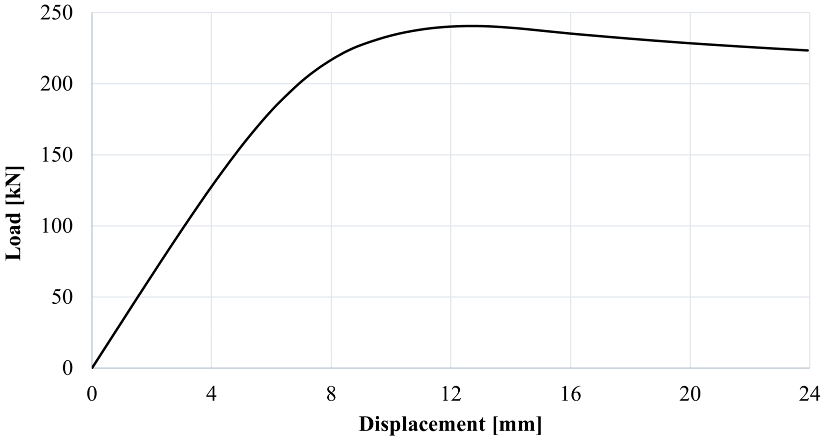

Figure C.3: Response curve with a combination of **Vierendeel bending** and **web buckling next to the opening** as critical failure modes. Beam geometry similar to specimen A, B and F. h_o = 250 mm, a_o = 250 mm, r_o = 0 mm, M/V = 700 mm.

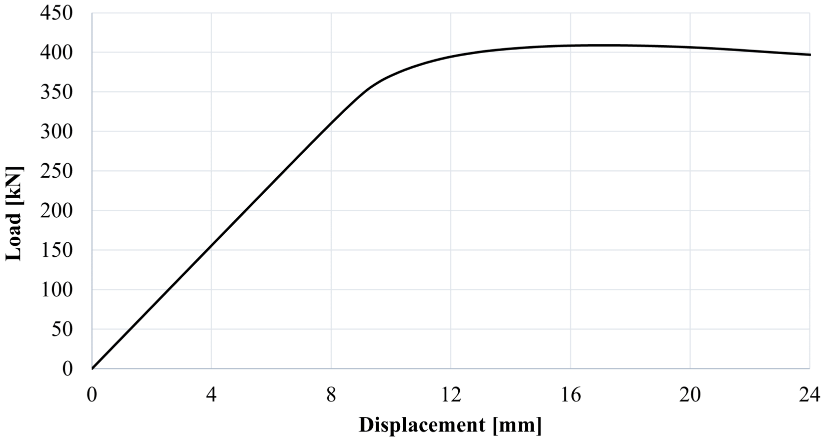

Figure C.4: Response curve with **bending moment at midspan** as critical failure mode. Beam geometry similar to specimen A, B and F. No web opening.

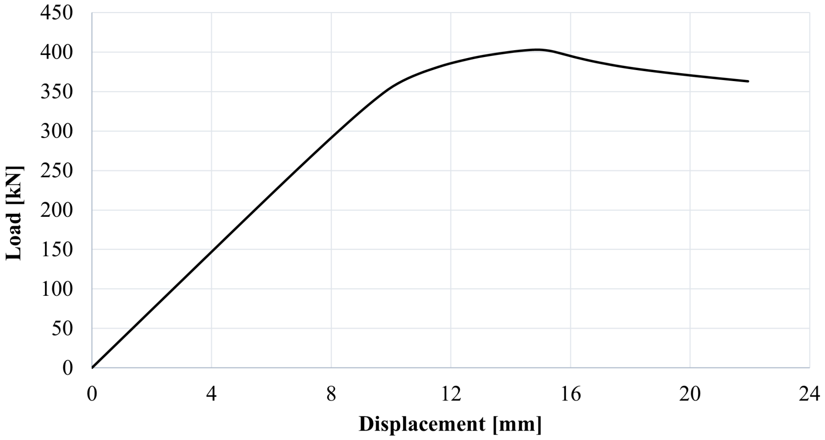

Figure C.5: Response curve with a combination of **Vierendeel bending** and **bending moment at midspan** as critical failure modes. Beam geometry similar to specimen A, B and F. h_{o} = 200 mm, a_{o} = 300 mm, r_{o} = 100 mm, M/V = 700 mm.

D Design Capacity of Specimen F According to the Eurocode

Geometry:

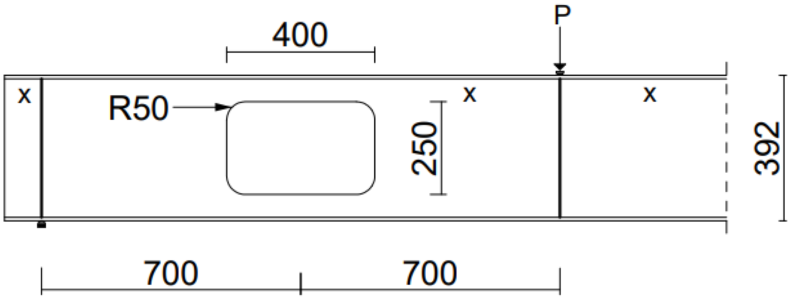

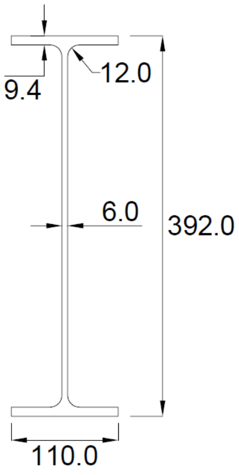

Additional Dimensions:

L	$:= 2800\ \text{mm}$	Beam span
x_o	$:= 700\ \text{mm}$	Distance from support to center of opening
s_e	$:= 500\ \text{mm}$	Distance to support from closest opening edge
s_i	$:= 500\ \text{mm}$	Distance to load from closest opening edge
A	$:= 4307\ \text{mm}^2$	Cross section area
d_T	$:= 49.6\ \text{mm}$	Tee depth

Material Data:

f_y	$:= 446\,\text{MPa}$ (Assumed consistent for entire cross section)	Yield strength
E	$:= 210\,\text{GPa}$	Young's modulus
ν	$:= 0.3$	Poisson ratio
ε	$:= \sqrt{\dfrac{235}{f_\text{y}}} = 0.726$	Material slenderness factor
η	$:= 1.2$	
γ_M0	$= \gamma_\text{M1} := 1$	Partial safety factors

Loads & Reaction Forces:

P_Ed	$:= \underline{120\,\text{kN}}$	Design load
N_Ed	$:= 0$	Design axial force
V_Ed	$:= 60.0\ \text{kN}$	Design shear force
M_Ed	$:= 84.0\ \text{kNm}$	Design bending moment
$M_\text{o,Ed}$	$:= V_\text{Ed} \cdot x_\text{o} = 42.0\ \text{kNm}$	Design bending moment at opening

EN 1993-1-1: Table 5.2 Cross Section Classification

Web: $72 < \frac{c}{t} \cdot \frac{1}{\varepsilon} = 80.2 \leq 83 \Rightarrow$ **Class 2**

Flanges: $\frac{c}{t} \cdot \frac{1}{\varepsilon} = 7.62 \leq 9 \Rightarrow$ **Class 1**

Tee outstand: $10 < \frac{c}{t} \cdot \frac{1}{\varepsilon} = 11.4 \leq 14 \Rightarrow$ **Class 3**

EN 1993-1-13: 7.4 Tee Cross Section Classification for Global Bending

7.4(2) Flange class 1 & Tee class 3

$\Longrightarrow$ **Tee class 2** for global bending

$\Longrightarrow$ $d_{\mathrm{T,mod,b}} = \min(10t_{\mathrm{w}}\varepsilon,\ d_{\mathrm{T}}) = 43.55$ mm — Modified Tee depth for global bending

EN 1993-1-13: 7.5 Tee Cross Section Classification for Vierendeel Bending

7.5(4) $a_{\mathrm{eff}} = a_{\mathrm{o}} = 400$ mm — Effective opening length

7.5(5) $a_{\mathrm{eff}} > 32t_{\mathrm{w}}\varepsilon = 139.4\,\mathrm{mm}$ — Class 2 limit for a_{eff}

$$d_{\mathrm{T,limit,2}} = 10t_{\mathrm{w}}\varepsilon \bigg/ \sqrt{1 - \left(\frac{32t_{\mathrm{w}}\varepsilon}{a_{\mathrm{eff}}}\right)^2} = 46.46 \text{ mm}$$

Class 2 limit of d_{T}

$d_{\mathrm{T}} = 49.6\,\mathrm{mm} > d_{\mathrm{T,limit}} = 46.46\,\mathrm{mm}$

$\Longrightarrow$ Cannot reduce Tee class

7.5(8)
$$d_{\mathrm{T,limit,3}} = 14t_{\mathrm{w}}\varepsilon \bigg/ \sqrt{1 - \left(\frac{36t_{\mathrm{w}}\varepsilon}{a_{\mathrm{eff}}}\right)^2} = 66.28 \text{ mm}$$

Class 3 limit of d_{T}

$d_{\mathrm{T}} = 49.6\,\mathrm{mm} < d_{\mathrm{T,limit}} = 66.28\,\mathrm{mm}$

7.5(7) 7.5(8) fulfilled for Tee class 3

$\Longrightarrow$ May reduce Tee class to 2 and use reduced d_{T}

$\Longrightarrow$ **Tee class 2** for Vierendeel bending

$\Longrightarrow$ $d_{\mathrm{T,mod,V}} = \min\left(d_{\mathrm{T,limit,2}};\ d_{\mathrm{T}}\right) = \underline{46.46\ \mathrm{mm}}$ — Modified Tee depth for Vierendeel bending

EN 1993-1-1: 6.2.6 ULS Shear

6.2.6(3) $A_{\mathrm{V}} = \max(A - 2bt_{\mathrm{f}} + (t_{\mathrm{w}} - 2r)t_{\mathrm{f}};\ \eta h_{\mathrm{w}} t_{\mathrm{w}})$ — Shear area

$= 2687\ \mathrm{mm}^2$

(6.18) $V_{\mathrm{pl,Rd}} = \dfrac{A_{\mathrm{V}}(f_{\mathrm{y}}/\sqrt{3})}{\gamma_{\mathrm{M0}}} = 691.9$ kN — Plastic shear capacity

(6.17)	$\frac{V_{\text{Ed}}}{V_{\text{pl,Rd}}}$	$= 0.09 \leq 1.0 \Rightarrow$ **OK**	Shear capacity verification
6.2.10(3)	$\frac{V_{\text{Ed}}}{V_{\text{pl,Rd}}}$	$= 0.09 \leq 0.5 \Rightarrow$ **OK**	Shear force yield strength reduction check
(6.22)	$\frac{h_w}{t_w} \cdot \frac{\eta}{\varepsilon}$	$= 102.8 > 72 \Rightarrow$ **NOT OK**	Web shear buckling control

$\Longrightarrow$ Have to check for shear buckling according to EN 1993-1-5: 5 Resistance to shear

EN 1993-1-5: 5 Resistance to Shear

A.3(1)	a	$= L/2 = 1400\,\text{mm} \geq h_\text{w} = 373.2$ mm	Distance between transverse stiffeners
	$k_{\tau sl}$	$= 0$ (No longitudinal stiffeners)	Longitudinal stiffener shear buckling coefficient
(A.5)	k_τ	$= 5.34 + 4.00\left(\frac{h_\text{w}}{a}\right)^2 + k_{\tau,sl} = 5.62$	Web slenderness parameter
(5.6)	$\overline{\lambda}_\text{w}$	$= \frac{h_\text{w}}{37.4 t\varepsilon\sqrt{k_\tau}} = 0.9661$	Shear buckling coefficient
Table 5.1	$\frac{0.83}{\eta}$	$\leq \overline{\lambda}_\text{w} = 0.9661 < 1.08$	
	χ_w	$= \frac{0.83}{\overline{\lambda}_w} = 0.8591$	Web buckling factor
(5.2)	$V_{\text{bw,Rd}}$	$= \frac{\chi_\text{w} f_\text{y} h_\text{w} t}{\sqrt{3}\gamma_{\text{M1}}} = 495.4$ kN	Web contribution to shear resistance
5.4(1)	b_f	$= \min(b;\ t_\text{w} + 2 \cdot 15\varepsilon t_\text{f}) = 110$ mm	Flange width contribution limit
	c	$= a\left(0.25 + 1.6\frac{b_\text{f}\,t_\text{f}^2}{t_\text{w}\,h_\text{w}^2}\right) = 376.1$ mm	Transverse stiffener contribution coefficient
	$M_{\text{f,pl,Rd}}$	$= \frac{M_{\text{f,k}}}{\gamma_{\text{M0}}} = 176.4$ kNm	Axial force reduction factor
(5.9)	N_{Ed}	$= 0 \Rightarrow 1$ (No reduction)	Axial force reduction factor
(5.8)	$V_{\text{bf,Rd}}$	$= \frac{b_\text{f} t_\text{f}^2 f_\text{y}}{c\gamma_{\text{M1}}}\left(1 - \left(\frac{M_{\text{Ed}}}{M_{\text{f,Rd}}}\right)\right)^2 = 8.92$ kN	Flanges contribution to shear resistance
(5.1)	$V_{\text{b,Rd}}$	$= \min\left(V_{\text{bw,Rd}} + V_{\text{bf,Rd}};\ \frac{\eta f_\text{y} h_\text{w} t}{\sqrt{3}\gamma_{\text{M1}}}\right) = 504.3$ kN	Cross section shear resistance
(5.10)	η_3	$= \frac{V_{\text{Ed}}}{V_{\text{b,Rd}}} = 0.06 \leq 1.0 \Rightarrow$ **OK**	Shear force verification

EN 1993-1-1: 6.2.4 ULS Compression

(6.10)	$N_{\mathrm{c,Rd}} = \dfrac{Af_{\mathrm{y}}}{\gamma_{M0}} = 1921\ \mathrm{kN}$	Cross section centric compression capacity
(6.9)	$\dfrac{N_{\mathrm{Ed}}}{N_{\mathrm{c,Rd}}} = 0 \leq 1.0 \Rightarrow \textbf{OK}$	Axial force verification

EN 1993-1-1: 6.2.5 ULS Bending Moment

	$W_{\mathrm{y,pl}} = 2\left(bt_{\mathrm{f}}\dfrac{h-t_{\mathrm{f}}}{2} + \dfrac{t_{\mathrm{w}}\,h_{\mathrm{w}}^2}{8}\right) = 604.5 \cdot 10^3\ \mathrm{mm}^3$	Cross section major axis plastic modulus
(6.13)	$M_{\mathrm{c,Rd}} = M_{\mathrm{pl,Rd}} = \dfrac{W_{\mathrm{y,pl}}f_{\mathrm{y}}}{\gamma_{\mathrm{M0}}} = 269.6\ \mathrm{kNm}$	Cross section major axis bending moment capacity
(6.12)	$\dfrac{M_{\mathrm{Ed}}}{M_{\mathrm{c,Rd}}} = 0.31 \leq 1.0 \Rightarrow \textbf{OK}$	Bending moment at midspan verification

EN 1993-1-1: 6.2.1 ULS General

(6.2)	$\dfrac{N_{\mathrm{Ed}}}{N_{\mathrm{Rd}}} + \dfrac{M_{\mathrm{y,Ed}}}{M_{\mathrm{y,Rd}}} = 0 + 0.31 = 0.31 \leq 1.0 \Rightarrow \textbf{OK}$	Conservative linear combination of reaction forces

EN 1993-1-13: Limiting Dimensions for Unstiffened Openings

Table 8.1	$h_{\mathrm{o}} = 250\,\mathrm{mm} \leq 0.75h = 294\,\mathrm{mm} \Rightarrow \textbf{OK}$	Maximum opening height
	$a_{\mathrm{o}} = 400\,\mathrm{mm} \leq 2.5h_o = 625\,\mathrm{mm} \Rightarrow \textbf{OK}$	Maximum opening length
	$s_{\mathrm{e}} = \text{Not available}$	Minimum edge to edge spacing
	$d_{\mathrm{t,T}} = 49.6\,\mathrm{mm} \geq max\left(\dfrac{a_{\mathrm{o}}}{12};\ 0.1h\right) = 39.2\,\mathrm{mm} \Rightarrow \textbf{OK}$	Minimum depth of Tee in compression
	$d_{\mathrm{b,T}} = 49.6\,\mathrm{mm} \geq 0.1h = 39.2\,\mathrm{mm} \Rightarrow \textbf{OK}$	Minimum depth of Tee in tension

EN 1993-1-13: 8.2 Shear Resistance at Web Opening Positions

(8.3)	$V_{\mathrm{o,pl,Rd}} = \min\left(V_{\mathrm{pl,Rd}} - \dfrac{h_{\mathrm{o}}t_{\mathrm{w}}f_{\mathrm{y}}}{\sqrt{3}\gamma_{\mathrm{M0}}};\ V_{\mathrm{w,b,Rd}}\right) = 305.7\,\mathrm{kN}$	Shear resistance at web opening
(8.1)	$\dfrac{V_{\mathrm{Ed}}}{V_{\mathrm{o,pl,Rd}}} = 0.20 \leq 1.0 \Rightarrow \textbf{OK}$	Opening shear force verification
8.2(2)	$\dfrac{V_{\mathrm{Ed}}}{V_{\mathrm{o,pl,Rd}}} = 0.20 \leq 0.5 \Rightarrow \textbf{OK}$	Opening shear force yield strength reduction check

8.5.1(3)	$\frac{h_\mathrm{w}}{t_\mathrm{w}} \cdot \frac{\eta}{\varepsilon} = 102.8 > 72 \Rightarrow$ **NOT OK**	Web shear buckling control
8.5.1(4)	$h_\mathrm{o} = 250\,\mathrm{mm} > 15 t_\mathrm{w}\varepsilon = 65.33\,\mathrm{mm} \Rightarrow$ **NOT OK**	Web shear buckling omittance check
$\Longrightarrow$	Have to check for shear buckling of web next to opening according to EN 1993-1-13: 8.5.2	
8.8.1(4)	$s_\mathrm{e} = 500\,\mathrm{mm} > a_\mathrm{eff} = 400\,\mathrm{mm} \Rightarrow$ **OK**	End-post shear buckling omittance check
$\Longrightarrow$	Do not have to check for shear buckling of end-post web according to EN 1993-1-13: 8.8.1	
8.8.2(2)	$s_\mathrm{i} = 500\,\mathrm{mm} > \min(0.5a_\mathrm{eff};\ h_\mathrm{o}) = 200\,\mathrm{mm} \Rightarrow$ **OK**	Load close to opening check
$\Longrightarrow$	Do not have to check for loads over or close to openings according to EN 1993-1-13: 8.8.2	

EN 1993-1-13: 8.5.2 Web Buckling

8.5.2(3)	$b_\mathrm{w} = 0.5h_\mathrm{o} = 125\ \mathrm{mm}$	Effective width of unstiffened compressed web
(8.22)	$\lambda_1 = 93.9\varepsilon = 68.17$	Material slenderness factor
(8.21)	$\bar{\lambda}_\mathrm{w} = \frac{3.5h_\mathrm{o}}{t_\mathrm{w}} \cdot \frac{1}{\lambda_1} = 2.139$	Relative slenderness factor of web next to opening
EN 1993-1-1: Table 6.1	$\alpha = 0.21$	Imperfection factor for buckling curves
EN 1993-1-1: 6.3.1.2(1)	$\Phi = 0.5\left[1 + \alpha\left(\bar{\lambda}_\mathrm{w} - 0.2\right) + \bar{\lambda}_\mathrm{w}^2\right] = 2.992$	
EN 1993-1-1: (6.49)	$\chi_\mathrm{wp} = \min\left(\frac{1}{\Phi + \sqrt{\Phi^2 - \bar{\lambda}_\mathrm{w}^2}};\ 1.0\right) = 0.1967$	Buckling curve reduction factor
(8.19)	$N_\mathrm{w,Rd} = \chi_\mathrm{wp} b_\mathrm{w} t_\mathrm{w} \frac{f_\mathrm{y}}{\gamma_\mathrm{M1}} = 65.8\ \mathrm{kN}$	Web buckling curve resistance
(8.17) & (8.18)	$N_\mathrm{w,Ed} = \frac{V_\mathrm{Ed}}{2} = 30.0\ \mathrm{kN}$	Compressive force acting on web next to opening
(8.15)	$\frac{N_\mathrm{w,Ed}}{N_\mathrm{w,Rd}} = 0.46 \leq 1.0 \Rightarrow$ **OK**	Web buckling verification

EN 1993-1-13: 8.3.1 Bending Resistance of a Beam with Web Openings

Tee class 2 for global bending ⇒ Plastic bending resistance

$$c_{\mathrm{t,T,mod,b}} = d_{\mathrm{t,T,mod,b}} + r = 55.55 \text{ mm}$$

Modified height of compressed Tee outstand in global bending

$$A_{\mathrm{t,T,mod,b}} = c_{\mathrm{t,T,mod,b}} t_{\mathrm{w}} + b t_{\mathrm{f}} = 1367 \text{ mm}^2$$

Modified area of compressed Tee in global bending

$$z_{\mathrm{t,T,mod,b}} = \frac{A_{\mathrm{t,T,mod,b}}}{2b} = 6.215 \text{ mm}$$

Modified NA of compressed Tee in global bending

$$c_{\mathrm{b,T,b}} = d_{\mathrm{b,T,b}} + r = 61.60 \text{ mm}$$

Height of tensed Tee in global bending

$$A_{\mathrm{b,T,b}} = c_{\mathrm{b,T,b}} t_{\mathrm{w}} + b t_{\mathrm{f}} = 1404 \text{ mm}^2$$

Area of tensed Tee in global bending

$$z_{\mathrm{b,T,b}} = \frac{A_{\mathrm{b,T,b}}}{2b} = 6.380 \text{ mm}$$

NA of tensed Tee in global bending

(8.7)

$$M_{\mathrm{o,pl,Rd}} = (h - z_{\mathrm{b,T}} - z_{\mathrm{t,T,mod,b}}) \min(A_{\mathrm{b,T}};\, A_{\mathrm{t,T,mod,b}}) \frac{f_{\mathrm{y}}}{\gamma_{\mathrm{M0}}} = 231.4 \text{ kNm}$$

Simplified plastic bending resistance at opening

(8.6)

$$\frac{M_{\mathrm{Ed}}}{M_{\mathrm{o,Rd}}} = 0.18 \leq 1.0 \Rightarrow \textbf{OK}$$

Bending resistance at opening verification

8.3.2(1)

$$a_{\mathrm{eff}} = 400 < 6 h_{\mathrm{t,T,mod,b}}\, \varepsilon \left(\frac{M_{\mathrm{o,Rd}}}{M_{\mathrm{Ed}}} \right)^{0.5} = 567.9 \text{ mm}$$

Long opening Tee buckling omittance check

$\Longrightarrow$ Do not have to check for buckling of compressed Tee according to EN 1993-1-13: 8.3.2

EN 1993-1-13: 8.4 Resistance of the Tees in Vierendeel Bending

Tee class 2 for Vierendeel bending ⇒ Plastic bending resistance, with modified Tee depth

$$c_{\mathrm{T,mod,V}} = d_{\mathrm{T,mod,V}} + r = 58.46 \text{ mm}$$

Modified height of one Tee outstand in Vierendeel bending

$$A_{\mathrm{T,mod,V}} = b t_{\mathrm{f}} + t_{\mathrm{w}} c_{\mathrm{T,mod,V}} = 1385 \text{ mm}^2$$

Modified area of one Tee in Vierendeel bending

$$z_{\mathrm{T,el,mod,V}} = \frac{b \cdot 0.5 t_{\mathrm{f}}^2 + c_{\mathrm{T,mod,V}} t_{\mathrm{w}} (t_{\mathrm{f}} + 0.5 \cdot c_{\mathrm{T,mod,V}})}{A_{\mathrm{T,mod,V}}} = 13.30 \text{ mm}$$

Modified elastic NA of Tee in Vierendeel bending from flange edge

$$z_{\mathrm{T,pl,mod,V}} = \frac{t_{\mathrm{w}} (d_{\mathrm{T,mod,V}} + r) + t_{\mathrm{f}} b}{A_{\mathrm{T,mod,V}}} = 6.29 \text{ mm} < t_{\mathrm{f}}$$

Modified plastic NA of Tee in Vierendeel bending from flange edge

$\Longrightarrow$ Plastic neutral axis in flange

$$z_{\mathrm{outstand}} = \left[t_{\mathrm{w}}(d_{\mathrm{T,mod,V}} + r) \cdot \Big(\frac{d_{\mathrm{T,mod,V}} + r}{2} + (t_{\mathrm{f}} - z_{\mathrm{T,pl,mod,V}}) \Big) + b \Big(t_{\mathrm{f}} - \frac{(d_{\mathrm{T,mod,V}})^2}{2} \Big) \right] \Big/ (0.5 A_{\mathrm{T,mod,V}}) = 17.15\,\mathrm{mm}$$

Plastic moment lever arm for Tee outstand plus part of flange

$$W_{\mathrm{T,pl,mod,V}} = \frac{A_{\mathrm{T,mod,V}}}{2} \cdot \Big(\frac{z_{\mathrm{T,pl,mod,V}}}{2} + z_{\mathrm{outstand}} \Big) = 14.05 \cdot 10^3\ \mathrm{mm}^3$$

Modified plastic section modulus of Tee

8.4(6)

$$M_{\mathrm{T,pl,Rd}} = \frac{W_{\mathrm{T,pl,mod,V}} \cdot f_{\mathrm{y}}}{\gamma_{\mathrm{M0}}} = 6.268\ \mathrm{kNm}$$

$$N_{\mathrm{T,el,Rd}} = A_{\mathrm{T,mod,V}} \frac{f_{\mathrm{y}}}{\gamma_{\mathrm{M0}}} = 617.6\ \mathrm{kN}$$

$$N_{\mathrm{m,Ed}} = N_{\mathrm{Ed}} + \frac{M_{\mathrm{o,Ed}}}{h - 2 \cdot z_{\mathrm{T,el,mod,V}}} = 114.9\ \mathrm{kN}$$

Design axial force acting on one Tee

(8.12)

$$M_{\mathrm{NV,T,Rd}} = M_{\mathrm{T,pl,Rd}} \left(1 - \left(\frac{N_{\mathrm{m,ed}}}{N_{\mathrm{T,pl,Rd}}} \right)^2 \right) = 605.1\ \mathrm{kNm}$$

Plastic bending resistance of the Tees, reduced for axial loads

Table 8.3

$$a_{\mathrm{eq}} = a_{\mathrm{o}} = 400\ \mathrm{mm}$$

Equivalent rectangular opening length

(8.11)

$$V_{\mathrm{Vier,Rd}} = \frac{4 M_{\mathrm{NV,T,Rd}}}{a_{\mathrm{eq}}} = 60.51\ \mathrm{kN}$$

Shear resistance to Vierendeel bending

(8.10)

$$\frac{V_{\mathrm{Ed}}}{V_{\mathrm{Vier,Rd}}} = 0.99 \leq 1.0 \Rightarrow \textbf{OK}$$

Vierendeel resistance verification at opening

E Design Capacity of Specimen G According to the Eurocode

Geometry:

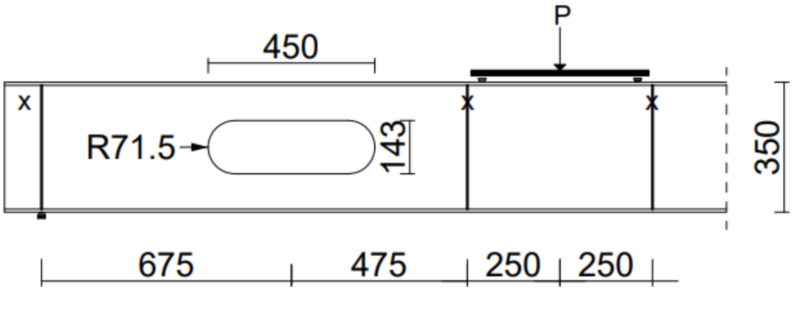

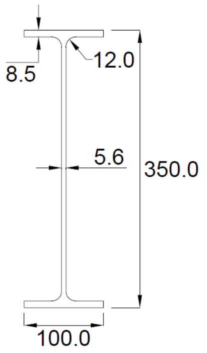

Additional Dimensions:

L	$:= 2300$ mm	Beam span
x_{o}	$:= 675$ mm	Distance from support to center of opening
s_{e}	$:= 450$ mm	Distance to support from closest opening edge
s_{i}	$:= 250$ mm	Distance to load from closest opening edge
A	$:= 3688\,\text{mm}^2$	Cross section area
d_{T}	$:= 83.0$ mm	Tee depth

Material Data:

f_{y}	$:= 446\,\text{MPa}$ (Assumed consistent for entire cross section)	Yield strength
E	$:= 210$ GPa	Young's modulus
ν	$:= 0.3$	Poisson ratio
ε	$:= \sqrt{\dfrac{235}{f_{\text{y}}}} = 0.726$	Material slenderness factor
η	$:= 1.2$	
γ_{M0}	$= \gamma_{\text{M1}} := 1$	Partial safety factors

Loads & Reaction Forces:

P_{Ed}	$:= 81.7$ kN	Ultimate external design load
N_{Ed}	$:= 0$	Design axial load
V_{Ed}	$:= 40.8$ kN	Design shear force
M_{Ed}	$:= 47.0$ kNm	Design moment at load points
$M_{\text{o,Ed}}$	$:= V_{\text{Ed}} \cdot x_{\text{o}} = 27.6$ kNm	Design moment at center of opening

EN 1993-1-1: Table 5.2 Cross Section Classification

Web: $72 < \frac{c}{t} \cdot \frac{1}{\varepsilon} = 76.0 \leq 83 \Rightarrow$ **Class 2**

Flanges: $\frac{c}{t} \cdot \frac{1}{\varepsilon} = 7.65 \leq 9 \quad \Rightarrow$ **Class 1**

Tee outstand: $\frac{c}{t} \cdot \frac{1}{\varepsilon} = 20.4 > 14 \Rightarrow$ **Class 4**

EN 1993-1-13: 7.4 Tee Cross Section Classification for Global Bending

7.4(3) Flange class 1 & Tee class 4

$\Longrightarrow$ **Tee class 3** for global bending

$\Longrightarrow$ $d_{\mathrm{T,mod,b}} = \min(14 t_{\mathrm{w}} \varepsilon;\ d_T) = 56.91$ mm — Modified Tee depth for global bending

EN 1993-1-13: 7.5 Tee Cross Section Classification for Vierendeel Bending

7.5(4) $a_{\mathrm{eff}} = a_{\mathrm{o}} - 0.3 h_{\mathrm{o}} = 407.1$ mm — Effective opening length

7.5(5) $a_{\mathrm{eff}} > 36 t_{\mathrm{w}} \varepsilon = 146.3\,\mathrm{mm}$ — Class 3 limit for a_{eff}

$$d_{\mathrm{T,limit,2}} = 10 t_{\mathrm{w}} \varepsilon \Bigg/ \sqrt{1 - \left(\frac{32 t_{\mathrm{w}} \varepsilon}{a_{\mathrm{eff}}}\right)^2} = 42.90 \text{ mm}$$

Class 2 limit of d_{T}

$d_{\mathrm{T}} = 83.00\,\mathrm{mm} > d_{\mathrm{T,limit,2}} = 42.90\,\mathrm{mm}$

$\Longrightarrow$ Cannot use Tee class 2

7.5(8)

$$d_{\mathrm{T,limit,3}} = 14 t_{\mathrm{w}} \varepsilon \Bigg/ \sqrt{1 - \left(\frac{36 t_{\mathrm{w}} \varepsilon}{a_{\mathrm{eff}}}\right)^2} = 60.99 \text{ mm}$$

Class 3 limit of d_{T}

$d_{\mathrm{T}} = 83.00\,\mathrm{mm} > d_{\mathrm{T,limit}} = 60.99\,\mathrm{mm}$

7.5(10) 7.5(8) not fulfilled for Tee class 4

$\Longrightarrow$ May reduce Tee class to 3 and use reduced d_{T}

$\Longrightarrow$ **Tee class 3** for Vierendeel bending

$\Longrightarrow$ $d_{\mathrm{T,mod,V}} = \min\left(d_{\mathrm{T,limit,3}};\ d_{\mathrm{T}}\right) = \underline{60.99\,\mathrm{mm}}$ — Modified Tee depth for Vierendeel bending

EN 1993-1-1: 6.2.6 ULS Shear

6.2.6(3) $A_{\mathrm{V}} = \max(A - 2 b t_{\mathrm{f}} + (t_{\mathrm{w}} - 2r) t_{\mathrm{f}};\ \eta h_{\mathrm{w}} t_{\mathrm{w}})$ — Shear area

$= 2116 \text{ mm}^2$

(6.18) $V_{\mathrm{pl,Rd}} = \frac{A_{\mathrm{V}}(f_{\mathrm{y}}/\sqrt{3})}{\gamma_{\mathrm{M0}}} = 576.2$ kN — Plastic shear capacity

(6.17)	$\frac{V_{\text{Ed}}}{V_{\text{pl,Rd}}}$	$= 0.07 \leq 1.0 \Rightarrow$ **OK**	Shear capacity verification
6.2.10(3)	$\frac{V_{\text{Ed}}}{V_{\text{pl,Rd}}}$	$= 0.07 \leq 0.5 \Rightarrow$ **OK**	Shear force yield strength reduction check
(6.22)	$\frac{h_w}{t_w} \cdot \frac{\eta}{\varepsilon}$	$= 98.30 > 72 \Rightarrow$ **NOT OK**	Web shear buckling control

$\Longrightarrow$ Have to check for shear buckling according to EN 1993-1-5: 5 Resistance to shear

EN 1993-1-5: 5 Resistance to Shear

A.3(1)	a	$= L/2 = 1150\,\text{mm} \geq h_{\text{w}} = 350$ mm	Distance between transverse stiffeners
	$k_{\tau sl}$	$= 0$ (No longitudinal stiffeners)	Longitudinal stiffener shear buckling coefficient
(A.5)	k_{τ}	$= 5.34 + 4.00 \left(\frac{h_{\text{w}}}{a}\right)^2 + k_{\tau,sl} = 5.68$	Web slenderness parameter
(5.6)	$\overline{\lambda}_{\text{w}}$	$= \frac{h_{\text{w}}}{37.4 t \varepsilon \sqrt{k_{\tau}}} = 0.9194$	Shear buckling coefficient
Table 5.1	$\frac{0.83}{\eta}$	$\leq \overline{\lambda}_{\text{w}} = 0.9194 < 1.08$	
	χ_{w}	$= \frac{0.83}{\overline{\lambda}_w} = 0.9027$	Web buckling factor
(5.2)	$V_{\text{bw,Rd}}$	$= \frac{\chi_{\text{w}} f_{\text{y}} h_{\text{w}} t}{\sqrt{3} \gamma_{\text{M1}}} = 433.5$ kN	Web contribution to shear resistance
5.4(1)	b_{f}	$= \min(b; t_{\text{w}} + 2 \cdot 15 \varepsilon t_{\text{f}}) = 100$ mm	Flange width contribution limit
	c	$= a \left(0.25 + 1.6 \frac{b_{\text{f}}\, t_{\text{f}}^2}{t_{\text{w}}\, h_{\text{w}}^2}\right) = 308.9$ mm	Transverse stiffener contribution coefficient
	$M_{\text{f,pl,Rd}}$	$= \frac{M_{\text{f,k}}}{\gamma_{\text{M0}}} = 129.5$ kNm	Axial force reduction factor
(5.9)	N_{Ed}	$= 0 \Rightarrow 1$ (No reduction)	Axial force reduction factor
(5.8)	$V_{\text{bf,Rd}}$	$= \frac{b_{\text{f}} t_{\text{f}}^2 f_{\text{y}}}{c \gamma_{\text{M1}}} \left(1 - \left(\frac{M_{\text{Ed}}}{M_{\text{f,Rd}}}\right)\right)^2 = 9.06$ kN	Flanges contribution to shear resistance
(5.1)	$V_{\text{b,Rd}}$	$= \min\left(V_{\text{bw,Rd}} + V_{\text{bf,Rd}}; \frac{\eta f_{\text{y}} h_{\text{w}} t}{\sqrt{3} \gamma_{\text{M1}}}\right) = 442.5$ kN	Cross section shear resistance
(5.10)	η_3	$= \frac{V_{\text{Ed}}}{V_{\text{b,Rd}}} = 0.09 \leq 1.0 \Rightarrow$ **OK**	Shear force verification

EN 1993-1-1: 6.2.4 ULS Compression

(6.10)	$N_{\text{c,Rd}}$	$= \dfrac{Af_{\text{y}}}{\gamma_{M0}} = 1921 \text{ kN}$	Cross section centric compression capacity
(6.9)	$\dfrac{N_{\text{Ed}}}{N_{\text{c,Rd}}}$	$= 0 \leq 1.0 \Rightarrow$ **OK**	Axial force verification

EN 1993-1-1: 6.2.5 ULS Bending Moment

	$W_{\text{y,pl}}$	$= 2\left(bt_{\text{f}}\dfrac{h-t_{\text{f}}}{2} + \dfrac{t_{\text{w}}\,h_{\text{w}}^2}{8}\right) = 445.5 \cdot 10^3 \text{ mm}^3$	Cross section major axis plastic modulus
(6.13)	$M_{\text{c,Rd}}$	$= M_{\text{pl,Rd}} = \dfrac{W_{\text{y,pl}}f_{\text{y}}}{\gamma_{\text{M0}}} = 198.7 \text{ kNm}$	Cross section major axis bending moment capacity
(6.12)	$\dfrac{M_{\text{Ed}}}{M_{\text{c,Rd}}}$	$= 0.24 \leq 1.0 \Rightarrow$ **OK**	Bending moment at midspan verification

EN 1993-1-1: 6.2.1 ULS General

(6.2)	$\dfrac{N_{\text{Ed}}}{N_{\text{Rd}}} + \dfrac{M_{\text{y,Ed}}}{M_{\text{y,Rd}}} = 0 + 0.24 = 0.24 \leq 1.0 \Rightarrow$ **OK**	Conservative linear combination of reaction forces

EN 1993-1-13: Limiting Dimensions for Unstiffened Openings

Table 8.1	h_{o}	$= 143\,\text{mm} \leq 0.8h = 280\,\text{mm} \Rightarrow$ **OK**	Maximum opening height
	a_{o}	$= 450\,\text{mm} \leq 3h_o = 429\,\text{mm} \Rightarrow$ **NOT OK**	Maximum opening length
	s_{e}	= Not available	Minimum edge to edge spacing
	$d_{\text{t,T}}$	$= 83.0\,\text{mm} \geq \max\left(\dfrac{a_{\text{o}}}{12};\ 0.1h\right) = 37.5\,\text{mm} \Rightarrow$ **OK**	Minimum depth of Tee in compression
	$d_{\text{b,T}}$	$= 83.0\,\text{mm} \geq 0.1h = 35.0\,\text{mm} \Rightarrow$ **OK**	Minimum depth of Tee in tension

EN 1993-1-13: 8.2 Shear Resistance at Web Opening Positions

(8.3)	$V_{\text{o,pl,Rd}}$	$= \min\left(V_{\text{pl,Rd}} - \dfrac{h_{\text{o}}t_{\text{w}}f_{\text{y}}}{\sqrt{3}\gamma_{\text{M0}}};\ V_{\text{w,b,Rd}}\right) = 370.0\,\text{kN}$	Shear resistance at web opening
(8.1)	$\dfrac{V_{\text{Ed}}}{V_{\text{o,pl,Rd}}}$	$= 0.11 \leq 1.0 \Rightarrow$ **OK**	Opening shear force verification
8.2(2)	$\dfrac{V_{\text{Ed}}}{V_{\text{o,pl,Rd}}}$	$= 0.11 \leq 0.5 \Rightarrow$ **OK**	Opening shear force yield strength reduction check

8.5.1(3)	$\frac{h_\mathrm{w}}{t_\mathrm{w}} \cdot \frac{\eta}{\varepsilon} = 98.30 > 72 \Rightarrow$ **NOT OK**	Web shear buckling control
8.5.1(4)	$h_\mathrm{o} = 143\,\mathrm{mm} > 25 t_\mathrm{w} \varepsilon = 101.6\,\mathrm{mm} \Rightarrow$ **NOT OK**	Web shear buckling omittance check
$\Longrightarrow$	Have to check for shear buckling of web next to opening according to EN 1993-1-13: 8.5.2	
8.8.1(4)	$s_\mathrm{e} = 450\,\mathrm{mm} > a_\mathrm{eff} = 407.1\,\mathrm{mm} \Rightarrow$ **OK**	End-post shear buckling omittance check
$\Longrightarrow$	Do not have to check for shear buckling of end-post web according to EN 1993-1-13: 8.8.1	
8.8.2(2)	$s_\mathrm{i} = 250\,\mathrm{mm} > \min(0.5 a_\mathrm{eff};\ h_\mathrm{o}) = 143\,\mathrm{mm} \Rightarrow$ **OK**	Load close to opening check
$\Longrightarrow$	Do not have to check for loads over or close to openings according to EN 1993-1-13: 8.8.2	

EN 1993-1-13: 8.5.2 Web Buckling

8.5.2(3)	$b_\mathrm{w} = 0.5 h_\mathrm{o} = 71.50\ \mathrm{mm}$	Effective width of unstiffened compressed web
(8.22)	$\lambda_1 = 93.9\varepsilon = 68.17$	Material slenderness factor
(8.21)	$\overline{\lambda}_\mathrm{w} = \frac{2.4 h_\mathrm{o}}{t_\mathrm{w}} \cdot \frac{1}{\lambda_1} = 0.8990$	Relative slenderness factor of web next to opening
EN 1993-1-1: Table 6.1	$\alpha = 0.21$	Imperfection factor for buckling curves
EN 1993-1-1: 6.3.1.2(1)	$\Phi = 0.5 \left[1 + \alpha \left(\overline{\lambda}_\mathrm{w} - 0.2\right) + \overline{\lambda}_\mathrm{w}^2\right] = 0.9975$	
EN 1993-1-1: (6.49)	$\chi_\mathrm{wp} = \min \left(\frac{1}{\Phi + \sqrt{\Phi^2 - \overline{\lambda}_\mathrm{w}^2}};\ 1.0 \right) = 0.7346$	Buckling curve reduction factor
(8.19)	$N_\mathrm{w,Rd} = \chi_\mathrm{wp} b_\mathrm{w} t_\mathrm{w} \frac{f_\mathrm{y}}{\gamma_\mathrm{M1}} = 131.2\ \mathrm{kN}$	Web buckling curve resistance
(8.17) & (8.18)	$N_\mathrm{w,Ed} = \frac{V_\mathrm{Ed}}{2} = 20.42\ \mathrm{kN}$	Compressive force acting on web next to opening
(8.15)	$\frac{N_\mathrm{w,Ed}}{N_\mathrm{w,Rd}} = 0.16 \leq 1.0 \Rightarrow$ **OK**	Web buckling verification

EN 1993-1-13: 8.3.1 Bending Resistance of a Beam with Web Openings

Tee class 3 for global bending ⇒ Elastic bending resistance

	$c_{\mathrm{t,T,mod,b}} = d_{\mathrm{t,T,mod,b}} + r = 68.91\ \mathrm{mm}$	Modified height of compressed Tee outstand in global bending
	$A_{\mathrm{t,T,mod,b}} = c_{\mathrm{t,T,mod,b}} t_{\mathrm{w}} + b t_{\mathrm{f}} = 1236\ \mathrm{mm}^2$	Modified area of compressed Tee in global bending
	$z_{\mathrm{t,T,mod,b}} = \dfrac{b \cdot 0.5 t_{\mathrm{f}}^2 + c_{\mathrm{t,T,mod,b}} t_{\mathrm{w}} (t_{\mathrm{f}} + 0.5 \cdot c_{\mathrm{t,T,mod,b}})}{A_{\mathrm{t,T,mod,b}}} = 16.34\ \mathrm{mm}$	Modified NA of compressed Tee in global bending (from top of beam)
	$c_{\mathrm{b,T,b}} = d_{\mathrm{b,T,b}} + r = 95.00\ \mathrm{mm}$	Height of tensed Tee in global bending
	$A_{\mathrm{b,T,b}} = c_{\mathrm{b,T,b}} t_{\mathrm{w}} + b t_{\mathrm{f}} = 1382\ \mathrm{mm}^2$	Area of tensed Tee in global bending (from the bottom)
	$z_{\mathrm{b,T,b}} = \dfrac{b \cdot 0.5 t_{\mathrm{f}}^2 + c_{\mathrm{b,T,b}} t_{\mathrm{w}} (t_{\mathrm{f}} + 0.5 \cdot c_{\mathrm{b,T,b}})}{A_{\mathrm{b,T,b}}} = 24.17\ \mathrm{mm}$	NA of tensed Tee in global bending
	$z_{\mathrm{T,el,mod}} = \dfrac{A_{\mathrm{t,T,mod,b}} z_{\mathrm{t,T,mod,b}} + A_{\mathrm{b,T}} z_{\mathrm{b,T}}}{A_{\mathrm{t,T,mod,b}} + A_{\mathrm{b,T}}} = 179.7\ \mathrm{mm}$	Effective NA of the Tees
	$I_{\mathrm{t,T,el,mod}} = \dfrac{b \cdot t_{\mathrm{f}}^3 + c_{\mathrm{t,T,mod,b}} \cdot t_{\mathrm{w}}^3}{12} + (b \cdot t_{\mathrm{f}})(z_{\mathrm{t,T,mod,b}} - 0.5 t_{\mathrm{f}})^2 + (c_{\mathrm{t,T,mod,b}} \cdot t_{\mathrm{w}})(0.5 c_{\mathrm{t,T,mod,b}} - z_{\mathrm{t,T,mod,b}} + t_{\mathrm{f}})^2 = 5.55 \cdot 10^5\ \mathrm{mm}^4$	Modified second moment of area, top Tee
	$I_{\mathrm{b,T,el}} = \dfrac{b \cdot t_{\mathrm{f}}^3 + c_{\mathrm{b,T,b}} \cdot t_{\mathrm{w}}^3}{12} + (b \cdot t_{\mathrm{f}})(z_{\mathrm{b,T,b}} - 0.5 t_{\mathrm{f}})^2 + (c_{\mathrm{b,T,b}} \cdot t_{\mathrm{w}})(0.5 c_{\mathrm{b,T,b}} - z_{\mathrm{b,T,b}} + t_{\mathrm{f}})^2 = 12.8 \cdot 10^5\ \mathrm{mm}^4$	Modified second moment of area, bottom Tee
	$W_{\mathrm{el,o}} = \Big(I_{\mathrm{t,T,el,mod}} + I_{\mathrm{b,T,el}} + A_{\mathrm{t,T,mod,b}}(z_{\mathrm{T,el,mod}} - z_{\mathrm{t,T,mod,b}})^2 + A_{\mathrm{b,T,b}}(h - z_{\mathrm{b,T,b}} - z_{\mathrm{t,T,mod,b}})^2\Big) \Big/ z_{\mathrm{T,el,mod}} = 3.58 \cdot 10^3\ \mathrm{mm}^3$	Elastic section modulus at opening
(8.7)	$M_{\mathrm{o,el,Rd}} = \dfrac{W_{\mathrm{el,o}} f_{\mathrm{y}}}{\gamma_{\mathrm{M0}}} = 160\ \mathrm{kNm}$	Elastic bending resistance at opening
(8.6)	$\dfrac{M_{\mathrm{Ed}}}{M_{\mathrm{o,Rd}}} = 0.17 \leq 1.0 \Rightarrow$ **OK**	Bending resistance at opening verification

8.3.2(1)	a_{eff}	$= 407 < 6 h_{\mathrm{t,T,mod,b}}\, \varepsilon \left(\frac{M_{\mathrm{o,Rd}}}{M_{\mathrm{Ed}}} \right)^{0.5} = 811\ \mathrm{mm}$	Long opening Tee buckling omittance check

$\Longrightarrow$ Do not have to check for buckling of compressed Tee according to EN 1993-1-13: 8.3.2

EN 1993-1-13: 8.4 Resistance of the Tees in Vierendeel Bending

Tee class 3 for Vierendeel bending ⇒ Elastic bending resistance, with modified Tee depth

	$c_{\mathrm{T,mod,V}}$	$= d_{\mathrm{T,mod,V}} + r = 60.99\ \mathrm{mm}$	Modified height of one Tee outstand in Vierendeel bending
	$A_{\mathrm{T,mod,V}}$	$= b t_{\mathrm{f}} + t_{\mathrm{w}} c_{\mathrm{T,mod,V}} = 1385\ \mathrm{mm}^2$	Modified area of one Tee in Vierendeel bending
	$z_{\mathrm{T,el,mod,V}}$	$= \frac{b \cdot 0.5 t_{\mathrm{f}}^2 + c_{\mathrm{T,mod,V}} t_{\mathrm{w}} (t_{\mathrm{f}} + 0.5 \cdot c_{\mathrm{T,mod,V}})}{A_{\mathrm{T,mod,V}}}$ $= 17.48\ \mathrm{mm}$	Modified elastic NA of Tee in Vierendeel bending from flange edge
	$I_{\mathrm{T,el,mod}}$	$= \frac{b \cdot t_{\mathrm{f}}^3 + c_{\mathrm{T,mod,V}} \cdot t_{\mathrm{w}}^3}{12}$ $+ (b \cdot t_{\mathrm{f}})(z_{\mathrm{T,el,mod,V}} - 0.5 t_{\mathrm{f}})^2$ $+ (c_{\mathrm{T,mod,V}} \cdot t_{\mathrm{w}})(0.5 c_{\mathrm{T,mod,V}} - z_{\mathrm{T,el,mod,V}} + t_{\mathrm{f}})^2$ $= 6.45 \cdot 10^5\ \mathrm{mm}^4$	Modified second moment of area, top Tee
8.4(6)	$M_{\mathrm{T,el,Rd}}$	$= \frac{I_{\mathrm{T,el,mod}} \cdot f_{\mathrm{y}}}{(c_{\mathrm{T,mod,V}} + r + t_{\mathrm{f}} - z_{\mathrm{T,el,mod,V}}) \gamma_{\mathrm{M0}}}$ $= 4.492\ \mathrm{kNm}$	Elastic bending resistance of one Tee
	$N_{\mathrm{T,el,Rd}}$	$= A_{\mathrm{T,mod,V}} \frac{f_{\mathrm{y}}}{\gamma_{\mathrm{M0}}} = 561.4\ \mathrm{kN}$	Plastic compression resistance of one Tee
	$N_{\mathrm{m,Ed}}$	$= N_{\mathrm{Ed}} + \frac{M_{\mathrm{o,Ed}}}{h - 2 \cdot z_{\mathrm{T,el,mod,V}}} = 87.51\ \mathrm{kN}$	Design axial force acting on one Tee
(8.12)	$M_{\mathrm{NV,T,Rd}}$	$= M_{\mathrm{T,el,Rd}} \left(1 - \frac{N_{\mathrm{m,ed}}}{N_{\mathrm{T,el,Rd}}} \right) = 3.79\ \mathrm{kNm}$	Elastic bending resistance of the Tees, reduced for axial loads
Table 8.3	a_{eq}	$= a_{\mathrm{o}} - 0.55 h_{\mathrm{o}} = 371.4\ \mathrm{mm}$	Equivalent rectangular opening length
(8.11)	$V_{\mathrm{Vier,Rd}}$	$= \frac{4 M_{\mathrm{NV,T,Rd}}}{a_{\mathrm{eq}}} = 40.85\ \mathrm{kN}$	Shear resistance to Vierendeel bending
(8.10)	$\frac{V_{\mathrm{Ed}}}{V_{\mathrm{Vier,Rd}}}$	$= 1.00 \leq 1.0 \Rightarrow$ **OK**	Vierendeel resistance verification at opening

NTNU

Norwegian University of
Science and Technology